

**POLYMERIC-BIMETALLIC OXIDE
NANOALLOY FOR THE CONSTRUCTION
OF PHOTOVOLTAIC CELLS**



**UNIVERSITY of the
WESTERN CAPE**

By

GCINEKA MBAMBISA

**A thesis submitted in fulfilment of the
requirement for the degree of**

Philosophiae Doctor

in the

DEPARTMENT OF CHEMISTRY

FACULTY OF SCIENCE

UNIVERSITY OF THE WESTERN CAPE

Supervisors: Prof. Emmanuel I. Iwuoha

Co-supervisor: Prof. Christopher J. Arendse

TABLE OF CONTENTS

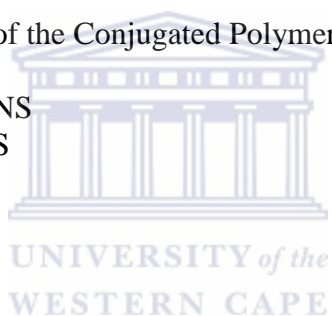
TITLE	i
TABLE OF CONTENTS	ii
ACKNOWLEDGEMENTS	vii
ABSTRACT	viii
LIST OF FIGURES	x
LIST OF TABLES	xiv
LIST OF ABBREVIATIONS	xv
CHAPTER 1 :INTRODUCTION	1
1. 1 SYNOPSIS	1
1.2 AIMS AND OBJECTIVES OF RESEARCH	2
CHAPTER 2 : BACKGROUND	4
2.1 HISTORY OF PHOTOVOLTAICS	5
2.2 TYPES OF PHOTOVOLTAIC CELLS	6
2.2.1 Inorganic Solar Cells	6
2.2.1.1 Silicon Solar Cells	7
2.2.1.2 Nanomaterials	8
2.2.2. Organic Solar Cells	8
2.2.3.1 Operating Principle of an Organic Solar Cells	9
2.2.3.2 Materials used	10
2.2.3.2.1 Conducting Polymers	11
2.2.3.2.2 Synthesis of the Conductive Polymers	13
2.2.3.2.3 Polyaniline	14
2.2.3.2.4 Poly(<i>ortho</i> -methoxyaniline) (POMA)	16
2.2.3.2.5 Doping	16
2.2.3.2.5 Charge Carriers in Conjugated Polymers	18
2.2.3.2.6 Importance of Photoluminescence in Photovoltaic cells	21
2.2.3.5 Acceptors in Organic Solar Cells	24
2.3 DEVICE ARCHITECTURE	25
2.3.1. Single-layer Cells	26
2.3.2 Bilayer Heterojunction	26
2.3.3 Bulk Heterojunction	27
2.3.4 Hybrid Heterojunction	27
2.4 CHARACTERISATION TECHNIQUES FOR PHOTOVOLTAIC CELL MATERIALS	28
2.4.1 Morphology	28

2.4.1.1 Scanning Electron Microscopy (SEM)	28
2.4.1.2 Transmission Electron Microscopy (TEM)	29
2.4.2 Thermal Gravimetric Analysis	30
2.4.3 Electrochemistry	30
2.4.3.1 Voltammetry	30
2.4.3.2 Electrochemical Impedance Spectroscopy (EIS)	32
CHAPTER 3 :EXPERIMENTAL	38
3.1 MATERIALS	39
3.2 ANALYTICAL TECHNIQUES	39
3.3 SYNTHESIS	41
3.3.1 Synthesis of Anthracene sulfonic acid and Phenanthrene sulfonic acid	41
3.3.2 Synthesis of polyaniline	41
3.3.3 Synthesis of Polyaniline/Phenanthrene sulfonic acid	41
3.3.4 Synthesis of poly(ortho-methoxyaniline)/Anthracene sulfonic acid nanostructures and poly(ortho-methoxyaniline)/Phenanthrene sulfonic acid	42
3.3.6 Synthesis of the Gallium Perchlorate	43
3.3.7 Synthesis of the ZnGa ₂ O ₄ nanoparticles	43
3.4 MEASUREMENT OF PHOTOPHYSICAL PROPERTIES	43
3.4.1 Fluorescence quantum yields	43
3.5 ELECTROCHEMICAL CHARACTERISATION	44
3.5.1 Preparation of the surface modified electrode	44
3.5.2 Electrochemical Impedance measurements	44
3.6 TECHNIQUES USED IN CONSTRUCTION OF THE PHOTOVOLTAIC CELL	44
3.6.1 Spin Coating	44
3.6.2 Sputter coating	45
3.7 CONSTRUCTION OF THE PHOTOVOLTAIC CELL	46

CHAPTER 4 : CHARACTERISATION OF THE MATERIALS	51
4.1 VIBRATIONAL SPECTROSCOPY OF THE POLYMERS	52
4.1.1. FTIR of the Conjugated Polymers	52
4.1.2 Raman Spectra of the Conjugated Polymers	54
4.2 PHOTOSPECTROSCOPIC CHARACTERISATION OF THE COMPOUNDS IN SOLUTION	56
4.2.1 Electronic Transitions in Conjugated Polymers	56
4.2.2 Electronic transitions in ZnGa ₂ O ₄ nanoparticles	61
4.2.3 Photoluminescence of the Conjugated Polymers	62
4.2.4 Photoluminescence of the ZnGa ₂ O ₃ nanoparticles	65
4.2.5 Photoluminescence behaviour of the Conjugated Polymers with the nanoparticles in solution	66
4.3 MORPHOLOGICAL ANALYSIS FROM SEM	69
4.3.1 Conjugated Polymers	69
4.4 X-RAY DIFFRACTION PATTERN OF THE CONJUGATED POLYMERS	71
4.5 X-RAY DIFFRACTION PATTERN OF THE ZnGa ₂ O ₄	72
4.6 MORPHOLOGICAL ANALYSIS FROM TEM	73
4.6.1 Conjugated Polymers	73
4.5.2 ZnGa ₂ O ₄ nanoparticles	76
4.7 THERMAL GRAVIMETRIC ANALYSIS OF THE CONJUGATED POLYMERS	77
CHAPTER 5 : ELECTROCHEMICAL CHARACTERISATION OF THE CONJUGATED POLYMERS	81
5.1. CYCLIC VOLTAMMETRY OF THE CONJUGATED POLYMERS	82
5.2 ELECTROCHEMICAL IMPEDANCE SPECTROSCOPY OF CONJUGATED POLYMERS	87



CHAPTER 6 : APPLICATION OF MATERIALS IN HYBRID PHOTOVOLTAIC CELLS	91
6.1 ELECTRONIC BEHAVIOUR OF THE CONJUGATED POLYMERS IN THE PRESENCE OF NANOPARTICLES AND PCBM IN SOLUTION	92
6.1.1 Electronic Interaction between the Conjugated Polymers and PCBM	92
6.1.2 Electronic Interaction between the Conjugated Polymers and Nanoparticles in the presence of PCBM	93
6.2 PHOTOLUMINESCENCE BEHAVIOUR OF THE COMPOUNDS ON ITO COATED GLASS	94
6.1.2 Conjugated Polymers with PCBM on ITO	98
6.1.3 Conjugated Polymers with nanoparticles and PCBM on ITO	99
6.1.4 Photovoltaic behaviour of the Conjugated Polymers with PCBM as acceptor	99
CHAPTER 7 : CONCLUSIONS	104
CHAPTER 8 : REFERENCES	107



DECLARATION

I declare that *Polymeric-Bimetallic Oxide Nanoalloys for the Construction of Photovoltaic cells* is my own work, that it has not been submitted for any degree or examination in any other university, and that all sources I have used or quoted have been indicated and acknowledged by complete references.

Gcineka Mbambisa

December 2014

Signed.....



ACKNOWLEDGEMENTS

First and foremost I want to thank the one who lightens whatever load, the God Almighty.

My appreciation goes to my supervisor, Prof E.I Iwuoha and Prof C.J Arendse, your assistance and guidance is appreciated.

My gratitude goes out to the friends who have been with me throughout this period, Lusanda Kuboni, Taofeek Ogunbayo, Kerileng Molapo, Ntombomzi Mbelebele, Desmond Modibane, Peter Ndangili.

I have to extend my appreciation to the following:

- My fellow labmates at SensorLab. It provided an environment that allows for growth academically and personally.
- The chemistry department technical staff.
- The electron microscopy unit at the University of the Western Cape.

Lastly I would like to extend my gratitude to my family. My appreciation goes to my *late* parents, Hudson Fezile Mbambisa and Tantaswa Esther Mbambisa, who were the ones that ignited my love of academia. A special thanks to my siblings, Nothukela Mbambisa, Thobile Mbambisa, Nokwazi Mbambisa, my pillars of strength. I am at this level because of your love, devotion, encouragement. The faith that you have in me has been my reservoir of strength. *Ndiyabulela baThembu abahle.*

ABSTRACT

Research in renewable energy has become a focal point as a solution to the energy crisis. One of renewable forms of energy is solar energy, with the main challenge in the development of the solar cells being the high cost. This has led to the exploration of the use of organic molecules to construct solar cells since it will lead to lowered costs of construction. The focus of this research is on the synthesis and characterisation of the polyaniline derivatives materials and zinc gallate for application in the construction of hybrid solar cells with [6,6]-phenyl-C₆₁-butyric acid methyl ester (PCBM) as an acceptor. The polyaniline (PANi) and doped polyaniline derivatives, polyaniline phenanthrene sulfonic acid (PANi-PSA), poly[*ortho*-methyl aniline] phenanthrene sulfonic acid (POMA-PSA) poly[*ortho*-methyl aniline] anthracene sulfonic acid (POMA-ASA) were produced via chemical synthetic procedures. The zinc gallate (ZnGa₂O₄) was also produced using a chemical method. The vibrational and electronic spectra of the polymers and zinc gallate were interrogated independently and dependently. Electronic transitions due to charge defects (polarons and bipolarons) were observed for the polymers that are doped. The PANi was the one with the lowest band gap of 2.4 eV with the POMA-ASA having the widest bandgap of 3.0 eV. The XRD and TEM analysis of the polymers revealed characteristics that show that the PANi has the highest level of crystallinity and the POMA-ASA displayed the least level of crystallinity. The electronic data, XRD, TEM data led to the conclusion that the conductivity of the polymers is decreasing in the following sequence, PANi > PANi-PSA > POMA-PSA > POMA-ASA. The photoluminescence of the polymers alone and with the nanoparticles was investigated in solution and on an ITO coated glass substrate. Photoluminescence was observed for the polymers due to relaxation of the exciton and also from the formation of excimers.

The relaxation due to the exciton was observed at higher energy levels, while the one that is as a result of the excimer formation was seen at lower energy levels. Enhancement of the peak due to the excimer was observed when the compound is mixed with the nanoparticles in solution. When the analysis was done on the ITO coated glass substrate, it was found that zinc gallate does not lead to quenching of the emission of the polymers; hence it can not be used as an acceptor in this particular system. The electrochemical behaviour of the polyaniline derivatives was investigated using cyclic voltammetry and electrochemical impedance spectroscopy. Interaction of the polymers with the PCBM (acceptor) was investigated using UV-visible absorption spectroscopy and photoluminescence spectroscopy. It was able to quench the photoluminescence of the polymers. Hence it was used as an acceptor in the construction of the photovoltaic cells. The polymers alone and with the nanoparticles were used in the formation of bulk heterojunction photovoltaic cells with PCBM as an acceptor. The photovoltaic behaviour was investigated and PANi was the one that displayed the highest efficiency.

LIST OF FIGURES

Figure 2.1: A figure depicting the formation of a module of a solar panel from a photovoltaic cell	6
Figure 2.2: A diagram showing the formation of the electron hole pair at the conduction and valence band of an inorganic material	7
Figure 2.3: (a) c-Si well ordered, stable structure and (b) a-Si unstable structure	8
Figure 2.4: Schematic representation of the operating principle of an inorganic solar cell	10
Figure 2.5: Diagrams showing typical conjugated conducting polymers	12
Figure 2.6: The intrinsic redox states of polyaniline	15
Figure 2.7: Schematic representation of the chemical polymerisation of aniline	16
Figure 2.8: Schematic representation of the soliton charge defect that can be observed in conjugated polymers	18
Figure 2.9: Schematic representation of the polaron charge defect that can be observed in conjugated polymers	19
Figure 2.10: Schematic representation of the bipolaron charge defect that can be observed in conjugated polymers	20
Figure 2.11: Jabłoński diagram representing the processes that occur upon photoexcitation	22
Figure 2.12: Schematic representation of the photoinduced electron transfer process	24
Figure 2.13: Schematic representation of the device architecture in solar cells	28
Figure 2.14: The schematic representation of a Nyquist plot	34
Figure 2.15: Bode plot for a simple electrochemical system	37
Figure 3.1: Schematic representation of the spin coating process	45
Figure 3.2: Schematic representation of the sputter coater	46

Figure 3.3: The I-V curves of an organic solar cell without light (a) and illuminated with light (b). The open circuit voltage (V_{oc}) and the short-circuit current (I_{sc}) are shown.	48
Figure 4.1: ATR-FTIR spectrum of a) PANi b) PANi-PSA, c) POMA-ASA, d) POMA-PSA	53
Figure 4.2: The Raman spectra of PANi and PANi-PSA using a 532 nm laser beam	55
Figure 4.3: The Raman spectra of POMA-ASA and POMA-PSA using a 532 nm laser beam	55
Figure 4.4: The electronic transition spectrum of POMA-ASA	57
Figure 4.5: The electronic transition spectrum of POMA-PSA	58
Figure 4.6: The electronic transition spectrum of PANi	59
Figure 4.7: The electronic transition spectrum of PANi-PSA	60
Figure 4.8: The electronic transition spectrum of $ZnGa_2O_4$ nanoparticles	62
Figure 4.9: The fluorescence spectra of the conjugated polymers	63
Figure 4.10: The excitation and emission spectra of $ZnGa_2O_4$ nanoparticles	66
Figure 4.11: The emission of the (a) PANi alone and PANi with nanoparticles ($ZnGa_2O_4$) (b) PANi-PSA alone and PANi-PSA with nanoparticles ($ZnGa_2O_4$) (c) POMA-ASA alone and POMA-ASA with nanoparticles ($ZnGa_2O_4$) (d) POMA-PSA alone and POMA-PSA with nanoparticles ($ZnGa_2O_4$) in DMSO at an excitation wavelength of 320 nm	69
Figure 4.12: SEM images of (a) POMA-ASA and (b) POMA-PSA	70
Figure 4.13: SEM images of (a) PANi and (b) PANi-PSA	70
Figure 4.14: X-ray Diffraction pattern of the conjugated polymers	72
Figure 4.15: X-ray diffraction pattern of the $ZnGa_2O_4$ nanoparticles	73

Figure 4.16: TEM images of (a) PANi (b) PANi-PSA, (c) POMA-ASA and (d) POMA-PSA	75
Figure 4.17: TEM images of ZnGa ₂ O ₄ at a (a) 100 000 X magnification and (b) at 500 000X magnification	76
Figure 4.18: Thermal gravimetric curve of (a) PANi, b) PANi-PSA, c) POMA-ASA, d) POMA-PSA	79
Figure 4.19: Possible degradation products from thermal gravimetric analysis of the conjugated polymers	80
Figure 5.1: Scan rate dependence of the cyclic voltammetry of PANi paste in 1 M HCl	82
Figure 5.2: Scan rate dependence of the cyclic voltammetry of the PANi-PSA paste in 1 M HCl	83
Figure 5.3: Scan rate dependence of the cyclic voltammetry of the POMA-PSA paste in 1 M HCl	84
Figure 5.4: Scan rate dependence of the cyclic voltammetry of the PANi-PSA paste in 1 M HCl	85
Figure 5.5: The Bode plots of a) PANi, b) PANi-PSA, c) POMA-PSA and d) POMA-ASA analysed using 1 M HCl	90
Figure 6.1: The electronic spectrum of the conjugated polymers in the presence of the PCBM (acceptor) in DMSO	93
Figure 6.2: The electronic spectrum of the conjugated polymers in the presence of nanoparticles and PCBM (acceptor)	94
Figure 6.3: The photoluminescence behaviour of (a) PANi) PANi alone and PANi with nanoparticles (ZnGa ₂ O ₄) (b) PANi-PSA alone and PANi-PSA with nanoparticles (ZnGa ₂ O ₄) (c) POMA-ASA alone and POMA-ASA with nanoparticles	

(ZnGa ₂ O ₄) (d) POMA-PSA alone and POMA-PSA with nanoparticles (ZnGa ₂ O ₄) on ITO	97
Figure 6.4: The photoluminescence behaviour of the polymers in the presence of PCBM	98
Figure 6.5: The photoluminescence response of the polymers in the presence of nanoparticles and PCBM	99
Figure 6.6: The I-V Curves of the photovoltaic cells under illumination	101
Figure 6.7: The I-V Curves of the photovoltaic cells under illumination	103



LIST OF TABLES

Table 1: The band gaps of materials commonly used as electron acceptors	25
Table 2: The energy band gaps of the conjugated polymers	61
Table 3: The absorption and emission wavelength maxima with the Stokes shift values and fluorescence quantum yield values	64
Table 4: The diffusion coefficient and surface concentration of the polymers	87
Table 5: The photovoltaic response of the polymers in the presence of PCBM as an acceptor under 1000 W cm^{-2} Simulated Solar Irradiation	102
Table 6: The photovoltaic response of the polymers in the presence of PCBM as an acceptor under 1000 W cm^{-2} Simulated Solar Irradiation	103



LIST OF ABBREVIATIONS

A	=	Electrode surface area (cm ⁻²)
Ag/AgCl	=	Silver/silver chloride reference electrode
C ₆₀	=	Fullerene
CT	=	Charge transfer band
CdS	=	Cadmium sulphide
CdSe	=	Cadmium selenide
CdTe	=	Cadmium telluride
CV	=	Cyclic voltammetry
DMSO	=	Dimethylsulfoxide
E _p	=	Peak potential
E _{pa}	=	Anodic peak potential
E _{pc}	=	Cathodic peak potential
F	=	Faradays constant
Fe ₂ O ₃	=	Iron oxide
Ga	=	Gallium
GaAs	=	Gallium arsenide
GaP	=	Gallium phosphide
HCl	=	Hydrochloric acid
HClO ₄	=	Perchloric acid
HOMO	=	Highest occupied molecular orbital
H ₂ SO ₄	=	Sulphuric acid
I _{max}	=	The current at which there is maximum power output
I _{pa}	=	Anodic peak current
I _{pc}	=	Cathodic peak current

I_{sc}	=	Short Circuit Current
ITO	=	Indium thin oxide coated glass
IR	=	Infrared
LUMO	=	Lowest unoccupied orbital
n	=	number of electrons
Np	=	Nanoparticle
OMA	=	<i>ortho</i> -Methyl aniline
PANi	=	Polyaniline
PANi-PSA	=	Polyaniline-phenanthrene sulfonic acid
PSA	=	phenanthrene sulfonic acid
PCBM	=	[6,6]-phenyl-C ₆₁ -butyric acid methyl ester
POMA	=	Poly-(orthomethyl aniline)
POMA-ASA	=	Poly-(orthomethyl aniline) –anthracene sulfonic acid
R	=	Gas constant
R_{ct}	=	Charge transfer resistance
SiC	=	Silicon carbide
aSi	=	Amorphous Silicon
SnO ₂	=	Tin (IV) oxide
T	=	Temperature in Kelvin (K)
TGA	=	Thermal Gravimetric Analysis
UV-vis	=	Ultraviolet-visible
V_{max}	=	The voltage at which there is maximum power output
V_{oc}	=	Open Circuit Voltage
WO ₃	=	Tungsten trioxide

XRD	=	X-ray Diffraction
Z	=	Impedance
ZnGa ₂ O ₄	=	Zinc gallate
ZnNO ₃	=	Zinc nitrate
ZnO	=	Zinc oxide



CHAPTER 1 :INTRODUCTION

1. 1 SYNOPSIS

The demand for energy has managed to exceed the supply. Tremendous amount of research came into being with the discovery of the photovoltaic effect by Alexandre Edmond Becquerel in 1839. This was further elucidated by Albert Einstein, who gave a detailed interpretation of the photovoltaic effect in 1905. The solar energy research was neglected by the lowered fuel prices in the 1970's. But with space research it became alive again [1]. Solar energy is generated upon absorption of photons by a semi conducting material; electrons are ejected and taken up by the electric field to produce charge [2]. This energy is stored in a battery. In a solar panel the semi conducting material is sandwiched between two electrodes, this component is what is referred to as a cell. These cells are connected together to form what is called the modules. These modules are connected together to form an array, which is referred to as a solar panel.

The main component of a photovoltaic device is the semi-conductor material, since it is the one that ultimately determines how much energy is taken up by the photovoltaic device. The most widely used semi-conductor is the crystalline silicon (90 %) [3]. This is because of the reported high efficiency (24%) in converting the light energy into electrical energy. They are also very stable. The amorphous silicon (a-Si) has also been explored for photovoltaic devices and it has been reported to have efficiencies of 13% but with time this goes down to 5% [4]. This has been attributed to the low stability of the a-Si that is caused

because of the breaking down of the hydride bonds with time. There is also what is called cadmium indium gallium selenide (CIGS). The development of the latter is challenged by the low efficiencies and also the fact that cadmium is a very toxic element. One of the challenges that hinder development of solar energy is cost of the materials since the most commercially used material (c-Si) is very expensive. This is a major reason organic materials are very attractive in photovoltaic devices research. Since organic materials are cheaper to process [5]. Inherently conducting polymers such as polyacetylene, polyaniline, polythiophene, polyparaphenylene, polypyrrole have been studied for potential as good conducting materials for photovoltaic devices [6]. The main problem with purely organic materials based photovoltaic devices is the recombination of the excited molecules upon absorption which limits the amount of energy that can be generated. This can be overcome by using a system that has a donor and an acceptor; the acceptor may be of a different nature to the donor. Hence in this work we investigate zinc gallate as a possible acceptor compound in the construction of solar cells.

1.2 AIMS AND OBJECTIVES OF RESEARCH

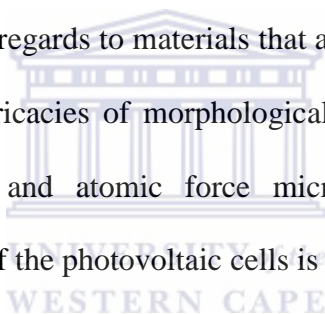
In this research the focus will be on developing polymeric materials based on polyaniline derivatives for use as donors in photovoltaic cells. The effect of the incorporation of nanoparticles based on zinc gallate will be investigated. The objectives that have to be achieved in accordance to the overall aim are as follows:

- (i) To synthesise polymeric material (based on polyaniline derivatives) and characterise the compounds using vibrational and electronic spectroscopy, photoluminescence, thermal gravimetric analysis (TGA), electron microscopy.
- (ii) To synthesise zinc gallate (ZnGa_2O_4) and characterise them using electronic and photoluminescence spectroscopy, electron microscopy.
- (iii) To study the electrochemical behaviour of the polymers.
- (iv) To construct and determine the efficiency of the polymer/ ZnGa_2O_4 composite with PCBM as an acceptor in photovoltaic cells.



CHAPTER 2 : BACKGROUND

The background looks at the history of photovoltaic cells. The different types that have been explored with the main focus being on organic solar cells as the work looks at organic materials as materials in photovoltaic cells. The operating principle of the organic solar cell is explained together with the types of materials that have been used so far within the research of organic solar cells. An emphasis is made on the use of polyaniline and its derivatives as a semiconductor. The potential good benefits of using polyanilines as a donor material in organic solar cells are explored. The importance of morphology in regards to materials that are used in photovoltaic cells is explored. As a result the intricacies of morphological techniques such as scanning electrochemical microscopy and atomic force microscopy are mentioned. The different device architecture of the photovoltaic cells is mentioned.



2.1 HISTORY OF PHOTOVOLTAICS

The photovoltaic concept was first reported by Edmond Becquerel, a French physicist, in 1839 using electrochemical studies of silver chloride coated platinum electrodes. Towards the late 1800's there were some significant research in regards to using selenium (Se) as the active layer by Adams and Day. Even though there was research done in the 1800s it is only upon the discovery of the photovoltaic effect by Albert Einstein in the 1960's. The solar energy research was neglected by the lowered fuel prices in the 1970's. But with the advent of space research it became alive again.

Solar energy is generated upon absorption of photons by a semi conducting material; electrons are ejected and taken up by the electric field to produce charge [7]. This energy is stored in a battery. In a solar panel the semi conducting material is sandwiched between two electrodes, this component is what is referred to as a cell. These cells are connected together to form what is called the modules. These modules are connected together to form an array, which is referred to as a solar panel, see **Figure 2.1**. The main component of a photovoltaic device is the semi-conductor material, since it is the one that ultimately determines how much energy is taken up by the photovoltaic device. The most widely used semi-conductor is the crystalline silicon (90 %) [8].

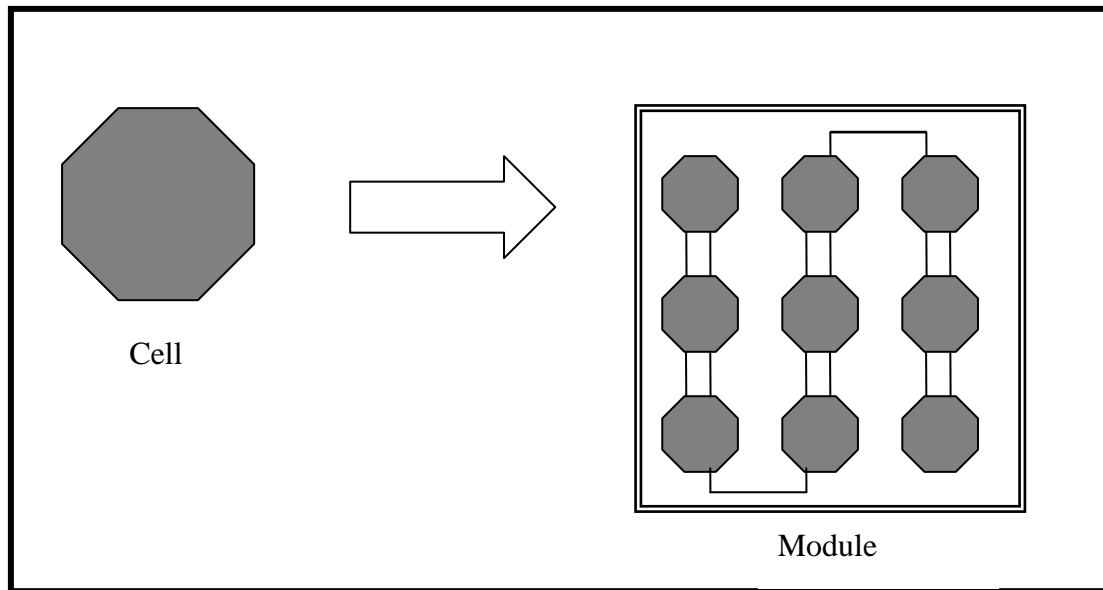


Figure 2.1: A figure depicting the formation of a module of a solar panel from a photovoltaic cell

2.2 TYPES OF PHOTOVOLTAIC CELLS

There are two main distinctions of solar cells, the inorganic and organic solar cells. The inorganic solar cells primarily consist of crystalline silicon (c-Si) which has been widely used owing to its high efficiency [9-11]. The emergence of thin film science has led to other materials such as, amorphous silicon (a-Si), cadmium indium gallium selenide (CIGS), being used for formation of inorganic solar cells [12-14]. Organic solar cells have been the primary area of research in solar cell technology because it is expected to lead to the formation of the solar panel at a lower cost in comparison with the c-Si.

2.2.1 Inorganic Solar Cells

An inorganic materials electronic bands consists of the conduction band and valence band, as shown in **Figure 2.2**, the photovoltaic effect is observed when upon exposure to light electron hole pairs are formed [15] with the holes at the valence band and the

electrons being in the conduction band. The holes go to the anode while the electrons go to the cathode allowing for the free flow of electric energy.

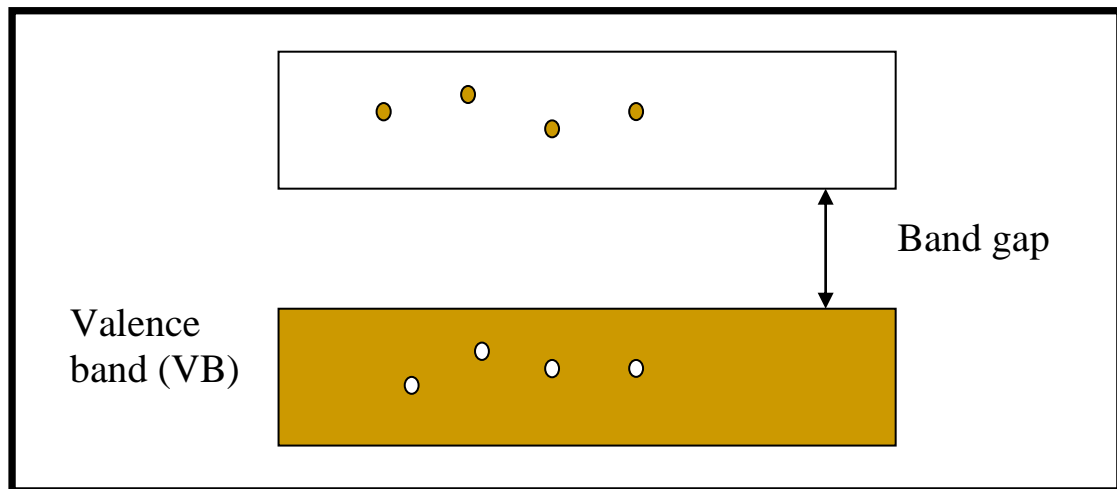


Figure 2.2: A diagram showing the formation of the electron hole pair at the conduction and valence band of an inorganic material

2.2.1.1 Silicon Solar Cells

The main semiconductor used in these materials is the c-Si because of its comparatively high efficiency and stability [16]. The stability is due to its well ordered structure, **Figure 2. 3**. The factor that hinders the spread of the use of solar energy using these materials is the high cost of c-Si. Since the materials cost a lot to process, it follows that for the consumers this will be an expensive source of energy making solar energy lack attractiveness. The development of thin films, has led to research on using the amorphous form of silicon [17-19]. This is preferable since a very thin layer of materials is used in the making of the solar cells based on the amorphous silicon. The disadvantage of this type is its very low stability [20] which is due to the fact that some hydrogen bonding is observed. When the materials are exposed to the sun they are reported to decompose because of the breaking of the hydrogen bond.

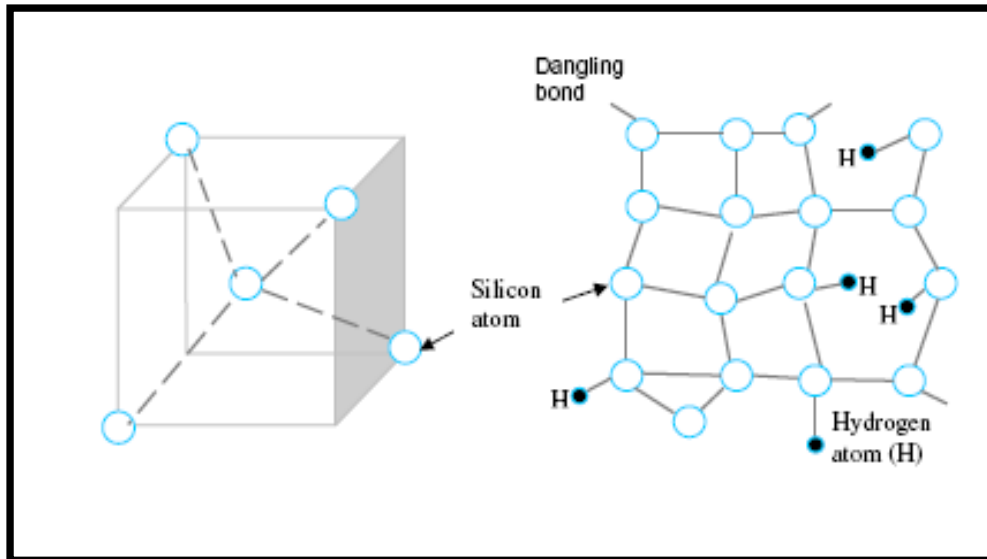


Figure 2.3: (a) c-Si well ordered, stable structure and (b) a-Si unstable structure

2.2.1.2 Nanomaterials

The advent of nanotechnology has led to the construction of nanomaterials based on cadmium indium gallium selenide (CIGS), CuInSe_2 , Cadmium Selenide (CdSe), Cadmium Telluride (CdTe) and Gallium Arsenide (GaAs) [21-23]. They have been reported to have an efficiency of up to 16 %. However selenium, tellurium and arsenic are very toxic. This makes materials that are based on these elements not ideal for the environment, hiking production costs. Since this is not ideal more research has gone in the use of materials such as zinc oxide and titanium dioxide for photovoltaic cell construction because it is less toxic.

2.2.2. Organic Solar Cells

Organic material based solar cells have garnered interest in the last two decades because of the high versatility in their chemical, electrical and optical properties [24]. They have opened a gateway in making solar cells at a lower cost with increased flexibility. The versatility also enables the use of substrates such as glass to make

solar cells, which further enhances organic solar cell technology's attractiveness. Conjugated organic materials are the ones that are used in solar cell technology as it displays a high conductivity, which is essential.

2.2.3.1 Operating Principle of an Organic Solar Cells

The operating principle of an organic solar cell works by utilising three concepts which are light absorption and charge generation, exciton diffusion and separation, charge carrier transport [25] as simulated in **Figure 2.4**. The organic material absorbs photons of light with enough energy to form a bound electron hole pair that is referred to as an exciton. The exciton is able to undergo charge separation using two routes. It can use electronic trap sites when one type of material is used. The latter produces organic solar cells that have low efficiencies [26-28], as there is a higher probability of charge recombination. Currently the most widely used method is the use of two materials (a donor and acceptor) with different electron affinities, this allows for a separation of the holes from the electrons at the interface of the materials [29]. In a typical system, the absorbing material (donor) acts as a hole charge carrier while the one with the greater electron affinity (acceptor) acts as an electron charge carrier to the designated electrodes, anode for the holes and cathode for the electrons.

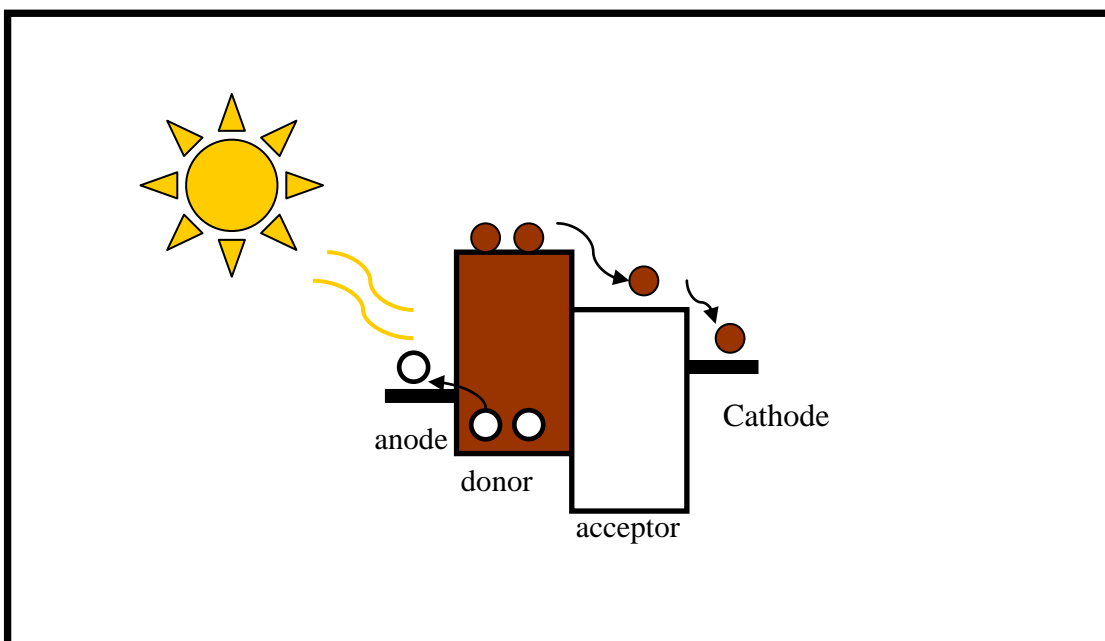


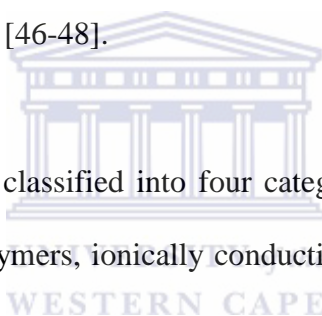
Figure 2.4: Schematic representation of the operating principle of an organic solar cell

2.2.3.2 Materials used

There are different areas within organic solar cells, there are purely organic solar cells, hybrid solar cells and dye sensitised solar cells [30-34]. The purely organic solar cells use only organic materials as donor and acceptor. Polymers such as polythiophenes, polypyrrole, polyaniline and their derivatives have been used as donors in these types of cells [35-38]. In these purely organic materials, reported in literature, fullerene (C_{60}) is used as an electron acceptor because of the relative good electron charge mobility [39-40]. The reported hybrid solar cells utilise organic molecules such as polymers as semi conductors of donors and inorganic nanoparticles such as zinc oxide and titanium dioxide as acceptors. Research has been mostly based on the hybrid type of solar cells since they have shown to have better efficiency because of the different electron affinities between the compounds. The research has further been encouraged by great strides in nanoscience.

2.2.3.2.1 Conducting Polymers

For a number of years, polymers have been prized for their insulating abilities [41-43], hence their use as a plastic rubber over electrical wires. This is because traditional polymers could only act as insulators as their energy band gap is very wide and hinders electron conductivity. They have since been discovered that they have some electrical conductivity which makes them important semiconductors [44-45]. The semi-conducting ability of the conducting polymers is because they have a much narrower bandgap in comparison with its insulator counterparts. The latter allows for the movement of the electrical charge. The semi conducting ability has led to an expansion in the uses of polymers; they have since found a niche in manufacturing of electronic displays, as sensors [46-48].



Conducting polymers can be classified into four categories, conjugating conducting polymers, charge transfer polymers, ionically conducting polymers and conductively filled polymers [49]. The focus will be on conjugated conducting polymers. It can be noted in **Figure 2.5** that for the conjugated polymers an alternating network of single and double bonds runs over the whole polymer chain, this concept is the one that makes the polymers to be termed intrinsically conducting. This arises because in comparison with its metal counterpart, which is highly conducting because of the liberated movement of electrons over the structure, the polymer also has that capability due to the overlap of the π -orbitals over the polymer chain. In the polymer network of conjugated polymers the atoms are sp^2 hybridised. In this state, the π -orbitals are able to overlap to generate two energy levels, one occupied by electrons and one not having the electrons. These are generally referred to as the highest occupied molecular orbital (HOMO) or π -bonding and the lowest unoccupied

molecular orbital (LUMO) or π -antibonding. A bandgap is formed in between these orbitals. In polymers the size of the bandgap is dependent on the length of conjugation, the longer the length of conjugation the smaller the band gap. Depending on the size of the band gap a compound can be classified as either an insulator, semi conductor or a conductor.

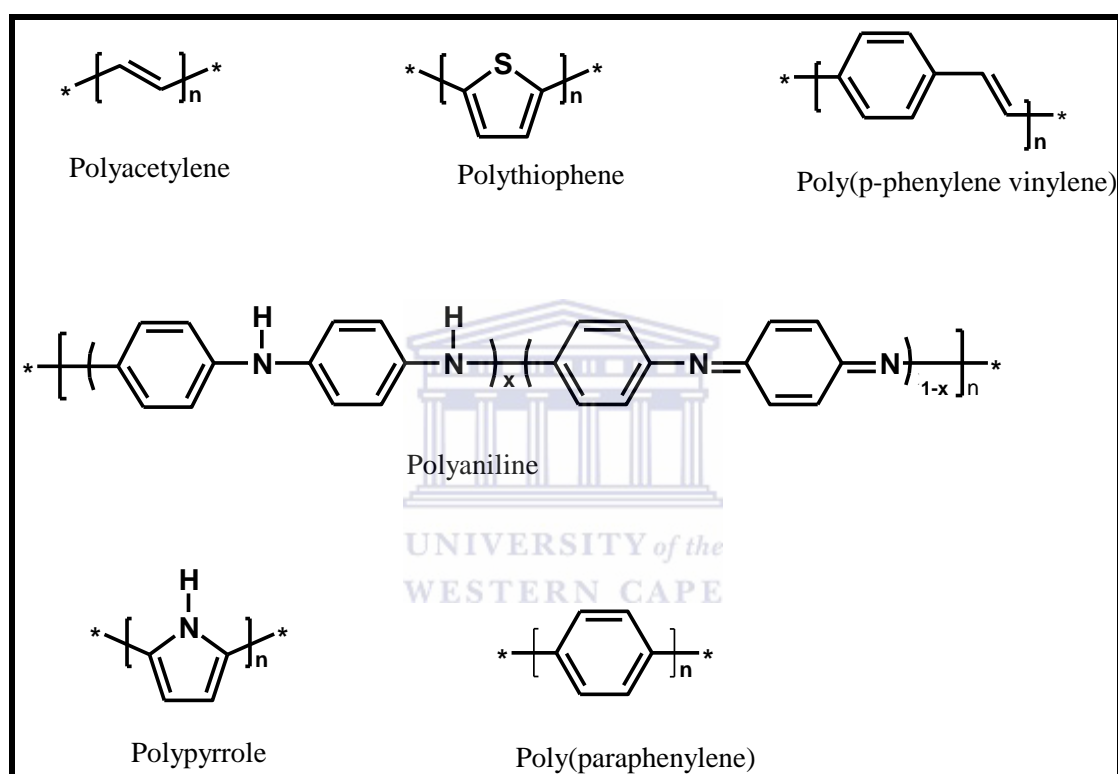


Figure 2.5: Diagrams showing typical conjugated conducting polymers

The conjugated polymers are used as donors in the construction of organic photovoltaic cells. The most commonly used polymer is the poly(p-phenylene vinylene) (PPV) [50] and its derivatives such as poly[2-methoxy-5-(2'-ethoxyhexyloxy)-1,4-phenylene vinylene] abbreviated MEH-PPV [51-53], polythiophene and its derivatives [54-56] and one based on polyanilines [57], **Figure 2.5**. Use of polyanilines in photovoltaic materials is limited in comparison with the other

polymers. This is because the polyaniline has a relatively much lower conductivity in comparison with the other polymers. However research in the recent past has focused on polyaniline because it can be tailored to give high conductivity values [58].

2.2.3.2.2 Synthesis of the Conductive Polymers

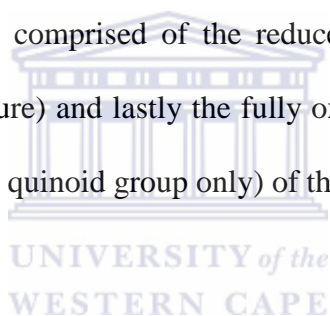
Polymers can be synthesised using chemical methods [59-60]. One of the chemical methods is the use of oxidising agents to form polymers [61]. This type of polymer synthesis is referred to as cationic polymerisation. The formation of the chain is initiated by the occurrence of a cation upon oxidation, a monomer species reacts with the active cation to form another active cation center, this continues until the subsequent termination of the process. The chemical synthesis of polymers does not allow for efficient control of the specific length of the polymer chain.

Another process that is utilised for the synthesis is electrochemical polymerisation [62-63]. This process allows for the formation of a polymer with a specific chain length, no mixtures are formed. This makes the electrochemical method of synthesis be considered as the 'cleaner' form of synthesis. Other excellent traits displayed by electrochemical method are its simplicity, reproducibility and the added advantage of obtaining a conducting polymer being simultaneously doped. Photochemical polymerisation [64-65] has also been reported in the synthesis of polymers. Photosensitizers are needed to act as photon absorbers to initiate a polymerization reaction. Conducting polymers have also been synthesized by other techniques such as metathesis polymerization (Ziegler-Natta polymerization) [66-67], plasma polymerization [68-69], chain polymerization [70-71], step growth polymerization

[72], concentrated emulsion polymerization [73], chemical vapour deposition [74], solid-state polymerization [75].

2.2.3.2.3 Polyaniline

Polyaniline is one of the oldest known conjugated polymers. It was first reported in 1862. Polyaniline is a compound that is formed from the chain propagation of aniline. The polyaniline structure has been elucidated to have five oxidation states [76] but there are three forms of PANi that have been successfully synthesised and isolated using a chemical method, they are depicted in **Figure 2.6**. There is the fully reduced (benzenoid structure) state referred to as the leucoemeraldine, emeraldine which exists with half of the chain comprised of the reduced form and another half the oxidised form (quinoid structure) and lastly the fully oxidised form, pernigraniline is the fully oxidised form (imine quinoid group only) of the polymer.



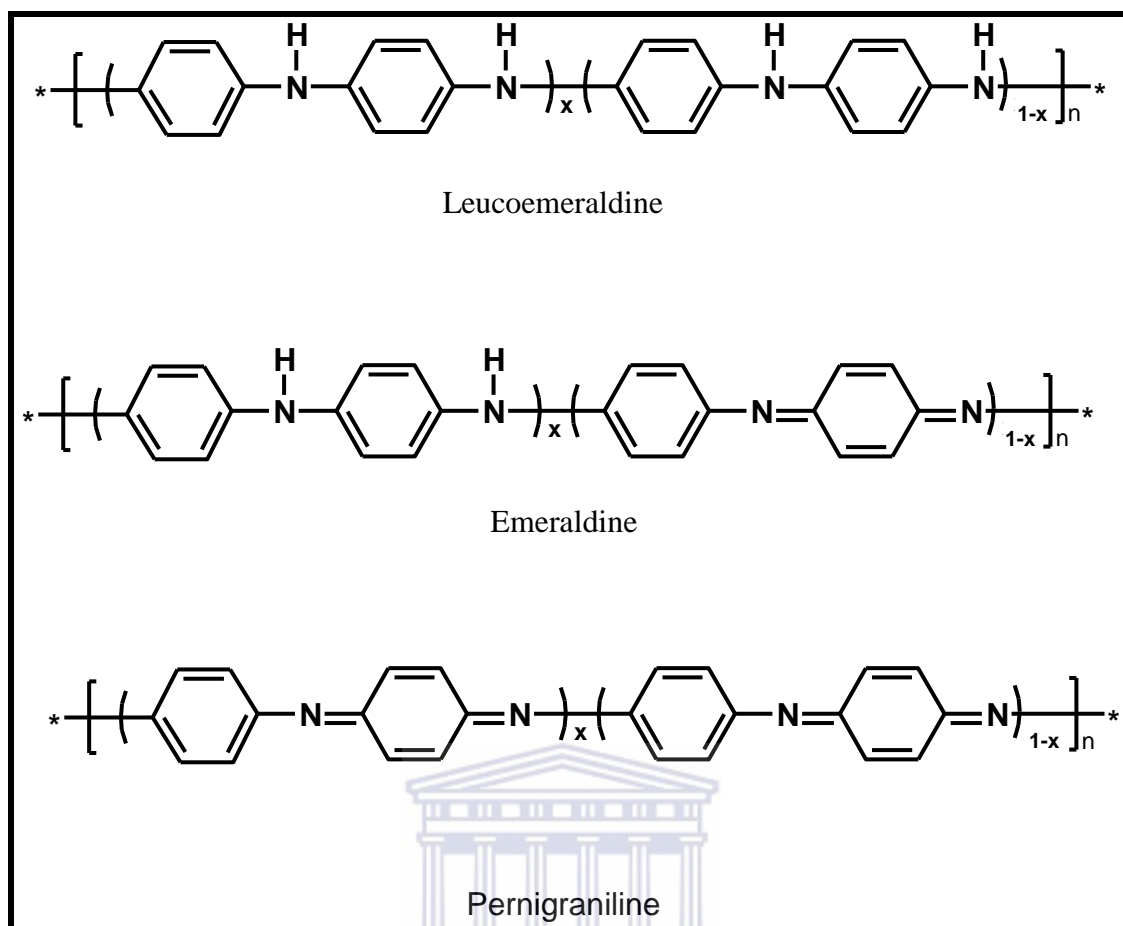


Figure 2.6: The intrinsic redox states of polyaniline

The synthesis of polyaniline has been achieved using chemical and electrochemical means in acidic conditions [77-78]. The chemical oxidative polymerisation of PANi occurs via two steps, the induction step and chain polymerisation step as shown in **Figure 2.7**. The induction step involves the oxidation of the aniline by the oxidant to form a radical cation. The radical cation acts as an oxidant of the monomeric unit, aniline. This is followed by the recombination of the radical cations to form the dimer species. The chain propagation occurs by the oxidised dimer nitrogen unit attacking the *para* position of the monomeric aniline.

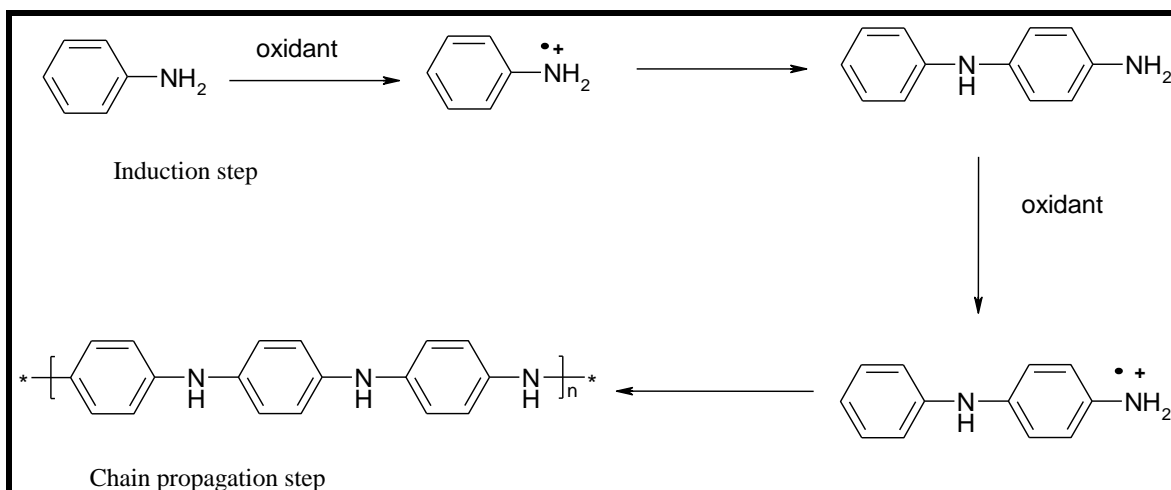


Figure 2.7: Schematic representation of the chemical polymerisation of aniline

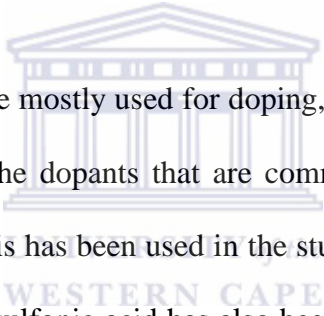
2.2.3.2.4 Poly(*ortho*-methoxyaniline) (POMA)

Poly(*ortho*-methoxy aniline) is a derivative of PANi that has a methoxy group as a substituent at the *ortho* position. The monomer of this derivative is *O*-methoxyaniline. The substitution leads to an improved solubility of the polymer in organic solvents [79]. This is as a result of the improved polarity of the polymer chain because of the substituent. Increase in solubility leads to a lowered conductivity as substitution at the phenyl or *N*-position of polyaniline leads to a decrease in the conductivity. The synthesis of POMA can also be done electrochemically or chemically. The intrinsic redox states that are formed are the same as the ones that are observed for PANi.

2.2.3.2.5 Doping

As previously stated when looking at the mechanism of operation of a solar cell, it is vital for the polymer to have charge carrying ability. The charge carrying ability of the polymer in its neutral state is limited. It is important to utilise processes such as doping to improve the charge carrying ability of the compounds. The compound can

be doped by partial oxidation of the compound or partial reduction of the compound [80]; these are referred to as p-doping and n-doping, respectively. The doping process affects the electronic structure of the compound. Upon doping of the polymers there is generation of charge defects such as polarons, bipolarons and solitons [81]. The polaron forms as a result of the removal of electrons from the HOMO, this leads to the HOMO being partially filled and a radical anion is formed. As a result of this energy states are formed within the HOMO-LUMO energy band gap. When an additional charge is removed within a chain bipolarons are formed. The polarons have both spin and charge, but the bipolarons are spinless. The effect of the doping process is seen on the optical spectrum by the appearance of peaks at lower energies.



There are two methods that are mostly used for doping, chemical and electrochemical doping. In chemical doping the dopants that are commonly used are iodine, which acts as an oxidizing agent. This has been used in the study of polyacetylene [82]. The use of protonic acids such as sulfonic acid has also been reported [83-84]. The use of acids does not change the number of electrons related to the backbone of the polymer chain. It only leads to the rearrangement of the energy levels. The most common polymer in regards to protonic doping is polyaniline. Due to the highly conjugated structure of the conjugated polymers, they are able to undergo redox processes very easily. This makes it possible to easily move from a p-doped species (reduced) to an n-doped species (oxidised). There is also control of the doping levels of the compound.

2.2.3.2.5 Charge Carriers in Conjugated Polymers

As previously stated there is formation of various charge carriers such as solitons, polarons and bipolarons upon doping of the conjugated polymers. The types of charges that are formed are dependent on the molecular structure and the level of doping.

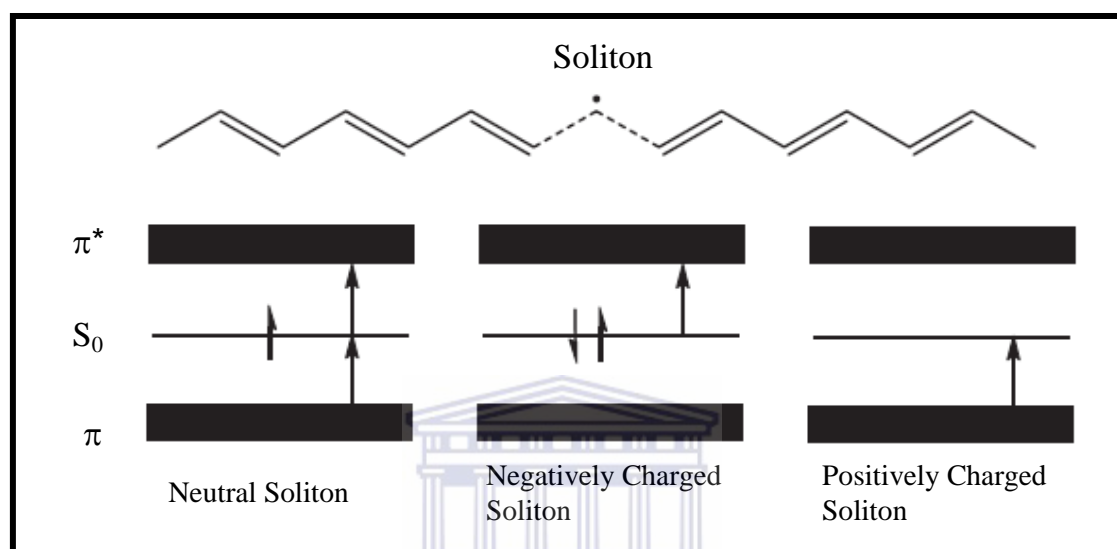


Figure 2.8: Schematic representation of the soliton charge defect that can be observed in conjugated polymers

The formation of the soliton occurs in compounds that have geometric structures that correspond to exactly the same energy [85] as depicted in **Figure 2.8**. The soliton can propagate freely along the polymer chain, as its two sides possess identical energy. In a long chain, the unpaired electron in a neutral soliton (or a charge in a charged soliton) will not be localized on one carbon but rather will be spread over several carbon atoms (up to 14), which causes the soliton to have a width. Although the bond lengths are equal at the middle of the soliton, starting from one side of the soliton the double bonds become gradually longer and the single bonds shorter; consequently, on reaching the other side of the soliton the alteration is completely reversed. The presence of a soliton leads to the appearance of a localized electronic level at mid gap, which is half occupied in the case of a neutral soliton and empty(doubly occupied) in

the case of positively (negatively) charged soliton. Upon increasing the doping level, soliton states at midgap begin to overlap and to form a soliton band.

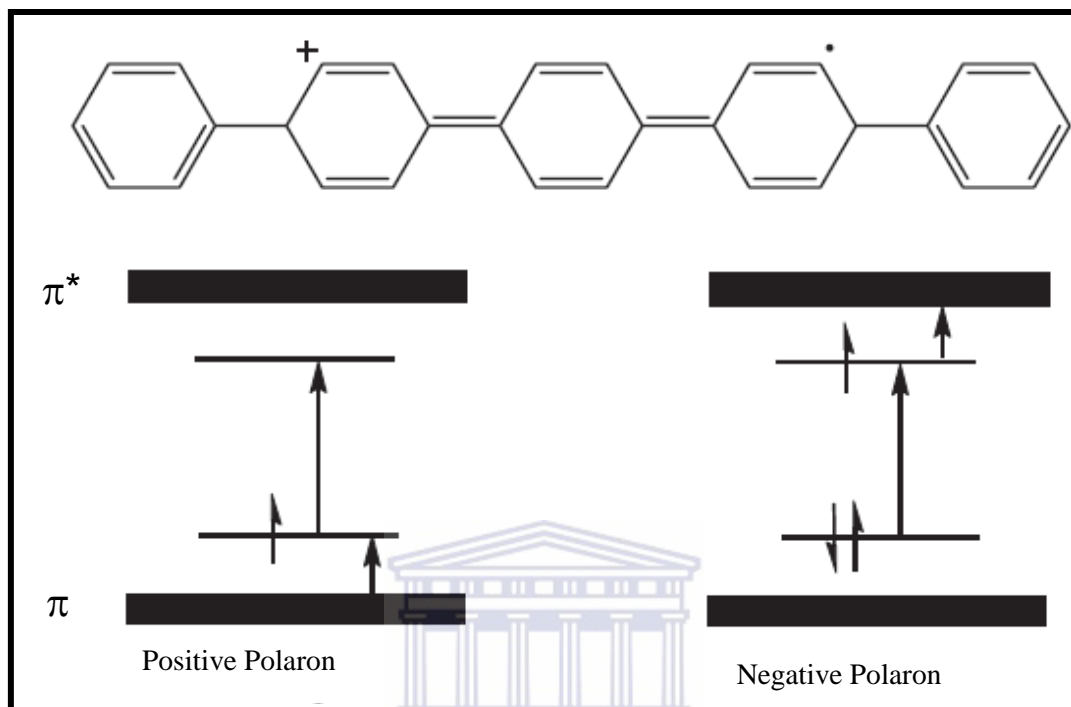


Figure 2.9: Schematic representation of the polaron charge defect that can be observed in conjugated polymers

Another type of charge defect that is mostly observed in polymers such as polyaniline and polypyrrole [86-87] is called the polaron and the schematic representation of the charge polaron charge defects is given in **Figure 2.9**. These are able to form in polymers with geometries that are not necessarily at the same energy level. In such polymers, the main charged excitations are radical ions strongly coupled with lattice distortion; these are termed polarons (a positive polaron in the case of a radical cation, and a negative polaron in the case of a radical anion). The net charges in polarons are the result of chemical reduction/oxidation, electrochemical charge injection, or photoinduced charge transfer. The local lattice distortion tends to localize the charge.

Although polarons can propagate along the polymer chain, the propagation length is strongly limited by conjugation interruptions. It is also possible for a polaron to jump from one chain to another if the acceptor chain possesses a similar lattice distortion to the donor.

A bipolaron [87] is a pair of charges of the same sign (dual cations or dual anions) that is coupled to lattice distortion. The schematic representation of the bipolarons is given in **Figure 2.10**. Bipolarons are similar to polarons, but have larger lattice distortions and begin to dominate at a large doping extent or a high charge injection rate. Two polarons of the same sign can combine to create a bipolaron, the formation of which implies that the energy gained by the interaction with lattice is larger than the Coulombic repulsion between the two charges of same sign, confined in the same location.

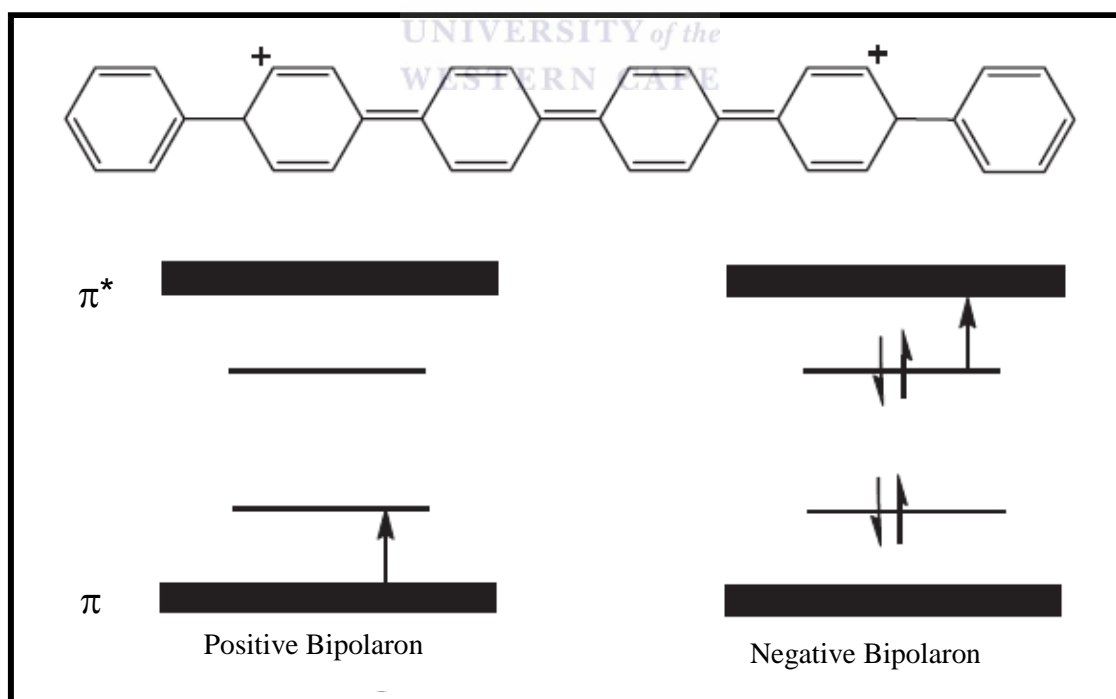


Figure 2.10: Schematic representation of the bipolaron charge defect that can be observed in conjugated polymers

2.2.3.2.6 Importance of Photoluminescence in Photovoltaic cells

The transitions that occur upon excitation of a compound are represented by means of a Jabłoński diagram [88], **Figure 2.11**. When we consider the Jabłoński diagram, we have the singlet ground state which is denoted as S_0 , in this state the HOMO level of the organic compound which is in this instance a polymer is expected to be occupied with two electrons of opposite spin. Upon absorption of light there is movement of one of the electrons to the LUMO level without alteration of the spin of the electron, this is referred to as the singlet excited state, S_1 or S_2 , of the compound. The disintegration of energy from the excited singlet excited can occur via internal conversion to the lowest vibrational mode of the excited state followed by fluorescence from the lowest vibrational level of the excited state to the ground state. This is referred to as a spin allowed transition. Since there is no change in the state it has short lifetimes, measured in nanoseconds. There is also the occurrence of spin disallowed transitions, this occurs when there is change of the spin of the compound at the excited state. They occur as a result of spin-orbit coupling which results in the intersystem crossing of the compound to the triplet state. Since it is a disallowed transition it is long lived, with lifetimes measured at microseconds. The energy decipation can occur via phosphorescence from the excited triplet state.

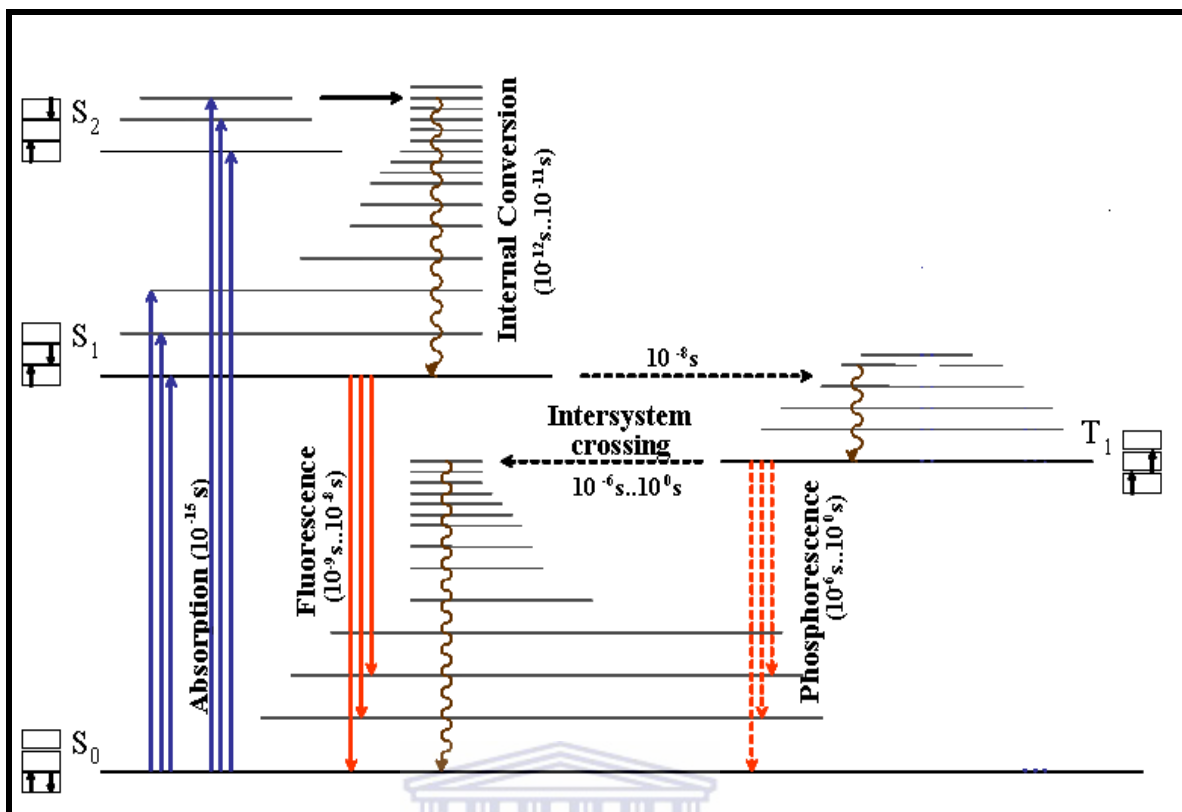


Figure 2.11: Jablonski diagram representing the processes that occur upon photoexcitation

The transition that we will be focusing on is fluorescence, since it is a photophysical tool that has been used to interrogate materials that are applicable in photovoltaic cells [89]. The vibrational modes that occur in fluorescence are supposed to be the same as the ones that are denoted in the absorption spectrum of the molecule but occurring at lower energies. A change in the vibrational modes can occur as a result of the change in the geometry of the compound at the excited level. In this instance fluorescence is a good tool for monitoring whether there are significant geometrical changes in the compound upon excitation so as to know that the materials that is used in photovoltaics is the same as the original compound. In polymers or organic compounds there are instances when there are transitions that are observed in fluorescence but not absorption spectra [90]. These transitions occur as a result of formation of excimers or exciplexes. They are referred to as excimers or exciplexes

depending on whether the excited complex is as a result of the interaction between two molecule of the same nature (excimers) or different nature (exciplexes). The excimers or exciplexes are as a result of the interaction of the excited molecule with a molecule that is at its ground state. This leads to a formation of an excited complex whose energy is decipated by fluorescence. The complex disintegrates at the ground state, hence no occurrence of the transitions at the ground state.

As previously stated in organic photovoltaics there is a donor and acceptor, fluorescence is one of the best photophysical tools that is used to look at the interaction of the acceptor and donor at the excited level. This is because with the fluorescence it is possible to monitor the decipation of the emitted energy of the donor compound by the acceptor compound. The decipation of energy in the presence of a donor and acceptor leads to two other possible transitions that can occur besides fluorescence of the donor compound. There is photoinduced charge transfer and excitation energy transfer [91-92]. Upon excitation of the donor species one of the electrons that occupies the HOMO level jumps to the LUMO, this means that one of the electrons has gained more energy and can be easily donated. However the HOMO has become half occupied and can easily accept electrons from a reductant, this state describes a photoinduced electron transfer process and is illustrated in **Figure 2.12**. One can conclude whether there is photoinduced electron transfer, from the donor to the acceptor upon excitation by the total quenching of the fluorescence of the donor. This is dependent on whether there electron transfer occurs at a faster rate in comparison with the fluorescence decay. In organic photovoltaics it has been observed that the use of fullerenes as an acceptor allow for more efficient electron

transfer processes [93]. This is because the electron transfer process occurs at a faster rate than fluorescence in the presence of fullerene as a donor.

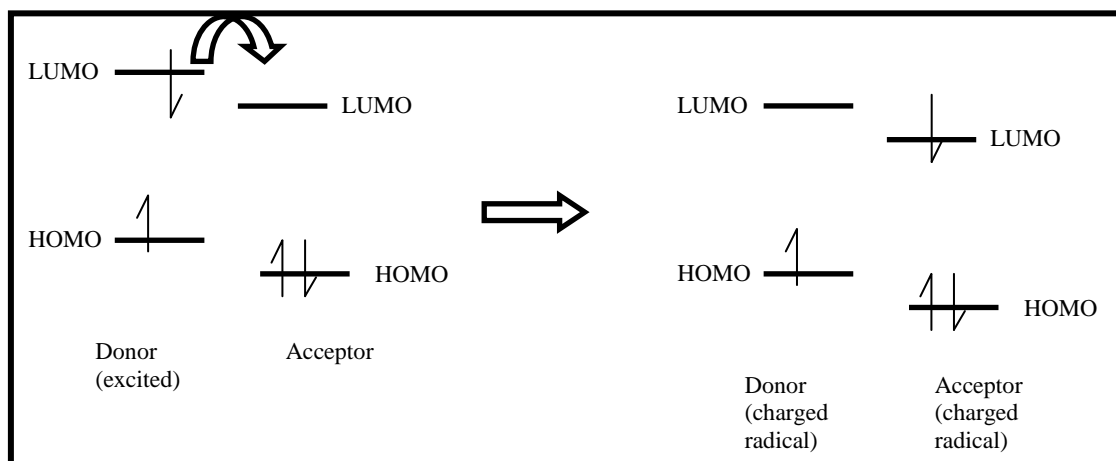


Figure 2.12: Schematic representation of the photoinduced electron transfer process

2.2.3.5 Acceptors in Organic Solar Cells

A list of the acceptors that are currently used in solar cell technology with their band gaps is shown in Table 1. The bandgap for the single walled carbon nanotube (SWCNT) is not supplied because it varies depending on the chirality and also the diameter of the SWCNT [94]. In purely organic solar cells there has been exploration of the use of fullerenes as electron acceptors. This is because they have a high electron affinity in comparison with other organic compounds such as polymers [95]. Light induced processes (in the presence of fullerene and polymers) such as fluorescence quenching have been observed because of this characteristic. This factor makes fullerenes good electron acceptors. They are able to carry up to six electrons per molecule. There are acceptors based on nanomaterials (listed in Table 1), such as titanium dioxide, zinc oxide that have been used for hybrid solar cells [96]. The inorganic nature of the compounds makes them good as electron carriers in solar cells. Considerable interest has gone into utilising these inorganic acceptors because

they can be tailored using inexpensive methods such as wet chemical synthesis. Other reports include the use of GaAs [97-98], tungsten trioxide (WO₃) [99], single walled carbon nanotubes [100-101], tin dioxide (SnO₂) [102] as acceptors in photovoltaic cells.

Table 1: The band gaps of materials commonly used as electron acceptors

Material	Band Gap (eV)
C ₆₀	2.27
PCBM	2.35
SWCNT	
TiO ₂	3.20
CdS	2.25
CdSe	1.70
CdTe	1.73
SiC	3.00
SnO ₂	3.80
WO ₃	2.60
GaAs	1.40
GaP	2.25
ZnO	3.20
Fe ₂ O ₃	2.10

2.3 DEVICE ARCHITECTURE

In photovoltaic cells the active layer is inserted between two electrodes that are referred to as the anode and cathode. The anode is an electrode made that is

transparent, indium thin oxide (ITO) is often used, and the other electrode referred to as a cathode is an electrode that can be made from aluminium or calcium. Aluminium is preferred over calcium because it is more stable in air. Different device designs arise as a result of the way the active layer (donor and acceptor) compounds are incorporated on the electrode. There are four types of device architecture in organic photovoltaic cells; single layer cells, bilayer heterojunction, bulk heterojunction and hybrid heterojunction. They are illustrated in **Figure 2.13**.

2.3.1. Single-layer Cells

This type of architecture uses one type of compound in the active layer of the cell and as illustrated in **Figure 2.13** [103]. This means that the polymer compound would be expected to act as an electron carrier. It has been proven that the polymers are more liable to carry holes than electrons. Another factor that makes this type of architecture not desirable is that high recombination has been experienced. The mentioned factors lead to photovoltaic cells with very low efficiencies. This type of architecture is mostly used when studying properties such as current densities.

2.3.2 Bilayer Heterojunction

The bilayer heterojunction uses the concept of using a donor and an acceptor. These compounds must have different electron affinities and ionisation energy to allow for the efficient transfer of charge between them. As the name implies the compounds are introduced layer by layer. The limitation of this type of cell is that there is a small interface area between the donor and acceptor. Sariciftci *et.al* were one of the first groups to report on the formation of organic solar cells using the layered method [104]. They used ITO as the transparent electrode and MEH-PPV was spin coated on

the electrode followed by the fullerene moiety. This was also the first report on the use of fullerene as an electron acceptor.

2.3.3 Bulk Heterojunction

The concept of bulk heterojunction was first introduced by Halls *et.al* in 1995 [105] in order to combat the limitation experienced by bilayer heterojunction, which is the small interface area between the donor and acceptor. Bulk heterojunction also uses the donor-acceptor concept with the only difference being that the two compounds are ‘blended’ together. This maximises the interface area between the donor and acceptor which ultimately leads to more excitons being able to reach the donor-acceptor interface. Yu *et.al* also looked at the blended type of solar cell design, they used MEH-PPV and PCBM, these achieved efficiencies of 2.3% [106]. The results are higher than when the same type of materials was used in bilayer heterojunction. Since this discovery there have been various reports on the use of bulk heterojunction in the formation of solar cells.

2.3.4 Hybrid Heterojunction

A very different kind of heterojunction has emerged as a result of trying to improve the efficiencies of organic solar cells; this is the hybrid heterojunction [107-108]. The hybrid heterojunction utilises the two concepts practised in bilayer heterojunction and bulk heterojunction, with the only difference being that there is use of an organic and inorganic compound in the active layer of the cell.

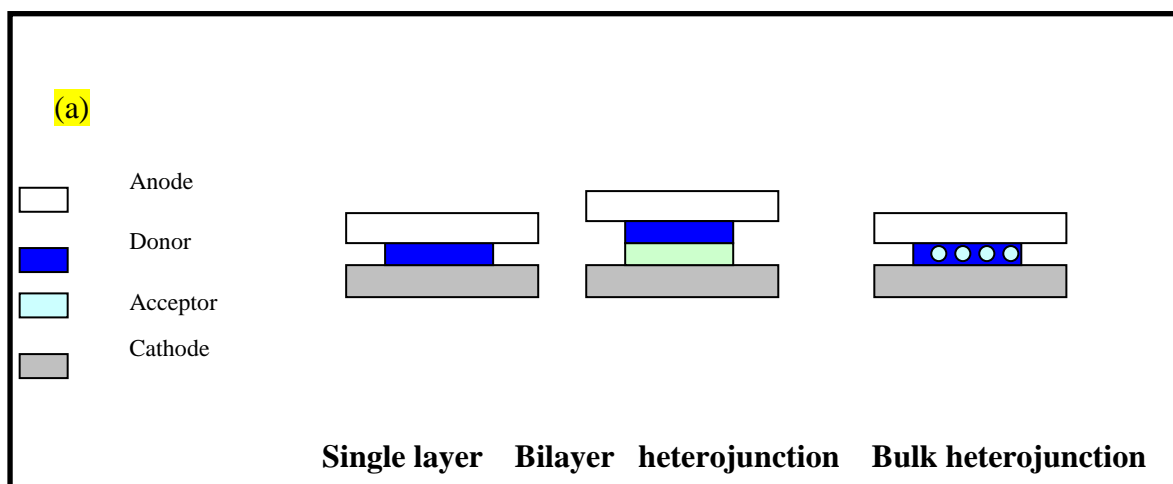


Figure 2.13: Schematic representation of the device architecture in solar cells

2.4 CHARACTERISATION TECHNIQUES FOR PHOTOVOLTAIC CELL MATERIALS

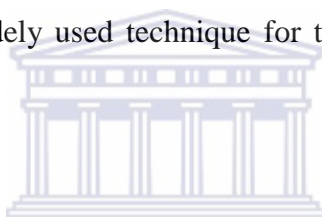
2.4.1 Morphology

Morphology is one of the main factors that affect the efficiencies of solar cells. A lot of research has focused at looking at different forms of polymers and how their morphology can affect the efficiency of solar cell [109-110]. It has been discovered that materials that form long tubular structures display high efficiencies due to an enhanced interface contact between the donor and acceptor. The techniques that make it possible to look at the morphology are scanning electron microscopy (SEM) and transmission electron microscopy (TEM).

2.4.1.1 Scanning Electron Microscopy (SEM)

SEM is a powerful technique that utilises a scanning probe that moves over the surface of the compound in order to form an image. The scanning probe is a focused electron beam. There are three signals that occur in response to exposure to the

electron beam, there are secondary electrons, backscattered electrons and x-rays. The secondary electrons are the ones that are detected for the development of a SEM image. These are emitted at relatively low energies, 50 eV; they are from the top surface of the compound. As a result with SEM it is possible to only look at the surface morphology of the compound. The image is developed as the scanning probe moves along the sample under analysis. The backscattered electrons are from the beam that have been elastically scattered by nuclei in the sample and escape from the surface. Backscattered electrons have higher energy and are able to give information regarding sample composition. This capability is enhanced in combination with the x-rays. The performance of a SEM instrument is largely dependent on the electron source. SEM is the most widely used technique for the analysis of morphology of polymers.



2.4.1.2 Transmission Electron Microscopy (TEM)

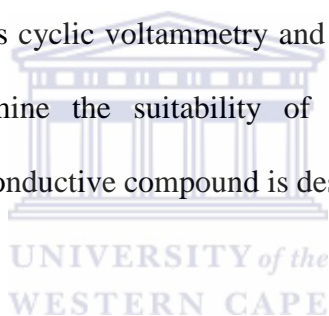
The transmission electron microscopy develops an image based on the interaction of the compound under analysis with the electron beam. In the case of the TEM, it is possible to analyse large areas at once instead of the small areas that are analysed with SEM. As with SEM a field emission gun is used as an electron beam. The images that are supplied by TEM for polymers are not that well resolved as there is the problem of phase contrast in the analysis of polymers using electron microscopy techniques. TEM is useful in resolving the degree of crystallinity of the polymers as it is possible to see the way in which the polymeric chain is folded on itself.

2.4.2 Thermal Gravimetric Analysis

This technique is used to determine the thermal stability of the compounds. This is a very important factor when considering materials for use in photovoltaic application. This is because the material will be exposed to high temperatures, it is advantageous to make that the materials that are used are stable at high temperatures. A good thermally stable donor material for application in photovoltaic cells has been reported to undergo decomposition at temperature that is higher than 300 °C.

2.4.3 Electrochemistry

The electrochemistry of donor and acceptor can be investigated by using voltammetric methods such as cyclic voltammetry and electrochemical impedimetric methods. This is to determine the suitability of the compound in terms of conductivity, since a highly conductive compound is desired.



2.4.3.1 Voltammetry

Cyclic voltammetry involves the reduction and oxidation of the species. Oxidation occurs on application of a positive potential, an increase in the peak current with an increase in the potential is observed until the potential of the analyte is reached, Figure 2.4. Thereafter a decrease in current occurs. The reoxidation of the species occurs with application of a positive potential. The movement of the species to the electrode can be facilitated by migration, convection and diffusion. Diffusion is the movement of analyte due to concentration gradient. The latter is the one that is of interest when dealing with electroanalytical reactions. When working with voltammetry, specifically cyclic voltammetry, a system can be characterised as a reversible, quasi-reversible and irreversible. This is dependent on the ease of the

redox reaction of the species and whether both the oxidised and reduced species are redox active. A reversible system shows the redox reaction of the species in the forward scan followed by the redox reaction upon application of a reverse scan, the Nernst equation applies to this system. The ratio of the reverse to forward peak currents is equal to unity for this system. ΔE (anodic to cathodic peak potential separation) is $\sim 59 \text{ mV}/n$ for a reversible system.

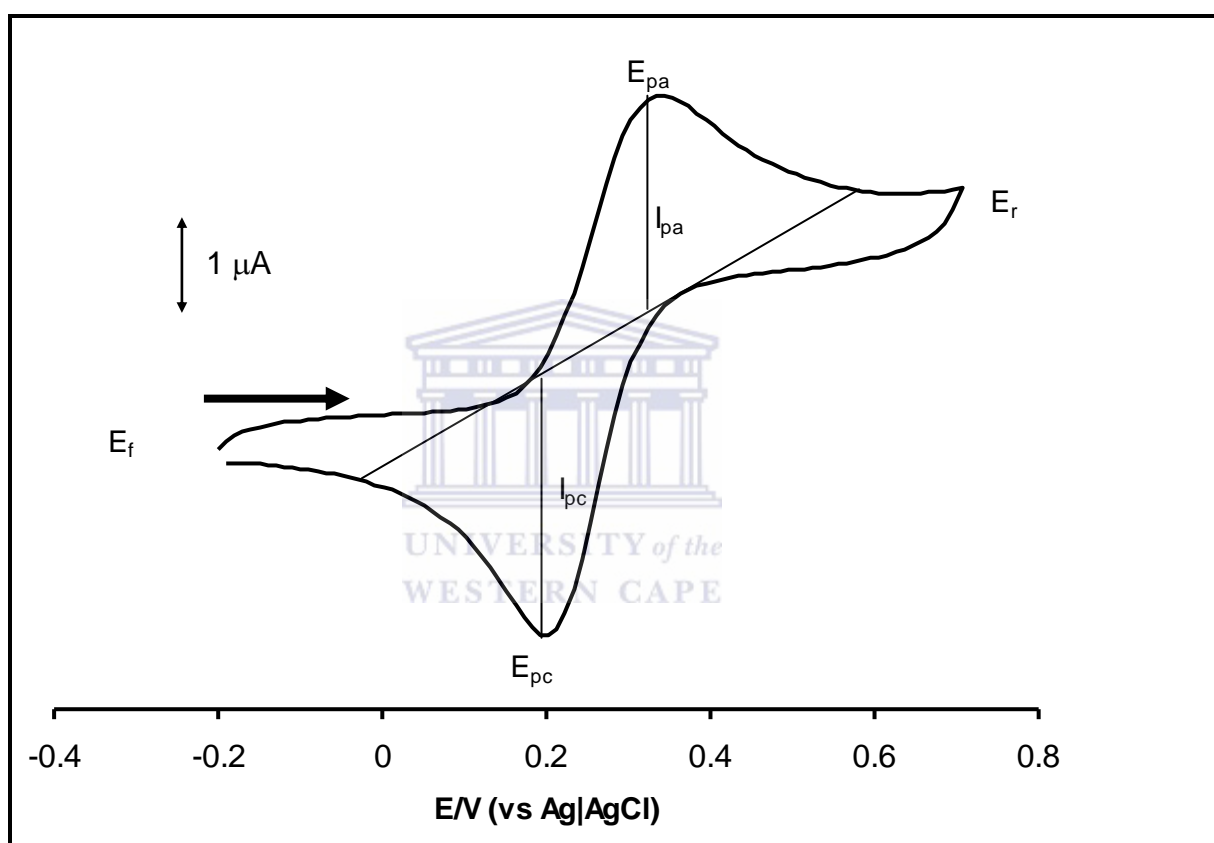


Figure 2.13: A typical cyclic voltammogram for a reversible system

The number of electrons transferred in this system is determined using equation 2.1

$$\Delta E = \frac{RT}{nF} = \frac{0.059 \text{ V}}{n} \quad 2.1$$

where R is the universal gas constant, T is the temperature in Kelvin and F is the Faraday's constant (96485 C mol^{-1}). The half wave potential is determined using equation 2.2

$$E_{1/2} = \frac{E_{pa} + E_{pc}}{2} \quad 2.2$$

The system is said to be quasi-reversible when the equilibrium concentration is not maintained between the redox species. This results in ΔE values that are greater than 59 mV for a one electron system with I_{pa}/I_{pc} deviating from unity. An irreversible system is observed by the occurrence of a forward peak with a peak in the reverse direction being very weak or not observed at all due to failure to regenerate the starting electroactive species. A shift in the potential with change in scan rates is observed with an irreversible system because of the slow electron transfer.

2.4.3.2 Electrochemical Impedance Spectroscopy (EIS)

Electrochemical impedance spectroscopy is a technique that uses an applied sinusoidal voltage which gives a response in the form of current. The technique is effective in interrogating surfaces, these include surface modified electrodes. EIS measurements allow for the proper quantification of the capacitive effect of a particular material at different frequencies. The impedance data is dependent on the frequency that is applied and the relationship between the two is expressed in the equation below:

$$Z(j\omega) = Z'(\omega) + jZ''(\omega)$$

where Z' and Z'' are the real and imaginary impedance terms, respectively; $j = \sqrt{-1}$ and is an imaginary number while ω is the radial frequency (rad. s^{-1}) and equals $2\pi f$, f

being the exciting frequency (Hz). The EIS data can be represented using two forms, Nyquist and Bode plots.

A typical Nyquist plot is shown in **Figure 2.14**. As can be seen from **Figure 2.14**, the Nyquist plot is a plot of the imaginary versus real impedance terms. A typical plot consists of the semi circle part which is a representative of the capacitive effect of the material. This part is the one that is used to deduce the charge transfer resistance of the material. This is because the diameter of the semi circle is considered the actual value of the charge transfer resistance. The linear region of the plot is indicative of diffusion controlled electrochemical processes. Since the impedance is dependent on the frequency, the high frequency side on a Nyquist plot is denoted by the left side of the diagram and the low frequency side by the right side of the diagram. Considering the latter, it is seen that the semi circle is observed on the high frequency side with the linear part at the low frequency region. The major limitation with presenting data using a Nyquist plot is that the frequency at any given data on the plot is not annotated. It has to be calculated.

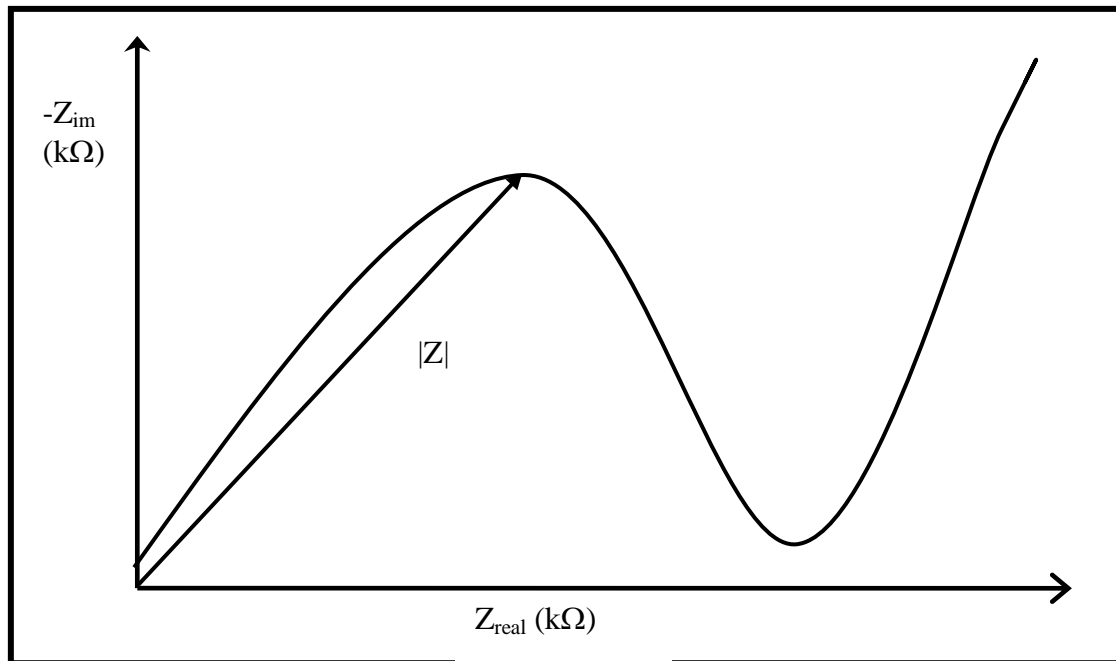


Figure 2.14: The schematic representation of a Nyquist plot

The total impedance is affected by several parameters these include the electrolyte solution resistance (R_s), the charge transfer resistance (R_{ct}), the double layer capacitance (C_{dl}) and the Warburg impedance (Z_w). The quantification of these parameters can be done by fitting data using the Randles circuit. This can be done using software such as zview. The electrolyte solution resistance emerges as a result of the conductance of the ions in the bulk solution. The use of the three electrode system is supposed to make the solution resistance between the counter and reference electrodes negligible but consideration has to be made for the solution resistance between the reference electrode and the working electrode. The electrolyte solution resistance is influenced by the concentration of the ions, type of ions and geometry of the area that carries the current as well as the temperature. This is seen in the equation that defines solution resistance shown below:

$$R_s = \rho \frac{l}{A} \quad 2.3$$

Where R_s is the solution resistance, ρ is the solution resistivity, A is the area and l is the length carrying the uniform current.

The solution resistance is found upon fitting of the data. The double layer capacitance is present at the interface of the working electrode, which is between the working electrode and the surrounding electrolyte solution. This is as a result of the ions from the electrolytic solution adhering on the electrode surface. The double layer capacitance is affected by the concentration of ions, type of ions, temperature, electrode roughness, impurity adsorption, oxide layers. In EIS the double layer capacitance behaviour varies from the ideal capacitor instead it behaves like a constant phase element (CPE). This is the reason in most models the CPE is used to denote the double layer capacitance. The variation from the ideal case is because of factors such as the surface roughness, non-uniform current distribution. The relationship between impedance and capacitance is expressed in equation 2.4 below.

$$Z = \frac{1}{C} (j\omega)^{-\alpha} \quad 2.4$$

Where Z is the impedance, C is the capacitance, j is an imaginary number, ω is the radial frequency, α is an exponent that has a value of one for an ideal capacitor. This latter is not true for systems that contain a CPE; the value of α is less than one in that instance.

Another component that is important in EIS is the charge transfer resistance. As the name implies this is the monitoring of the ease of the transfer of charge between the electrolyte solution and the surface (electrode). When the overpotential is very small in a system in equilibrium the charge transfer resistance can be expressed as follows,

$$R_{ct} = \frac{RT}{nFi_0} \quad 2.5$$

where R_{ct} is the charge transfer resistance, R is the gas constant, T is the temperature in Kelvin, n is the number of electrons, F is the Faradays constant and i_0 is the exchange current density.

Diffusion has been shown to lead to an impedimetric response that is termed the Warburg impedance. This is shown to occur at low frequencies in the Nyquist plot. This is because at high frequencies the distance travelled by diffusing species is very small while at low frequencies the opposite is true. Hence the Warburg impedance observed at low frequencies. The equation that is a representation of infinite Warburg impedance is as follows:

$$Z_w = \sigma \sqrt{\omega} (1 - j) \quad 2.6$$

Where Z_w is the Warburg impedance, σ is the Warburg coefficient, ω is the radial frequency. The Warburg coefficient can be expressed in the form of an equation as follows,

$$\sigma = \frac{RT}{n^2 F^2 A \sqrt{2}} \left(\frac{1}{C^o \sqrt{D_o}} + \frac{1}{C^R \sqrt{D_R}} \right) \quad 2.7$$

where σ is the Warburg coefficient, R is the gas constant, T is the temperature in Kelvin, n is the number of electrons, F is the Faradays constant, A is the area, C^o is the concentration of the oxidant, D_o is the diffusion coefficient of the oxidant, C^R is the concentration of the reductant, D_R is the diffusion coefficient of the reductant.

The relationship between impedance and frequency is not clearly defined when using Nyquist plots. Thus the use of Bode plots. The Bode plot is a plot of the log of the modulus of impedance versus the frequency, with the phase angle being also plotted against the log of frequency. The diagram in **Figure 2.15** shows that the phase angle

tends towards zero at low frequencies and high frequencies. The leaning of the phase angle towards zero at low frequencies is because of the current and voltage being in phase to each other. The observation of the same phenomenon at high frequencies is due to the influence of the electrolyte solution resistance. This effect can be expressed in the form of an equation shown below.

$$\phi = \tan^{-1} \frac{1}{1 + 2 \left(\frac{R_s}{R_{ct}} \right)} \quad 2.8$$

Where ϕ is the phase angle, R_s is the electrolyte solution resistance and R_{ct} is the charge transfer resistance.

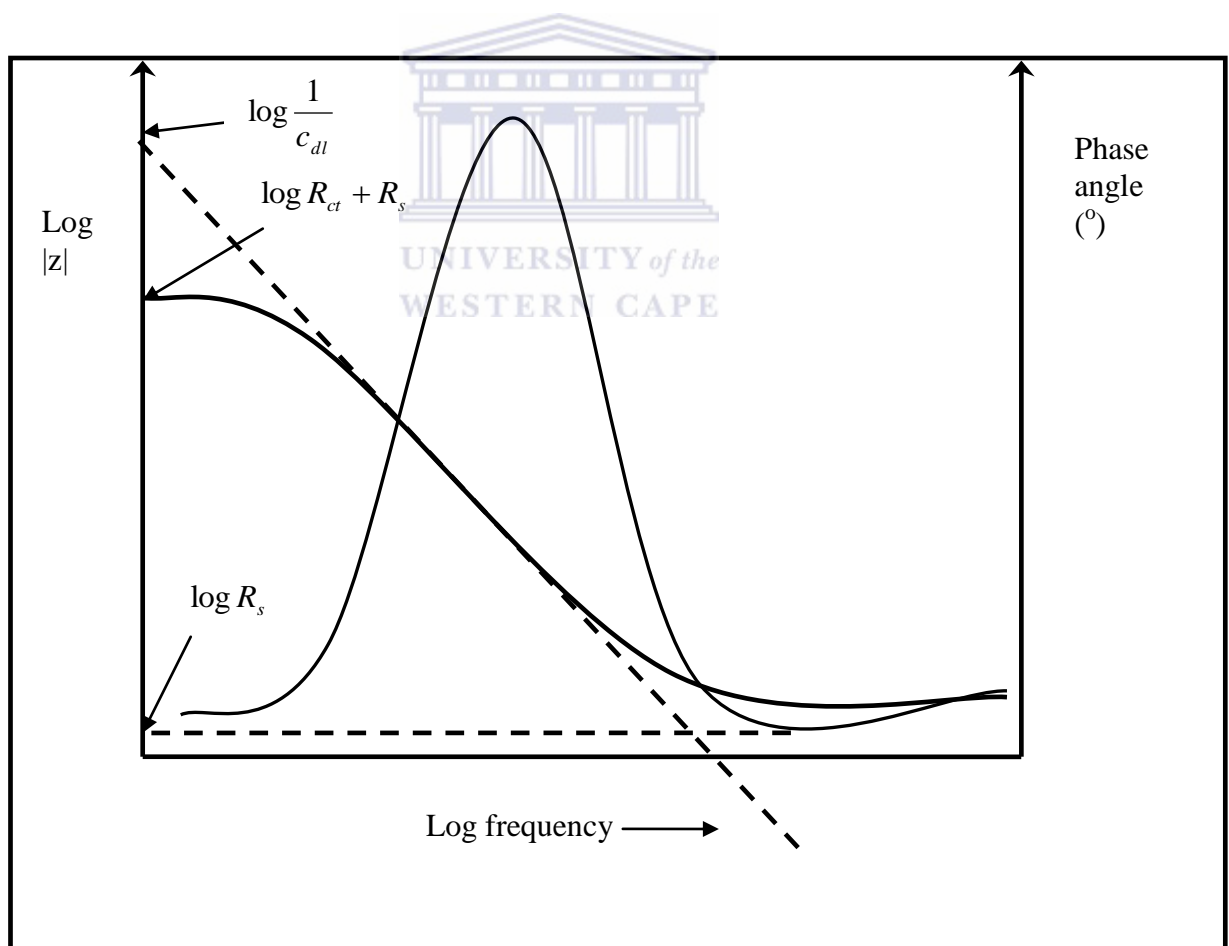


Figure 2.15: Bode plot for a simple electrochemical system

CHAPTER 3 :EXPERIMENTAL

The synthetic procedures used for the synthesis of the polymers and nanoparticles are reported. Characterisation techniques such as fourier transform infrared spectroscopy, ultraviolet-visible spectroscopy, fluorescence spectroscopy, electrochemical techniques, morphological techniques (AFM and SEM) are used in order to analyse the nature of the materials. The steps taken in the construction of the photovoltaic cells are reported.

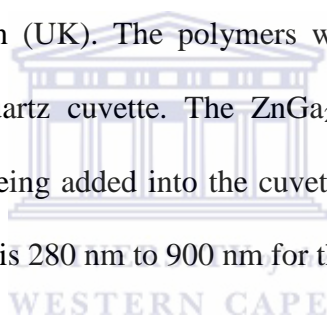


3.1 MATERIALS

Hydrochloric acid (HCl), anthracene, phenanthrene, aniline, ortho-methyl aniline (OMA), dimethyl sulfoxide (DMSO), hydrochloric acid (HCl), fuming sulphuric acid (H₂SO₄), zinc nitrate (ZnNO₃), gallium (Ga), perchloric acid (HClO₄), methanol, dimethyl ether, ammonium persulfate (APS), [6,6]-phenyl-C₆₁-butyric acid methyl ester (PCBM) was supplied by sigma Aldrich.

3.2 ANALYTICAL TECHNIQUES

The UV-visible spectra were recorded on a Nicolet Evolution 100 Spectrometer from Thermo Electron Corporation (UK). The polymers were dissolved in DMSO and decanted into a 1X1 cm quartz cuvette. The ZnGa₂O₄ was able to be partially dissolved in ethanol before being added into the cuvette. The UV-visible absorption spectrum range that was used is 280 nm to 900 nm for the polymers.



Attenuated total reflectance-fourier transform infrared (ATR-FTIR) spectroscopy was utilised to observe the vibrational transitions within the doped conjugated polymers. ATR-FTIR spectroscopy was done by loading the sample unto the sample holder without prior sample preparation.

The fluorescence measurements were obtained by the using of the Horiba Jobin Yvon NanoLog from France. The measurements were done both in solution and as a film on a glass substrate.

The X-ray analysis was done using Bruker multi purpose (powder) diffractometer.

The X-ray source that was used was Cu K α utilising a 2 θ range of 5-60°

The thermal gravimetric analysis was done using a Perkin-Elmer thermal gravimetric analyser. The samples were all analysed using a heat rate of 20 °C/min starting from 50 °C. The range that was analysed was from 50 °C to 600 °C for all the polymers.

All electrochemical experiments were carried out in a conventional three-electrode electrochemical cell by means of BAS100 electrochemical analyzer from BioAnalytical Systems (BAS) Technical (Stockport, UK). The working electrode was a platinum disk encapsulated in epoxy resin (electrode geometric area: 0.0177 cm²), a platinum wire and a Ag|AgCl electrode were used as counter electrode and reference electrode, respectively. Electrochemical impedance spectroscopy (EIS) measurements were recorded with VoltaLab PGZ 402 from Radiometer Analytical (Lyon, France).

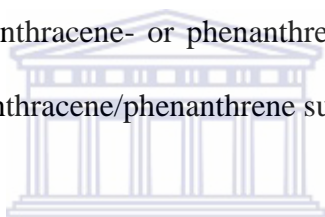
There are two techniques that were utilised to probe the morphology of the compounds, scanning electrochemical microscopy (SEM) and high resolution transmission electron microscopy (HR-TEM). SEM studies were done on polymers that were first spin coated on a glass substrate using a Zeiss Auriga, high resolution (FEG-SEM) field emission gun scanning electron microscope. HR-TEM studies were performed on samples of polymers and nanoparticles mounted on a copper coated TEM grid using a Tecnai G2F20X-Twin MAT 200 kV Field Emission Transmission Electron Microscope from FEI Eindhoven (Netherlands).

A KW 4A spin coater and 4 KW-AH hotplate was used from Chemat Technology Incorporated (California, USA) in the construction of the photovoltaic cell device.

3.3 SYNTHESIS

3.3.1 Synthesis of Anthracene sulfonic acid and Phenanthrene sulfonic acid

10 mL of fuming H_2SO_4 was added to 10 mL H_2SO_4 (6 M) and the mixture was diluted to 100 mL in a volumetric flask. 50 mL of the above solution was added to a round bottom flask that contained 2 g of anthracene or phenanthrene. The contents were heated to boiling in an oil bath (temperature between 120 – 140 °C) fitted with a condenser and thermometer. The mixture was refluxed for 2-3 h with constant shaking to immerse reactants into solution. The mixture was poured into a beaker with crushed ice. After 20 min the unreacted anthracene/phenanthrene was filtered off. 10 mL of a 50% NaOH solution was added to the mixture and put in a refrigerator to crystallize, to form a white anthracene- or phenanthrene sulfonic salt. The salt was then hydrolysed to form the anthracene/phenanthrene sulfonic acid.



3.3.2 Synthesis of polyaniline

Aniline (0.2592 mL, 0.142 M) was added into 20 mL of deionised water in a round bottomed flask. The vigorously stirred mixture was heated for 30 min at 50 °C on an oil bath that is temperature controlled. An aqueous solution of ammonium persulfate (APS) (0.1 M) was added dropwise to the hot solution. The mixture was cooled down to room temperature. Then it was left stirring for con 24 h. The product was filtered and washed with deionised water, methanol and dimethyl ether, respectively, to remove impurities such as APS and unreacted aniline. The latter was repeated three times.

3.3.3 Synthesis of Polyaniline/Phenanthrene sulfonic acid

Aniline (0.2592 mL, 0.142 M) was added into 20 mL of deionised water, whereby phenanthrene sulfonic acid (0.2592 mg) was added. The vigorously stirred mixture was heated for 30 min at 50 °C on an oil bath that is temperature controlled. An aqueous solution of ammonium persulfate (APS) (0.1 M) was added dropwise to the hot solution. The mixture was cooled down to room temperature while continuously stirred for 24 h. The product was filtered and washed with deionised water, methanol and dimethyl ether, respectively, to remove impurities such as APS, free PSA and unreacted aniline. The latter was repeated three times.

3.3.4 Synthesis of poly(*ortho*-methoxyaniline)/Anthracene sulfonic acid nanostructures and poly(*ortho*-methoxyaniline)/Phenanthrene sulfonic acid

Poly(*ortho*-methoxyaniline)/Anthracene-/Phenanthrene sulfonic acid were prepared by adopting a similar procedure as in section 3.3.2. In a 100 mL round bottomed flask, 0.26 mL of *ortho*-methoxyaniline was added to 20 mL of deionised water. This was followed by the addition of 0.2592 mg of anthracene sulphonic acid. The vigorously stirred mixture was heated for 30 min at 50 °C on an oil bath that is temperature controlled. An aqueous solution of ammonium persulfate (APS) (0.1 M) was added dropwise to the hot solution. The mixture was cooled down to room temperature while continuously stirred for 24 h. The product was filtered and washed with deionised water, methanol and dimethyl ether 3 times, respectively, to remove impurities such as APS, free ASA and unreacted *ortho*-methoxyaniline. The same procedure was used for the synthesis of poly (*ortho*-methoxyaniline)/Phenanthrene was utilised.

3.3.6 Synthesis of the Gallium Perchlorate

7 g of gallium metal was weighed into a round bottomed flask and 5 mL of concentrated HClO₄ added. The mixture was refluxed under constant stirring for 6 h at 120 °C, after which, a white precipitate of Ga(ClO₄)₃.6H₂O was formed.

3.3.7 Synthesis of the ZnGa₂O₄ nanoparticles

Synthesis of the nanoalloy was done by utilising a coreduction method of Zn(NO₃)₂ and Ga(ClO₄)₃.6H₂O with sodium borohydride in a 1:1 molar ratio of the salts. The precipitate was filters off and washed with water.

3.4 MEASUREMENT OF PHOTOPHYSICAL PROPERTIES

3.4.1 Fluorescence quantum yields

Fluorescence quantum yield is defined as the ratio of the photons emitted to the number of photons absorbed. As a result it gives the probability of the excited state being deactivated via fluorescence

The comparative method was used to determine the fluorescence quantum yields (Φ_F) of the polymers using equation 3.1

$$\Phi_F = \Phi_{F(\text{Std})} \frac{F \cdot A_{\text{Std}} \cdot \eta^2}{F_{\text{Std}} \cdot A \cdot \eta_{\text{Std}}^2} \quad 3.1$$

where F and F_{std} are the areas under the fluorescence curves of the polymers and the standard, respectively. A and A_{std} are the respective absorbances of the sample and the standard at the excitation wavelength and η and η_{std} are the refractive indices of

the solvents used for the sample and standard, respectively. Anthracene was used as a standard in ethanol where $\Phi_F = 0.27$.

3.5 ELECTROCHEMICAL CHARACTERISATION

3.5.1 Preparation of the surface modified electrode

A platinum disk electrode was thoroughly cleaned by polishing it on a soft polishing pad using 1.00 μM , 0.30 μM and 0.05 μM slurries of alumina, respectively, rinsing with de-ionized water after each polish. This was followed by ultrasonication in de-ionized water for 5 min. All the electrochemical data was run in a paste of the polymer that was made by taking 0.05 g of polymer and 500 mL of 0.1 M HCl. Cyclic voltammetry measurements were done at different scan rates.

3.5.2 Electrochemical Impedance measurements

The electrochemical impedance measurements were conducted on the polymer pastes. The impedimetric spectra were recorded with a VoltaLab PGZ 402 at a frequency range of 100 kHz to 10 mHz, amplitude of 10 mV and a potential of 150 mV.

3.6 TECHNIQUES USED IN CONSTRUCTION OF THE PHOTOVOLTAIC CELL

3.6.1 Spin Coating

Spin coating is one of the techniques that is predominantly used in the field of research where a thin film of uniform thickness is formed on a substrate. This technique is predominantly used in electronics. Spin coating involves several stages, that is deposition of fluid, spin up, spin off and solvent evaporation, as shown in **Figure 3.1**. The deposition of the fluid stage involves the addition of the fluid by

using a pipette or a micro syringe at the centre of the substrate and the primary speed is the one that is used to spread the fluid from the centre outward. This is done to form a uniform spread over the surface of the substrate. This is followed by the spin up phase, which happens when the secondary speed, which is higher than the primary speed, is used to make a thin layer on the substrate. Thus this stage is said to influence the thickness of the film that is formed on the substrate. Spin off and evaporation stage can occur concurrently. This is when the substrate is spinning at a constant rate and formation of the film is predominantly influenced by the evaporation of the solvent.

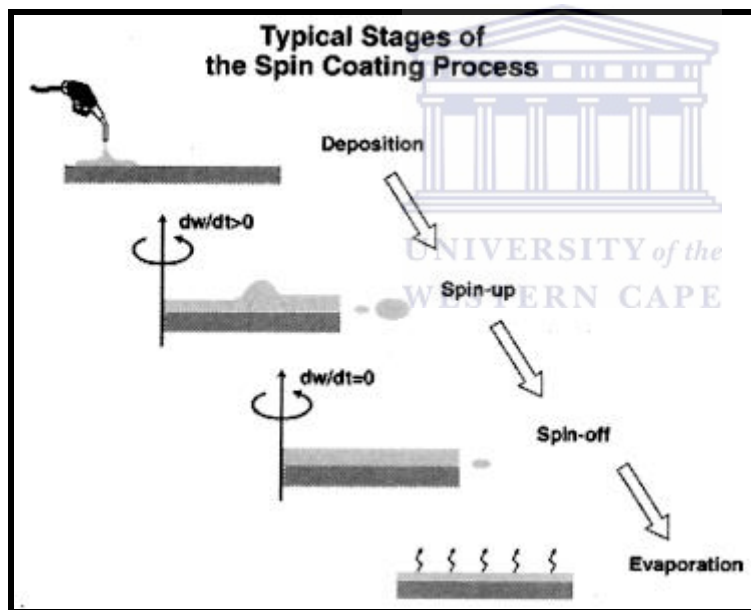


Figure 3.1: Schematic representation of the spin coating process

3.6.2 Sputter coating

The sputter coater makes use of different targets which can be gold, palladium, silver. The target is bombarded with heavy gas atoms (argon), this leads to the ejection of the metal from the target to cross the plasma to the substrate that is close to the target plate, **Figure 3.2**. This occurs at low pressure. The deposition of the metal on the

surface using this method is in the form of islands. Even though the deposition is in the form of islands the thickness of the deposited materials is able to be controlled by varying parameters such as the current at which the sputter coating is done.

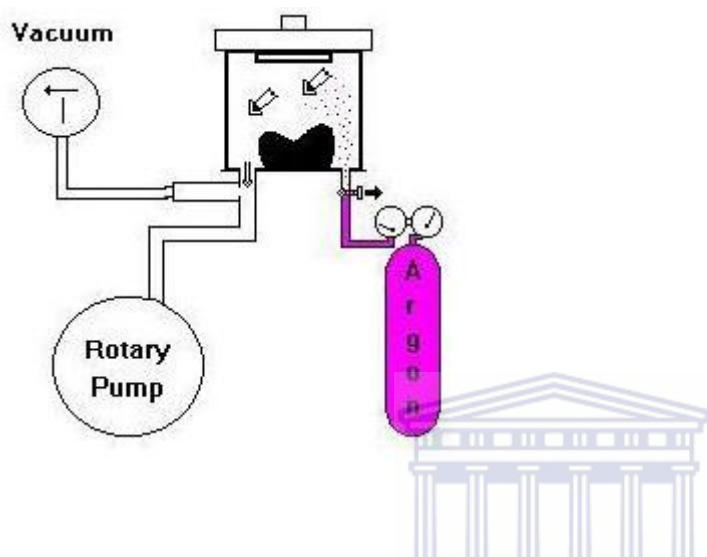


Figure 3.2: Schematic representation of the sputter coater

3.7 CONSTRUCTION OF THE PHOTOVOLTAIC CELL

The photovoltaic cell was constructed using an indium tin oxide coated glass. The 1.5 cm X 1.5 cm glass substrate was cleaned in three different solvent, acetone, ethanol, and isopropanol, respectively in an ultrasonication bath for 5 min in each solvent. A thin layer of poly(3,4-ethylenedioxythiophene)-poly(styrenesulfonate) (PEDOT-PSS) solution was spin-coated on conductive side of the glass. The parameters that were for the primary stage were 500 rpm for nine seconds and for the secondary stage it was 1500 rpm for 40 s. The PEDOT-PSS layer was subsequently annealed at 50 °C for 15 min on a hotplate. The active layer containing the blended polymer and PCBM was dissolved in 1 mL of DMSO and spin-coated on top of the PEDOT-PSS layer. The parameters that were used are 500 rpm for nine s for the primary stage and 1000 rpm

for 18 s for the secondary stage. A plain glass with the same dimensions as the ITO coated glass was then taken and cellotape plastered on three sides of the glass to expose an area of $\sim 1 \text{ cm}^2$. Silver was then sputtered on the glass using a sputter coater to form a layer with a thickness of 150 nm on the glass substrate. The cellotape was removed from both glasses and a thin coating of silicone glue was placed at these edges. The two glass substrates (one with the active polymer PCBM blend and the other with the silver) were adhered together making sure the edge of each is exposed. These were pressed together for 4 h using clips before measurements.

The current-voltage (I-V) measurements on the solar cell devices were performed using a Keithly semiconductor characterization system (SCS) by connecting the positive terminal to the anode (ITO) and a negative terminal to the cathode (silver).

3.8 ANALYSIS OF THE PERFORMANCE OF THE PHOTOVOLTAIC DEVICE

When light shines on a solar cell, the current that is measured is called the photocurrent. The value of the photocurrent is dependent on many factors in addition to just the quality of the device. The quality of the device, the incident wavelength, intensity of the incident light and the area of the device being illuminated are some of factors that affect the photocurrent. A graph of current (I) versus voltage (V) in Figure 3.1 is a common way to illustrate the properties of solar cells [111]. In the dark, the I-V curve passes through the origin, with no potential, no current flows, Figure 3.1(a). Illumination of the device leads to the shift of the curve in such a way that it moves away from the origin as illustrated in **Figure 3.3(b)**.

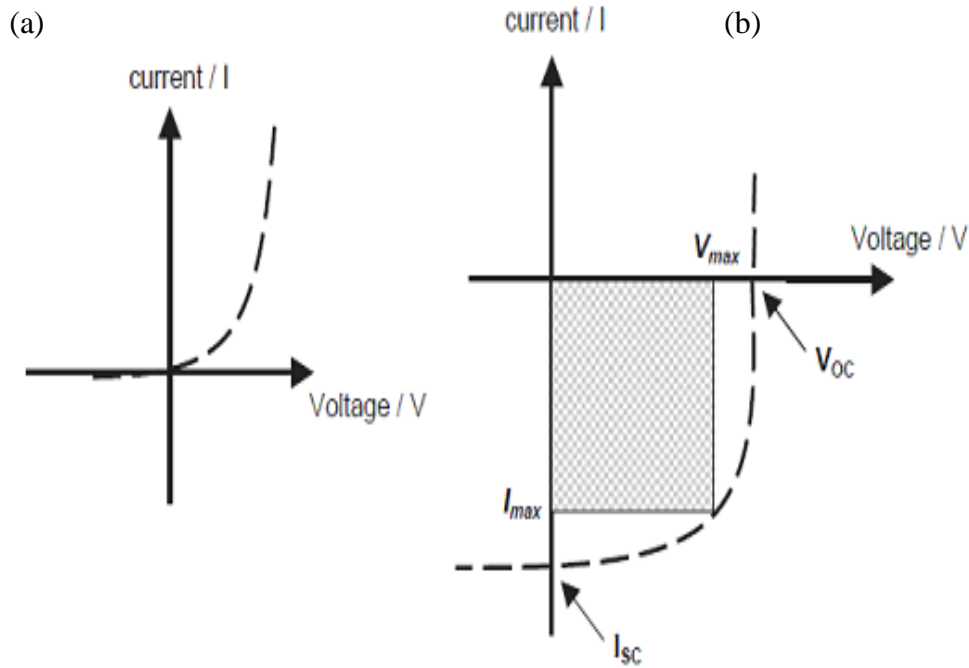
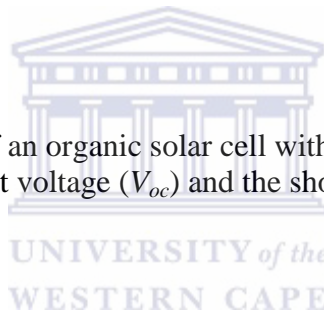


Figure 3.3: The I-V curves of an organic solar cell without light (a) and illuminated with light (b). The open circuit voltage (V_{oc}) and the short-circuit current (I_{sc}) are shown.



The I-V curve contains a number of important parameters that are related to photovoltaic cells, these include open circuit voltage (V_{oc}), short circuit current (I_{sc}), maximum current and voltage. The latter factors make it possible to calculate parameters such as the fill factor (FF), maximum power (P_{max}). P_{max} is important in the determination of the efficiency of the solar cell.

3.8.1 Open Circuit Voltage (V_{oc})

Open circuit voltage is defined as the maximum voltage that can be obtained when measuring between two leads when the device is disconnected. The value for the open circuit voltage is taken from the I-V curve at the point where the current is \sim zero. The V_{oc} is a factor that influences the devices efficiency. The origin of the influence of the

V_{oc} on the organic solar cells has not been clearly defined, but what has been clearly seen is that it is greatly influenced by the morphology of the organic layer.

3.8.2 Short Circuit Current (I_{sc})

The short circuit current gives the maximum current density that can be obtained when the two leads are connected to each other. When analysing an I-V curve, the short circuit current is the value where the voltage is \sim zero.

3.8.3 Fill Factor (FF)

The fill factor is defined as the ratio of the curve under the maximum power point of the cell ($P_{max} = I_{max} V_{max}$) to the area associated with open and closed circuit ($P = I_{sc} V_{oc}$). The fill factor is referred to as a quantifying unit for the squareness of the I-V curve. This is also influenced by the materials morphology. In addition to this it is also influenced by the stability of the materials.

The fill factor can be calculated using the following equation:

$$FF = \frac{V_{max} \cdot I_{max}}{V_{oc} \cdot I_{sc}}$$

Where V_{max} and I_{max} are the current and voltage at the point of maximum power output of the solar cell. I_{max} and V_{max} can be determined by calculating the power output P of the solar cell ($P=I \cdot V$) at each point between I_{sc} and V_{oc} and finding the maximum of P_{max} . The theoretical limit of a fill Factor (FF) is between 0.25 and 1.

3.8.4 Power Conversion Efficiency (η)

Power Conversion efficiency can be defined as the ratio between the maximum power output (P_{max}) and the power that is from the incident light (P_{in}). As already stated the

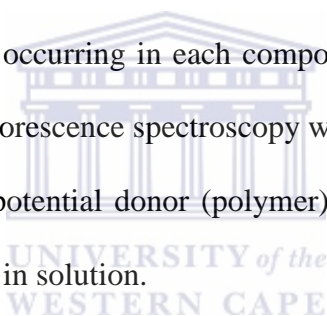
power conversion efficiency is greatly influenced by the V_{oc} and I_{sc} . The latter is displayed in the following equation used to calculate the efficiency.

$$\eta = \frac{FF \cdot V_{oc} \cdot I_{sc}}{P_{in}}$$



CHAPTER 4 : CHARACTERISATION OF THE MATERIALS

Analysis of the data that is found using FTIR, UV-visible spectroscopy, fluorescence spectroscopy, SEM and AFM is provided. The vibrational spectroscopy technique such as FTIR spectroscopy helps in deducing that there has been successful synthesis of the polymers. This is because it is able to show bonds that are broken and also bonds that are formed. The UV-visible spectroscopy helped in determining the electronic transitions that are occurring in each compound and also the energy band gap of each transition. The fluorescence spectroscopy was used to see whether there is energy transfer between the potential donor (polymer) and acceptor (nanoparticles). The latter is analysed for both in solution.



4.1 VIBRATIONAL SPECTROSCOPY OF THE POLYMERS

4.1.1. FTIR of the Conjugated Polymers

Figure 4.1 depicts the FTIR spectrum of the synthesised conjugated polymers. In **Figure 4.1(a)**, it is shown that PANi has strong stretching vibrations that are observed at 1637 cm^{-1} , 1549 cm^{-1} , 1373 cm^{-1} and 1198 cm^{-1} . The band at 1637 cm^{-1} is assigned to the quinoid moiety of the polymer chain, at 1549 cm^{-1} to the benzenoid moiety of the polymer and the stretching vibration at 1373 cm^{-1} is due to the CN stretching vibration. The relative intensities between these two vibrational bands is able to give the intrinsic oxidation state of the polymer [112]. The stretching vibration due to the quinoid moiety is more intense than the one that is due to the benzenoid moiety. This implies that the polymer synthesised is predominantly in its oxidised form, pernigraniline. This is further supported by the fact that the wavenumber at which the transition occurs for the CN stretching is for a tertiary amine. The latter can lead to the conclusion that the PANi synthesised is predominantly in its oxidised form, pernigraniline. The C-H stretching vibrations were observed at 1198 cm^{-1} . The PANi-PSA FTIR spectrum that is shown in **Figure 4.1(b)** shows transitions that are due to the quinoid and benzenoid ring at lower wavenumbers, 1579 cm^{-1} and 1491 cm^{-1} , respectively. There is an additional peak at 1089 cm^{-1} that is seen in PANi-PSA, this is attributed to the sulfone moiety (S=O) of the phenanthrene sulfonic acid.

Figure 4.1 (c) and **(d)** depicts the FTIR of POMA-PSA and POMA-ASA, respectively. Stretching vibrations were observed for the POMA-PSA at 1579 cm^{-1} , 1491 cm^{-1} , 1291 cm^{-1} , 1161 cm^{-1} , 1084 cm^{-1} and 762 cm^{-1} . The first two stretching vibrations are the quinoid and benzenoid moiety, respectively. The intensity of the vibrational stretch that is due to the benzenoid is much greater in comparison with the

quinoid. This shows that the formed polymer is in its emeraldine form. As mentioned in Chapter 2, the benzenoid moiety is expected to occur at a higher percentage in emeraldine than the quinoid moiety. The transition at 1291 cm^{-1} is because of the CN stretching vibration of a secondary amine. The peak at 1084 cm^{-1} is due to the sulfone from the dopant, phenanthrene sulfonic acid. The peak at 761 cm^{-1} is as a result of the substitution at the *ortho* position of the aromatic ring, since POMA-PSA has a methoxy substituent at that position. The transitions observed for POMA-ASA are the same as the ones for POMA-PSA with slight shifts. The transitions for the quinoid moiety are observed at 1579 cm^{-1} . Other bands are at 1487 cm^{-1} , 1294 cm^{-1} , 1161 cm^{-1} and 773 cm^{-1} . They can be attributed to the benzenoid moiety, CN stretching, CH stretching and S=O stretching vibration, respectively.

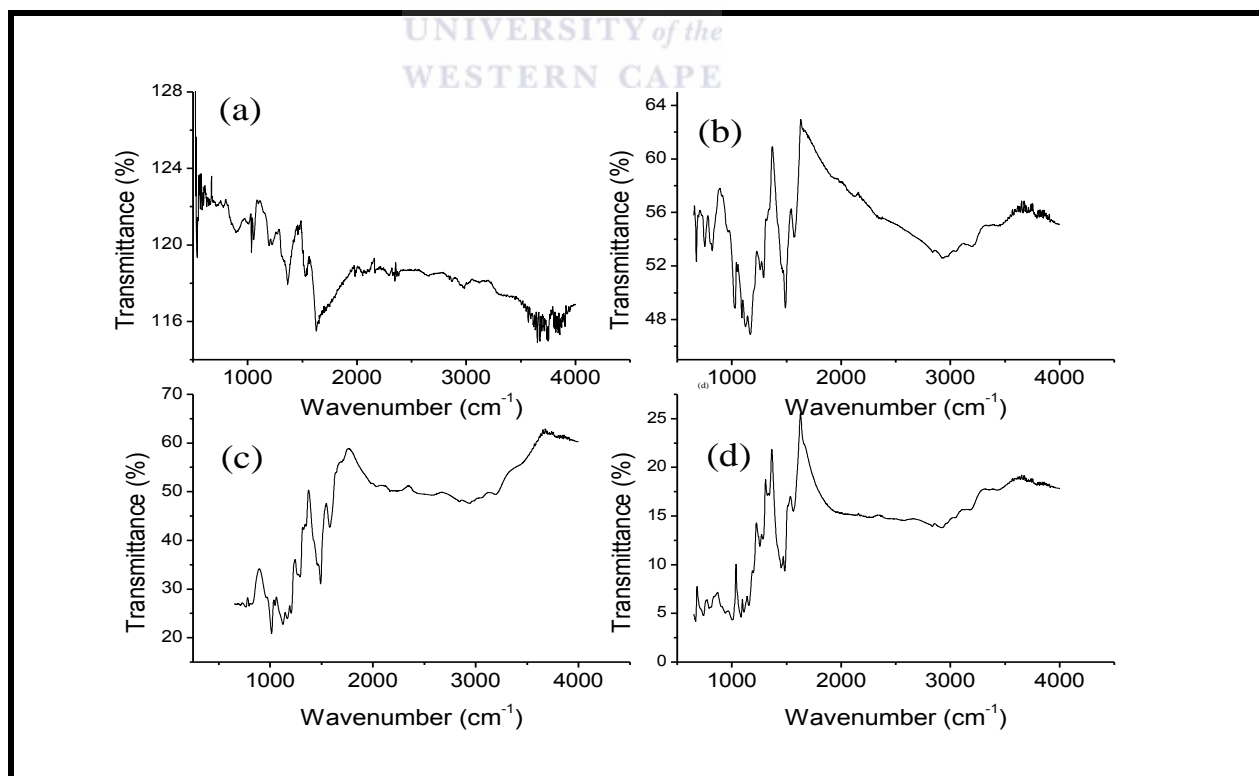


Figure 4.1: ATR-FTIR spectrum of a) PANi b) PANi-PSA, c) POMA-ASA, d) POMA-PSA

4.1.2 Raman Spectra of the Conjugated Polymers

A 532 nm laser beam was used to obtain the Raman spectra of all the conjugated polymers. The laser beam that was used makes it possible to observe vibrations that are due to both the benzenoid and quinoid moiety of the polyaniline and its derivatives [113]. The Raman spectrum of PANi and PANi-PSA is shown in **Figure 4.2**. The Raman spectrum of PANi has vibrational modes that are as a result of the benzenoid moiety at 1663 cm^{-1} and also ones that are due to the quinoid moiety at 1584 cm^{-1} . There is no apparent difference in the intensities of the peaks that are assigned to the benzenoid and the quinoid moiety. Hence no conclusions can be made in terms of the intrinsic oxidation state of the PANi as seen in the IR data above. The stretching vibrations due to C-N bond are observed at 1441 cm^{-1} . The PANi-PSA has the same vibrational modes as the one that is seen in PANi, there is vibration due to the benzenoid moiety at 1670 cm^{-1} and the one due to the quinoid moiety at 1584 cm^{-1} . Even the PANi-PSA is in its emeraldine form. The latter is also true for the POMA-PSA and POMA-ASA as seen in **Figure 4.3**. The vibrations that are as a result of the benzenoid moiety are at 1634 cm^{-1} and 1649 cm^{-1} for POMA-PSA and POMA-ASA, respectively. The vibrations that are due to the C-N bond are observed at 1458 cm^{-1} and 1451 cm^{-1} for POMA-PSA and POMA-ASA, respectively.

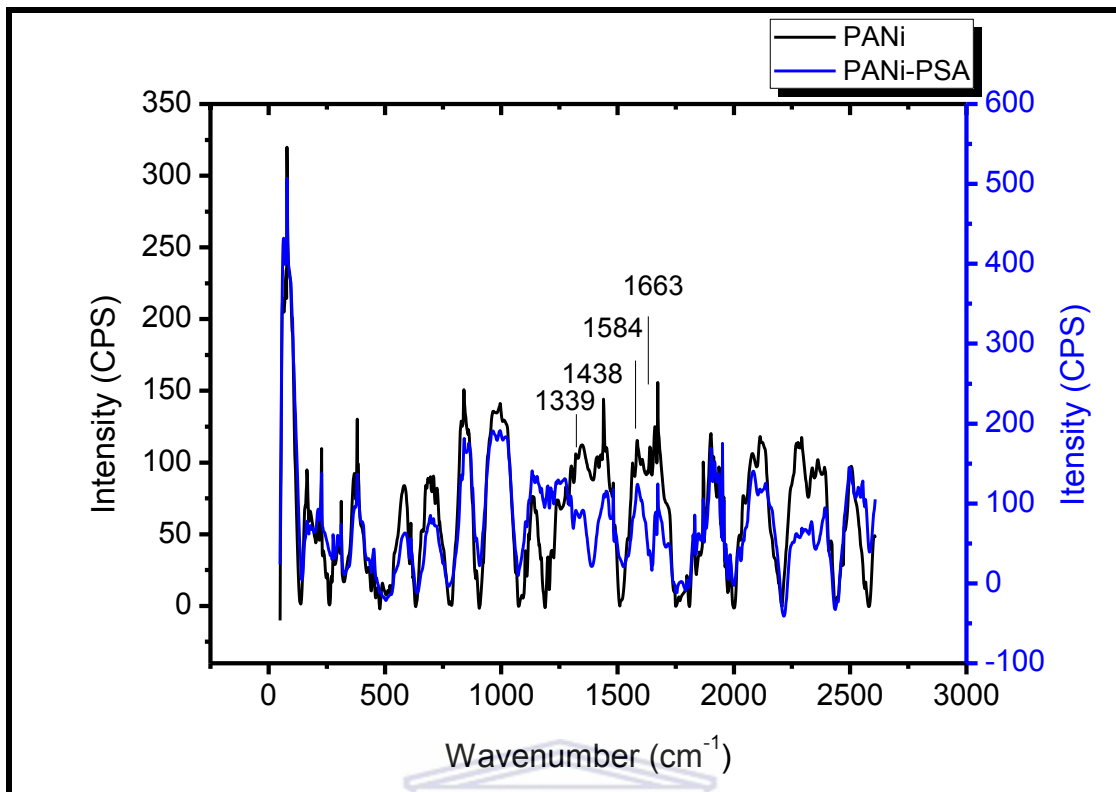


Figure 4.2: The Raman spectra of PANi and PANi-PSA using a 532 nm laser beam

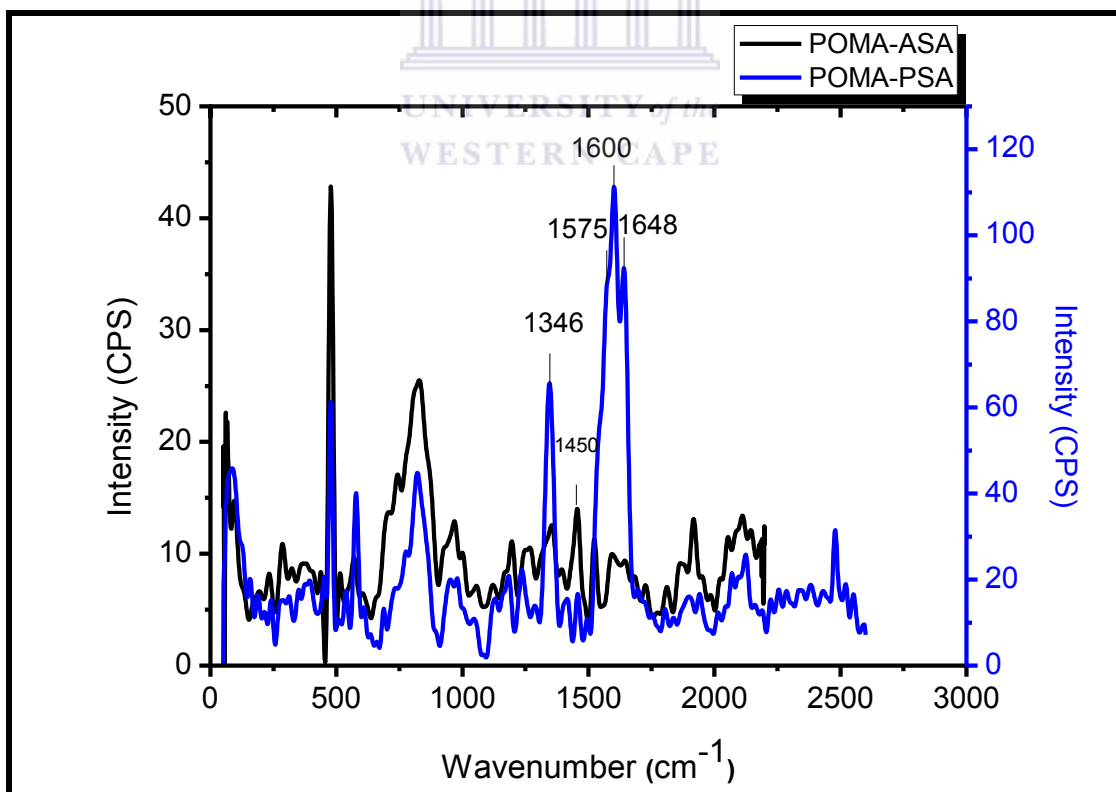


Figure 4.3: The Raman spectra of POMA-ASA and POMA-PSA using a 532 nm laser beam

4.2 PHOTOSPECTROSCOPIC CHARACTERISATION OF THE COMPOUNDS IN SOLUTION

4.2.1 Electronic Transitions in Conjugated Polymers

The UV-visible spectra of the polymers were done in DMSO. The generally observed wide absorption spectrum of the polymers is advantageous for photovoltaic cells, **Figure 4.4-4.7**. This is because with photovoltaic cells, compounds that absorb at a wide spectral range are required to absorb as much energy as it is possible from the sun.

The UV-visible spectrum depicted in **Figure 4.4** of the POMA-ASA showed five transitions at 287 nm, 320 nm, 440, 640 nm and 835 nm. As previously outlined in Chapter 2, the electronic transitions observed in conjugated compounds are mainly due to the movement of electrons from the π -bonding to the π -antibonding orbitals. The latter is true for polyanilines as well. Considering this, the assignation of the transitions is as follows, the transition at 320 nm is due to the movement of electrons from π -bonding to the π -antibonding orbital within the benzenoid moiety of the compound. When a polymer is doped other transitions arise within the normal π - π^* band gap, these transitions are due to the formation of the polaron energy carriers [86]. These are responsible for the electronic transitions observed at 420 nm and 640 nm. The transition at 835 nm is due to the formation of a bipolaron, which is of lower energy than the polaron.

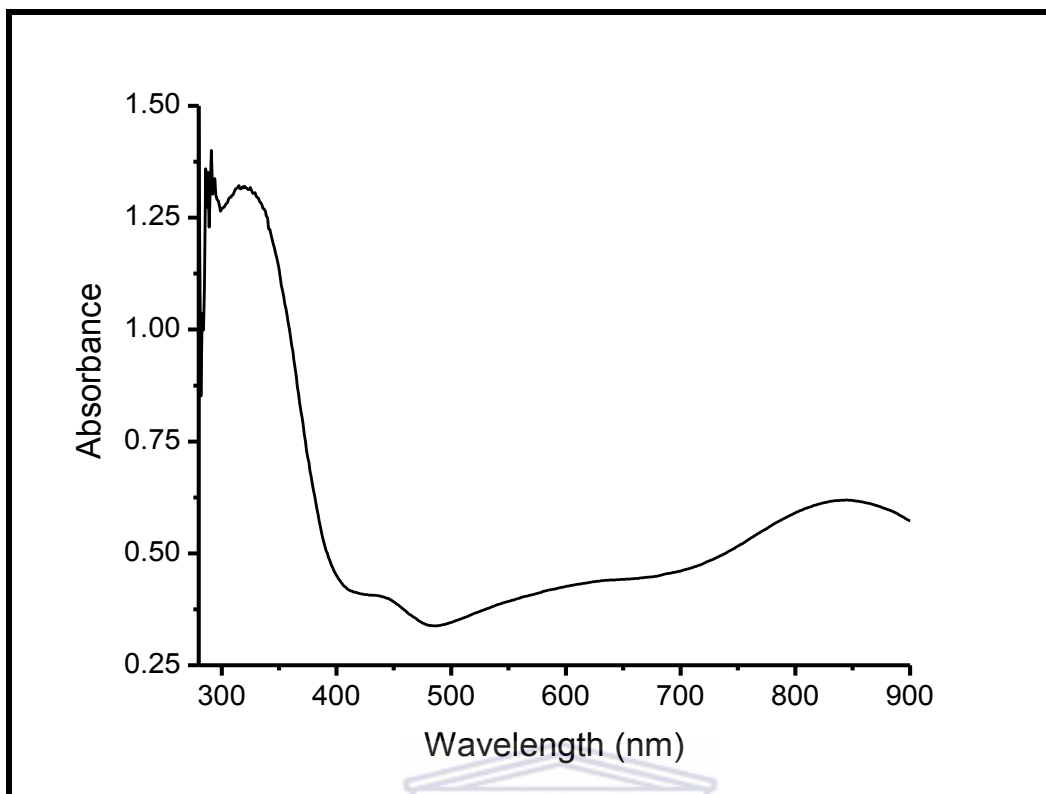


Figure 4.4: The electronic transition spectrum of POMA-ASA

In comparison with POMA-ASA, the number of transitions observed for POMA-PSA is much less, only three transitions shown in **Figure 4.5**, at 318 nm and one at ~450 nm and a very wide peak is observed at ~600 nm. The peak at 318 nm is still due to the π - π^* transitions. The one at ~450 nm is from the energy states of the polaron, which is formed upon doping, to the π -antibonding orbital of the benzenoid moiety. The wide peak is due to the quinoid moiety. Its wideness might be attributed to the existence of the polymer in a wide variety of chain lengths.

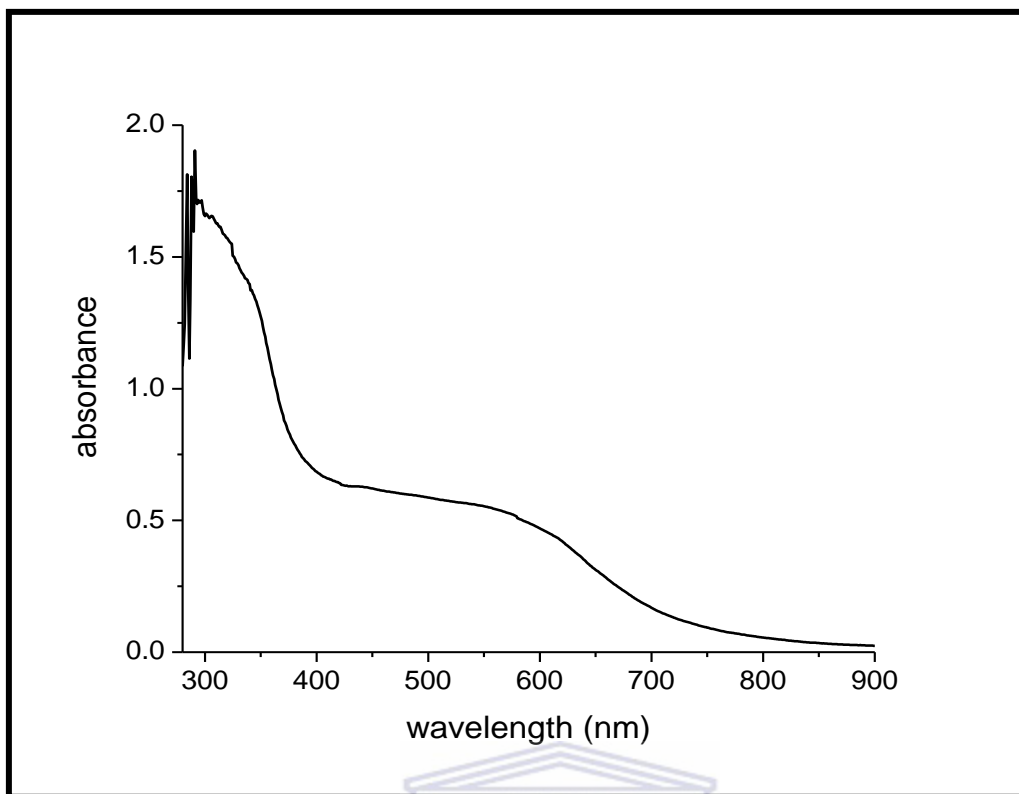


Figure 4.5: The electronic transition spectrum of POMA-PSA

When considering that a compound with a wide absorption is advantageous in photovoltaic cells, POMA-ASA would be the most attractive polymer in photovoltaic cell construction. When comparing the two polymers it is expected that the POMA-ASA will have a more efficient transportation of the holes since it has two types of charge carriers.

There are three clearly defined transitions that are observed for the PANi-PSA as denoted in **Figure 4.6**. These transitions occur at 330 nm, 435 nm and 600 nm.

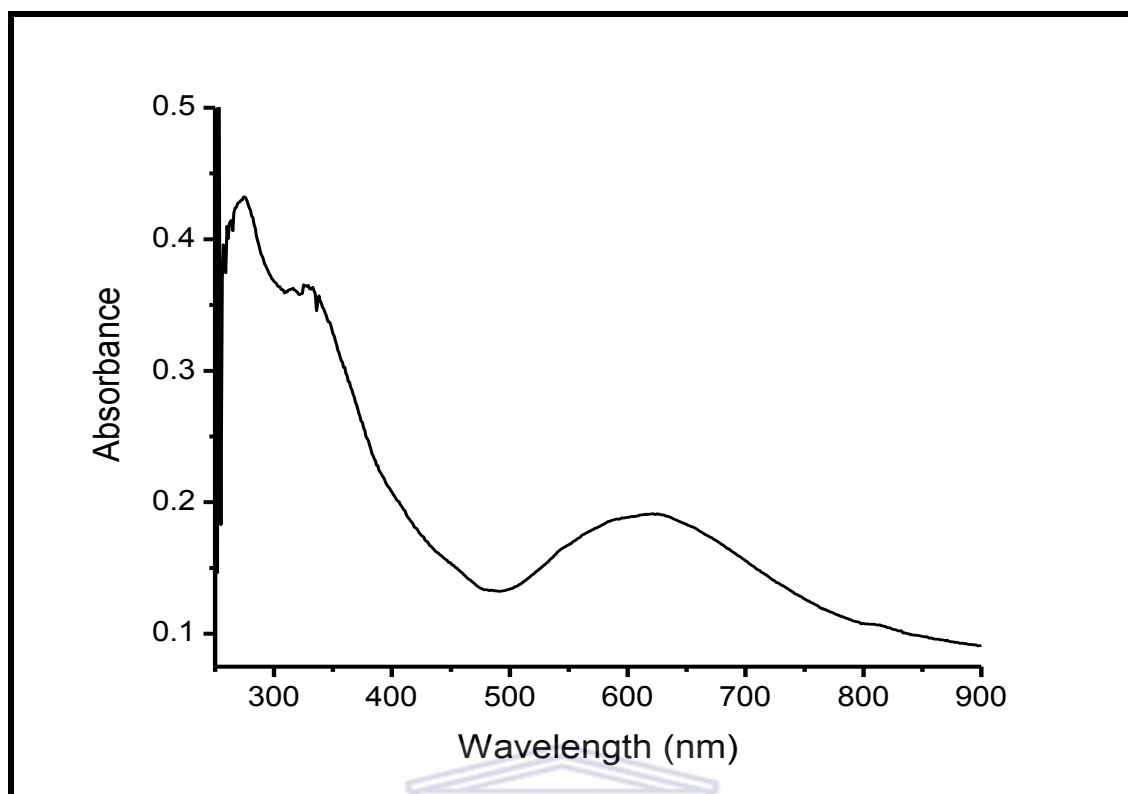


Figure 4.6: The electronic transition spectrum of PANi

The transition at 330 nm is attributed to the excitation of the polymer from the π -bonding orbital to the π -antibonding orbital of the benzenoid moiety. The transition at 435 nm occurs as a result of the formation of polarons upon doping. This transition is as a result of the movement of electrons from the lowest energy orbital of the polaron to the π -antibonding orbital. The transition that is observed at 600 nm is attributed to the transitions that involve the quinoid moiety. These are charge transfer transitions. The very broad peak can be attributed to the different chain lengths of the polymers.

PANi displays two electronic transitions as denoted in **Figure 4.7**. The transitions are observed at 330 nm and 600 nm. These transitions occur at the same wavelength as the previously discussed PANi-PSA and are as a result of the same reasons as stated above. The peak at 330 nm is as a result of the π -bonding to the π -antibonding orbital

of the benzenoid moiety. The transition at 600 nm is as a result of the charge transfer transitions from the quinoid structure to the benzenoid. As expected for PANi that has not been doped, there is no occurrence of the peaks that are due to the transitions involving polaron or bipolaron energy states.

When looking at the transition that is due to the π - π^* orbital, a trend is observed. The PANi and PANi-PSA have the transition at 330 nm which is a more bathochromic position in comparison with POMA-PSA and POMA-ASA, with the transitions being observed at 318 nm and 320 nm, respectively. This is as a result of the methoxy substituents on the polymer chain; it lowers the extent of π conjugation.

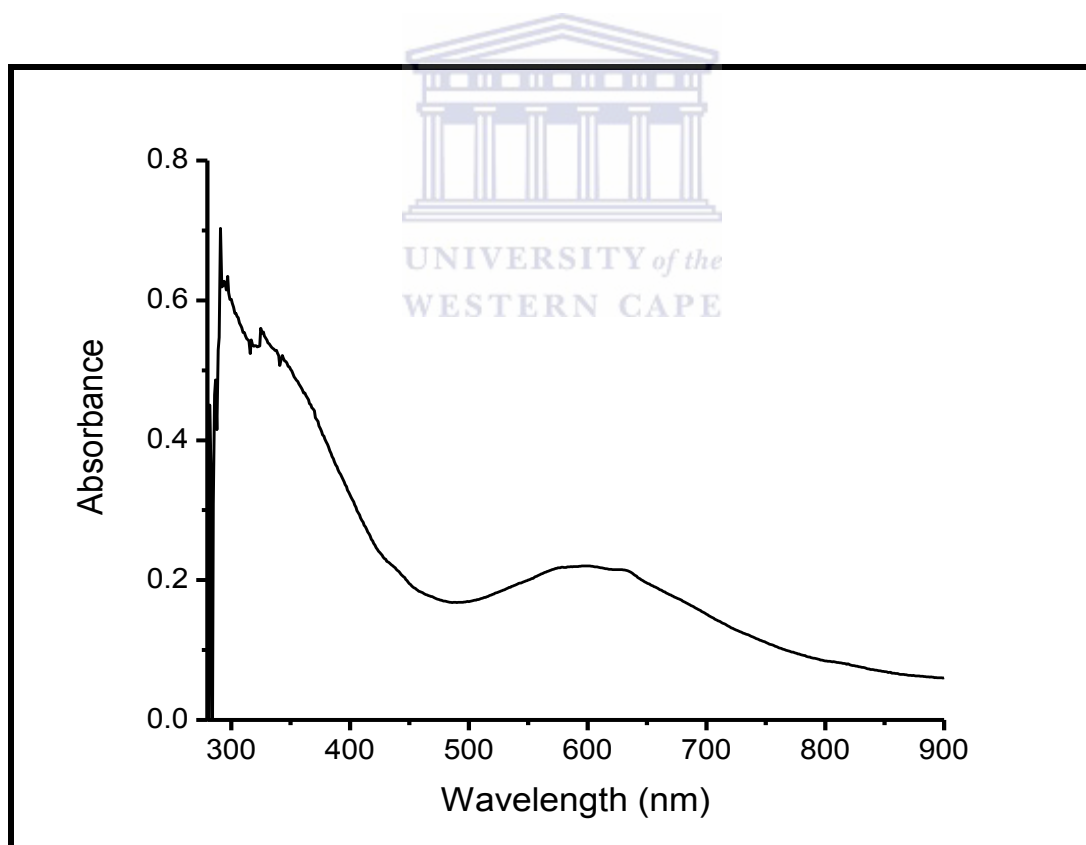


Figure 4.7: The electronic transition spectrum of PANi-PSA

The energy band gap was calculated and reported in Table 2. The calculated energy gap values showed that PANi had the smallest band gap of 2.4 eV with the POMA-

ASA displaying the largest value of 3.0 eV. The smallest energy band gap value that is observed with the PANi is as a result of the higher degree of conjugation in this compound in comparison with the ones that are doped with the sulfonic acid [83, 114]. The sulfonic acid shortens the degree of conjugation which leads to a higher energy gap which consequently implies that the conductivity of the polymers is also lowered. In the POMA compounds the degree of conjugation is relatively much lower compared to the PANi-PSA, as there are two factors that contribute in lowering the conjugation length; the sulfonic acid and the methoxy substituent on the aromatic ring.

Table 2: The energy band gaps of the conjugated polymers

Polymer	λ_1 (nm)	λ_2 (nm)	λ_3 (nm)	λ_4 (nm)	$E_{\text{band gap}}$ (eV)
PANi	330		600		2.48
PANi-PSA	330	430	600		2.55
POMA-ASA	320	440	640	835	2.71
POMA-PSA	318	450	600		3.0

4.2.2 Electronic transitions in ZnGa_2O_4 nanoparticles

The absorption spectrum of the nanoparticle showed a broad peak at the high energy area of the UV-visible spectrum, **Figure 4.8**. The maximum absorption of the peak is observed at 282 nm. The electronic transitions that are observed are as a result of the excitation of the electron from the valence band to the conduction band, forming the electron hole pair, the exciton. The band gap of the nanoparticles was calculated to be

4.2 eV. This is indicative of a compound with low conductivity and a very weak semiconductor material.

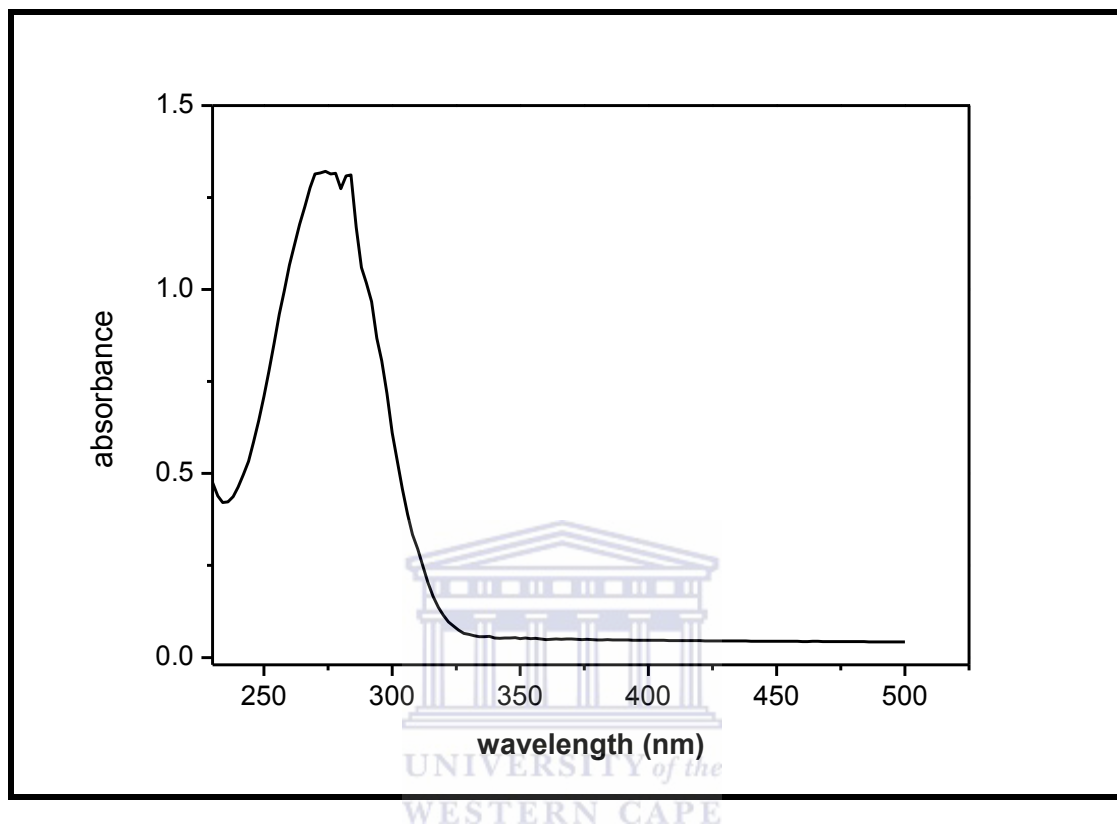


Figure 4.8: The electronic transition spectrum of ZnGa_2O_4 nanoparticles

4.2.3 Photoluminescence of the Conjugated Polymers

The photoluminescence of the compounds were studied in DMSO. As already illustrated in Chapter 2, photoluminescence or fluorescence is a transition that occurs when a compound in its excited state goes back to its ground state by releasing a photon. The singlet excited state of the polymers occurs as an exciton. This exciton is able to hop along the polymer chain until it dissipates by transitions such as fluorescence. The polymers were all excited at 320 nm and their spectra is depicted in **Figure 4.9**. The photoluminescence behaviour that is as a result of the exciton is observed at 391 nm and 393 nm for PANi and PANi-PSA, respectively. The transition

is observed at 385 nm for POMA-ASA and POMA-PSA. The observation of the transition at higher energy for the POMA-ASA and POMA-PSA in relation to PANi and PANi-PSA is as a result of the lower extent of conjugation that is expected for POMA derivatives. There is a Stokes shift of ~ 60 nm that is observed for all the polymers as shown in Table 3.

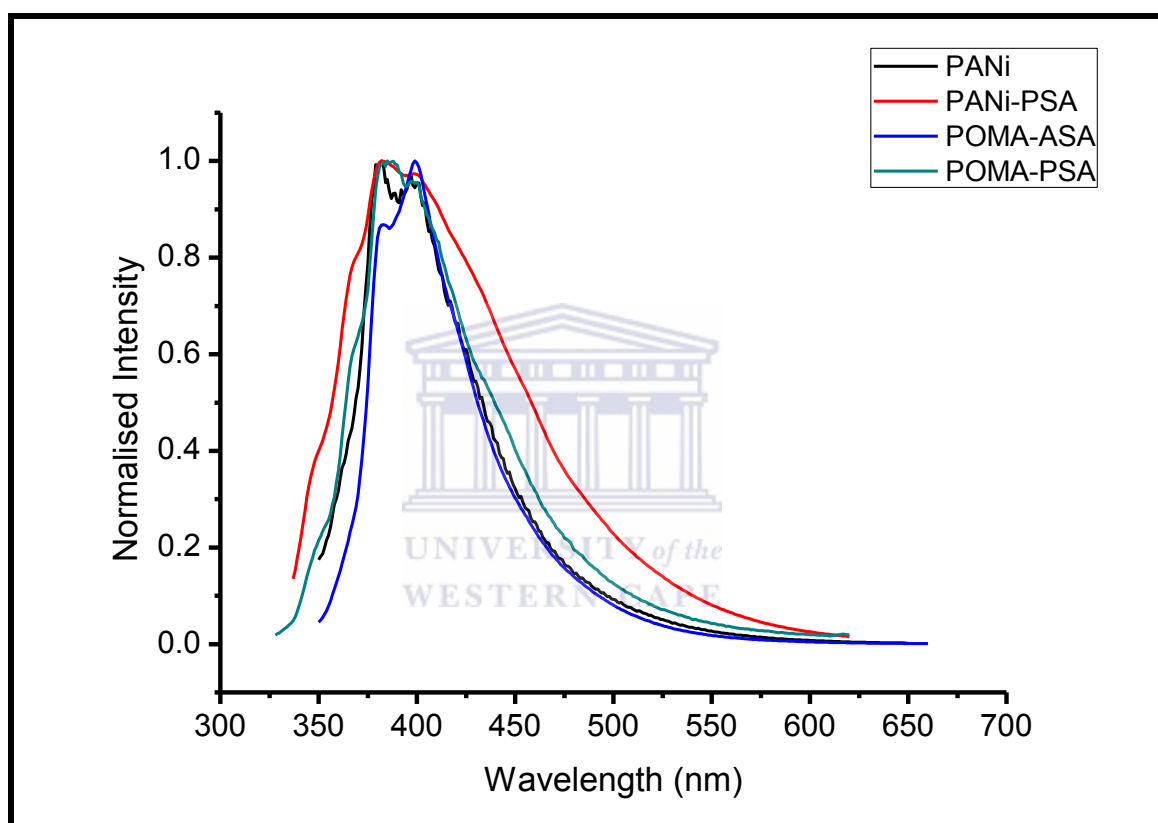


Figure 4.9: The fluorescence spectra of the conjugated polymers

The emission spectra of the conjugated polymers have a peak at the low energy levels. This is as a result of the formation of the excimer between the chain of the polymer at its excited state and another chain of the polymer at its ground state. The shoulder is more pronounced in PANi, PANi-PSA and POMA-PSA than in POMA-ASA.

Seemingly there is no obvious relation between the wavelength at which the emission occurs and the fluorescence quantum yield as shown in Table 3. The fluorescence quantum yields that were calculated are as follows, 0.41, 0.56, 0.50 and 0.18 for PANi, PANi-PSA, POMA-ASA and POMA-PSA, respectively. There have been reports of the band gap and the fluorescence quantum yield being related, an increase in the band gap has been reported to lead to an increase in the fluorescence quantum yield by Kim *et.al* [115]. This comes as a result of a decrease in the extent of conjugation. When considering these findings it is expected that the PANi should have the lowest fluorescence quantum yield and the POMA-ASA the highest fluorescence quantum yield. This is not the case in this instance; POMA-PSA is the one with the lowest quantum yield of 0.18. This shows that other factors are influencing the fluorescence quantum yield. The underlying factor is the existence of the excimers that are able to quench the fluorescence of the polymers leading to lowered values of the fluorescence quantum yield [90].

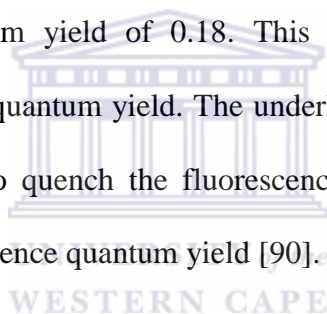
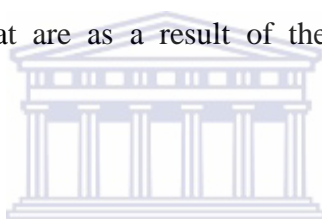


Table 3: The absorption and emission wavelength maxima with the Stokes shift values and fluorescence quantum yield values

Polymer	Absorption λ_{\max} (nm)	Emission λ_{\max} (nm)	Stokes shift (nm)	Φ_f
PANi	331	391	60	0.41
PANi-PSA	335	393	58	0.56
POMA-ASA	320	385	65	0.50
POMA-PSA	323	385	62	0.18

4.2.4 Photoluminescence of the ZnGa₂O₃ nanoparticles

Generally it is agreed upon that when a semi conductor material is exposed to a photon of light, there is excitation of the electron from the valence band to the conduction band thereby leaving a hole in the valence band. An electron hole pair is formed because of the existence of coulombic forces between the particles. The electron hole pair is referred to as an exciton. When the electron-hole pair recombines, energy is released in the form of photoluminescence. There are additional factors that contribute to the excitation and emission spectrum of the nanoparticles for oxide compounds. The presence of the oxide moiety leads to observation of transitions that are due to the oxygen vacancies [116]. As a result there can be observation of transitions that are as a result of the charge transfer between the transition metal and oxygen.



The emission and excitation spectrum of the nanoparticles is shown in **Figure 4.10**, with the excitation and emission peak being a mirror image of each other, this is indicative of that there are no geometric changes within the nanoparticles upon excitation. The emission spectrum of the synthesised nanoparticles showed three peaks at 425 nm, 440 nm, 493 nm and 535 nm. The peak at 425 nm is as a result of the relaxation of the exciton of the nanoparticles from the excited state to the ground state. The peak at 493 nm is as a result of the interaction between the oxygen vacancies and gallium [117]. There is observation of vibronic vibrations at 493 nm and 535 nm.

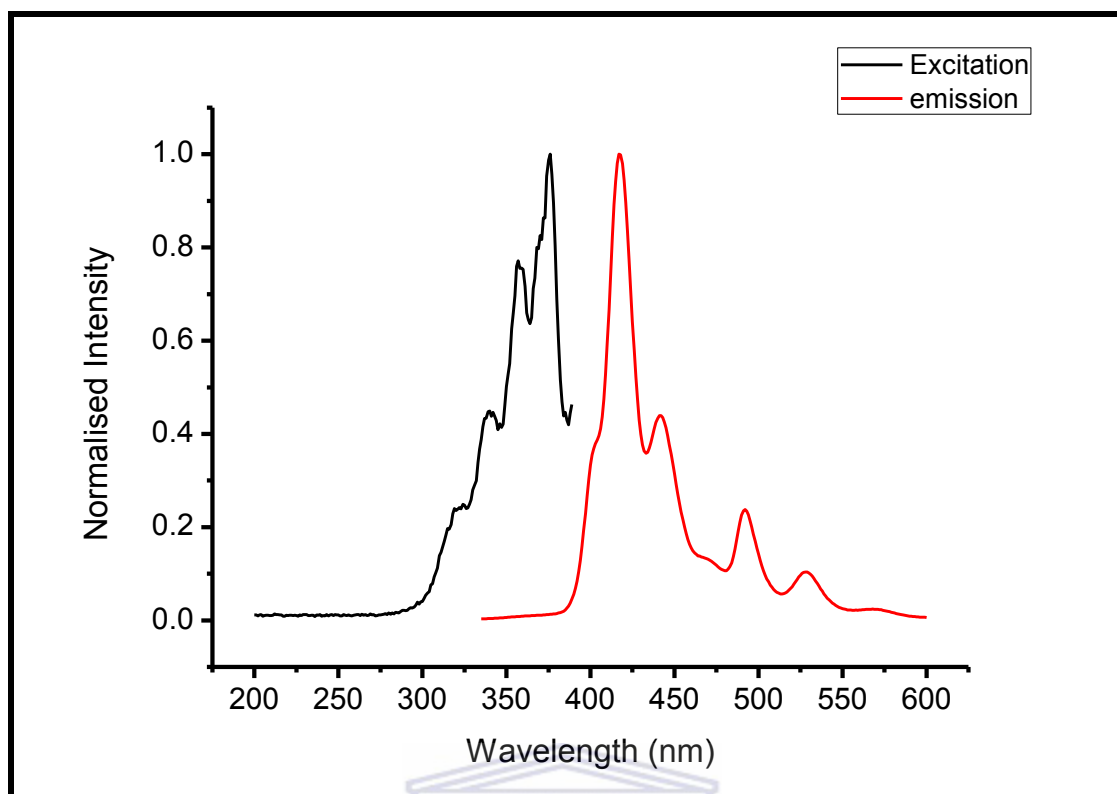
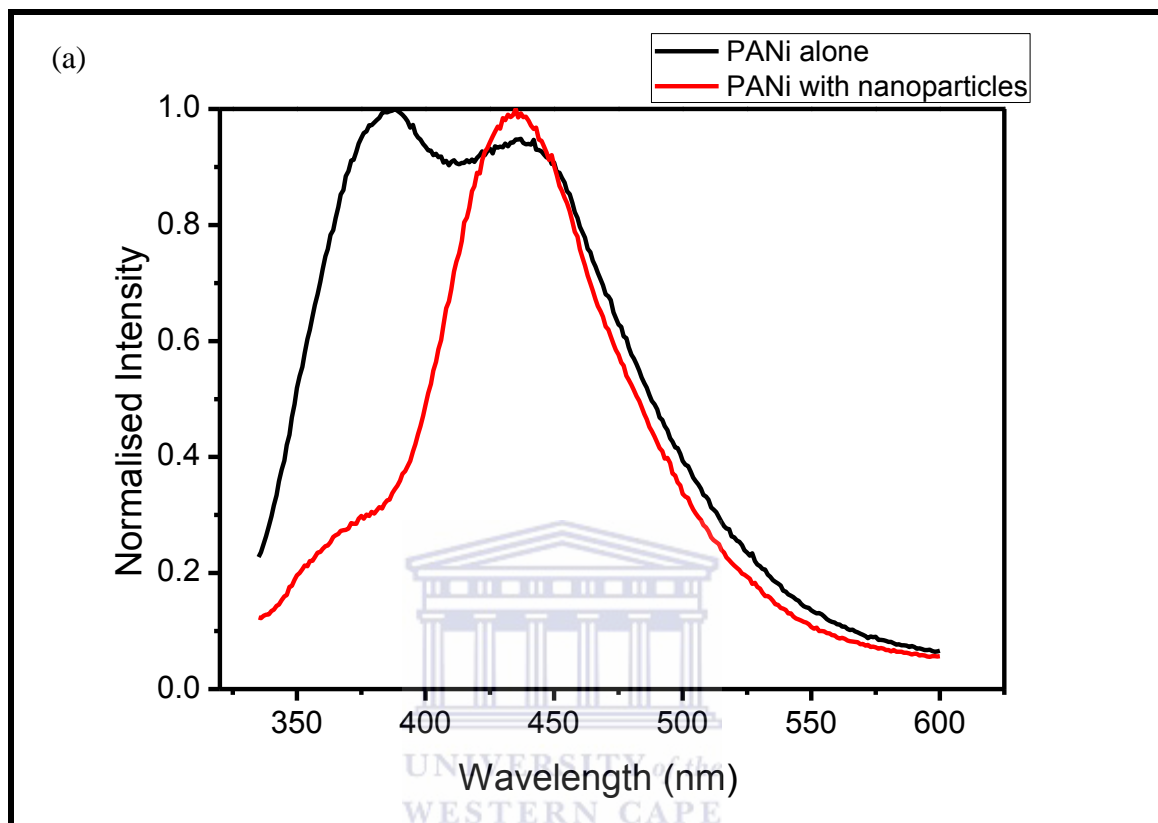


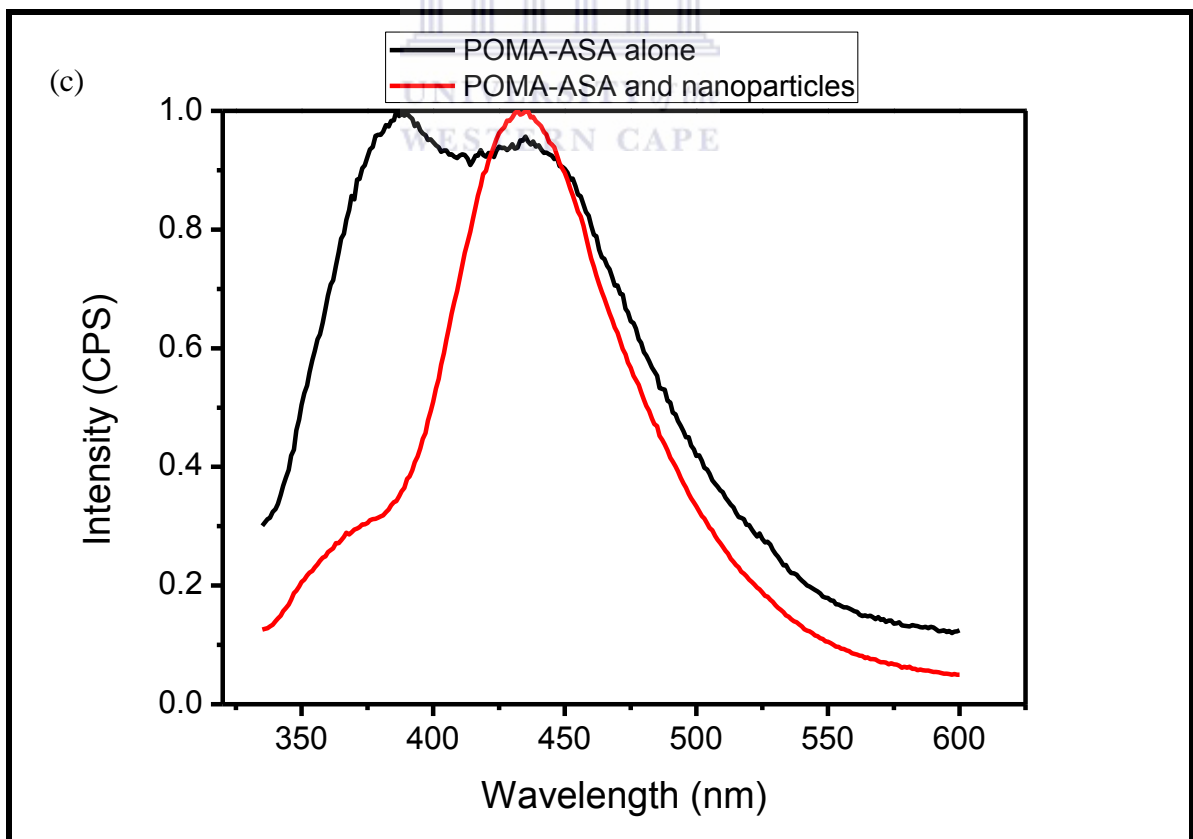
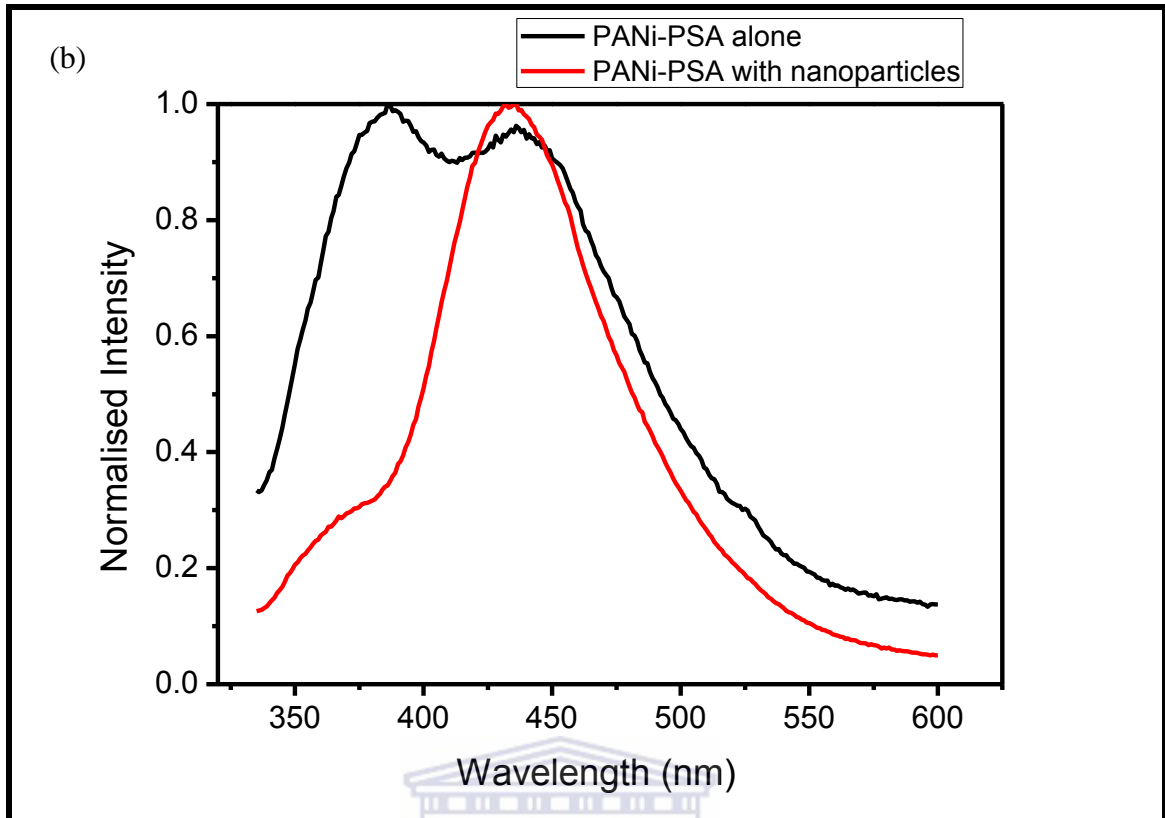
Figure 4.10: The excitation and emission spectra of ZnGa₂O₄ nanoparticles

4.2.5 Photoluminescence behaviour of the Conjugated Polymers with the nanoparticles in solution

The nanoparticles that were used were explored for the potential use as acceptors in photovoltaic cells. The effect of the presence of the nanoparticles in the photoluminescence spectra of the polymers is a very important parameter that needs to be explored so as to determine the applicability of a compound as an acceptor in the photovoltaic system. The photoluminescence was measured for the polymers in the absence and presence of the polymers at an excitation wavelength of 320 nm. Overall for all the polymers there is an enhancement of the emission at the low energy range and decrease in the intensity of the peak at high energy as shown in **Figure 4.11**. As discussed in section 4.2.3 the emission that is observed at low energies is as a result of the excimers that are formed as a result this suggests that the presence of the

nanoparticles might lead to a greater degree of quenching of the emission of the polymer by the excimers.





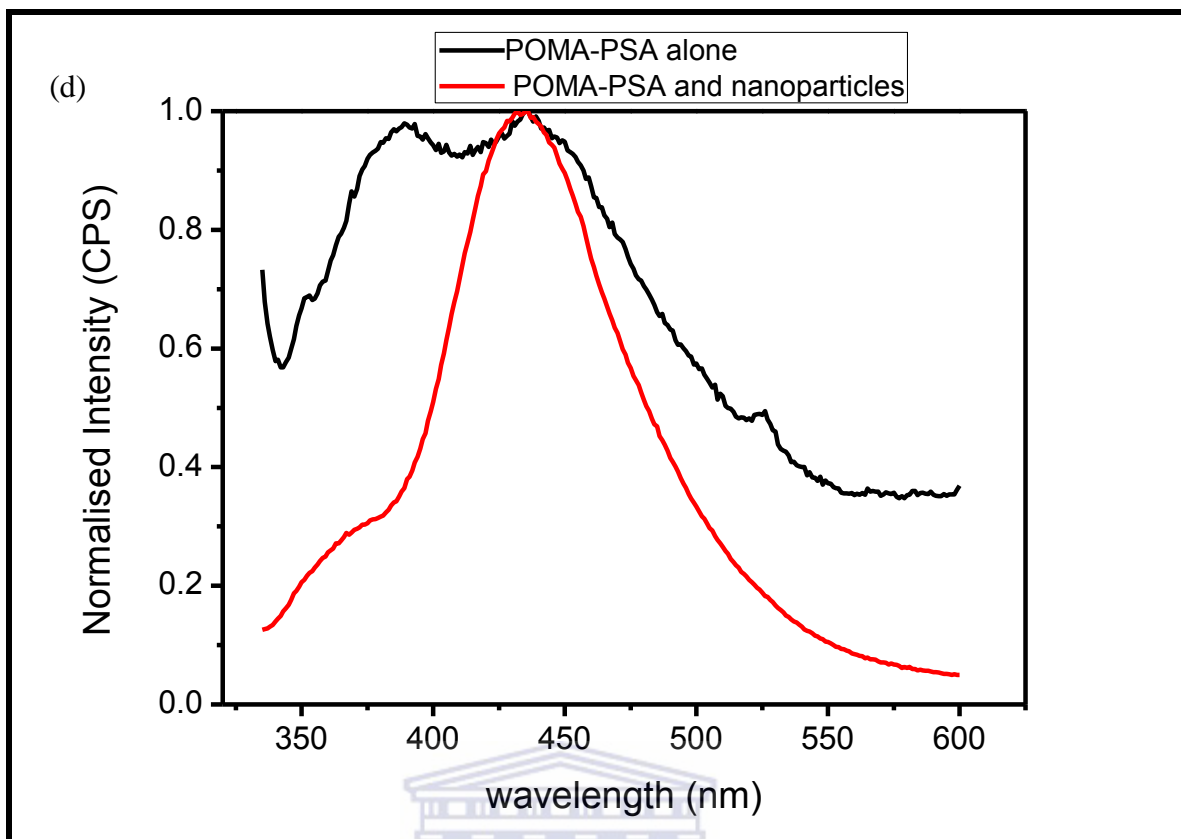


Figure 4.11: The emission of the (a) PANi alone and PANi with nanoparticles (ZnGa_2O_4) (b) PANi-PSA alone and PANi-PSA with nanoparticles (ZnGa_2O_4) (c) POMA-ASA alone and POMA-ASA with nanoparticles (ZnGa_2O_4) (d) POMA-PSA alone and POMA-PSA with nanoparticles (ZnGa_2O_4) in DMSO at an excitation wavelength of 320 nm

4.3 MORPHOLOGICAL ANALYSIS FROM SEM

4.3.1 Conjugated Polymers

The morphology of the different polymers, POMA-ASA, POMA-PSA, PANi and PANI-PSA was investigated. All the represented data shown for the polymers is at a magnification of 100 000X. The SEM images for the POMA-ASA and POMA-PSA are depicted in **Figure 4.12**. POMA-ASA (**Figure 4.12(a)**) was shown to display micelle like character. The POMA-PSA (**Figure 4.12(b)**) showed tubular structures that are ~200 nm in length. The tubular morphology of the POMA-PSA is

advantageous in solar cells since it allows for a better interface interaction between the donor and acceptor.

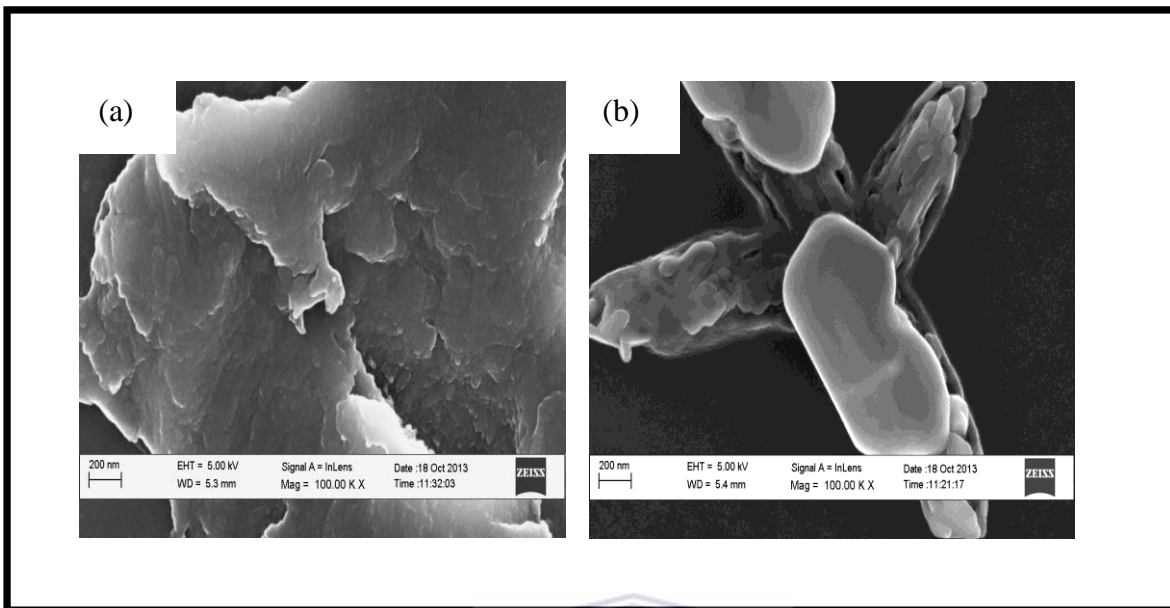


Figure 4.12: SEM images of (a) POMA-ASA and (b) POMA-PSA

The micrographs for PANi and PANi-PSA are depicted in **Figure 4.13**. It can be seen that the PANi (**Figure 4.13(a)**) has formed a densely interconnected fibers. The PANi-PSA (**Figure 4.13(b)**) shows the same arrangement as seen for the PANi.

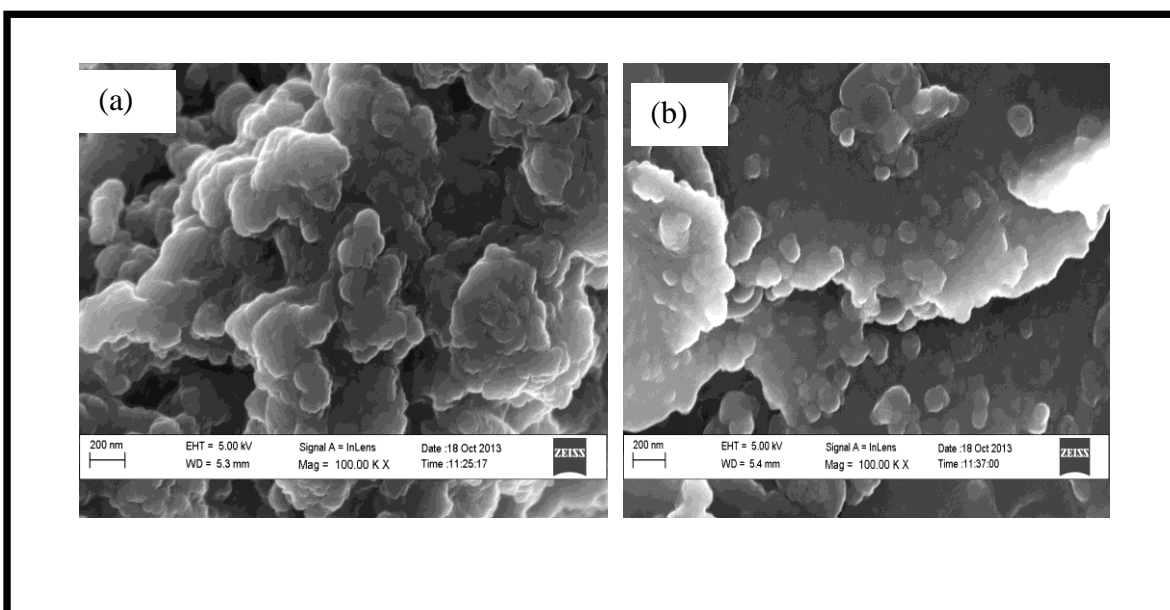


Figure 4.13: SEM images of (a) PANi and (b) PANi-PSA

4.4 X-RAY DIFFRACTION PATTERN OF THE CONJUGATED POLYMERS

Polymers can come in many forms. They can display crystalline, semi crystalline and amorphous behaviour. In most cases it is found that one polymer exists in all three states [118]. The polyaniline and its derivative can be characterised as highly crystalline as shown from their XRD data, **Figure 4.14**. Even though the polyaniline and its derivatives can be classified as crystalline, there are minute traces of amorphous behaviour. These traces of a higher degree amorphous behaviour are more pronounced in the doped PANi derivatives, that is PANi-PSA, POMA-PSA and POMA-ASA. This suggests that the doping of the PANi with sulfonic acid introduces a level of disorder within the structure. Crystallinity in polymers is as the result of the folding of the polymer within itself, a highly ordered folding leads to a highly crystalline structure. The fact that there is a lowered level of crystallinity with doping suggests that the bulky sulfonic acid groups act as a hindrance in the folding process of the polymers. This may be as result of the branched structure that is formed when there is incorporation of the sulfonic acid groups. The degree of disorder is higher for the anthracene sulfonic acid substituted polymer in comparison with the phenanthrene sulfonic acid. The latter is because of the linear bulky structure of the anthracene sulfonic acid dopant which has a lower degree of flexibility in comparison with the phenanthrene sulfonic acid dopant which has a more angular characteristic.

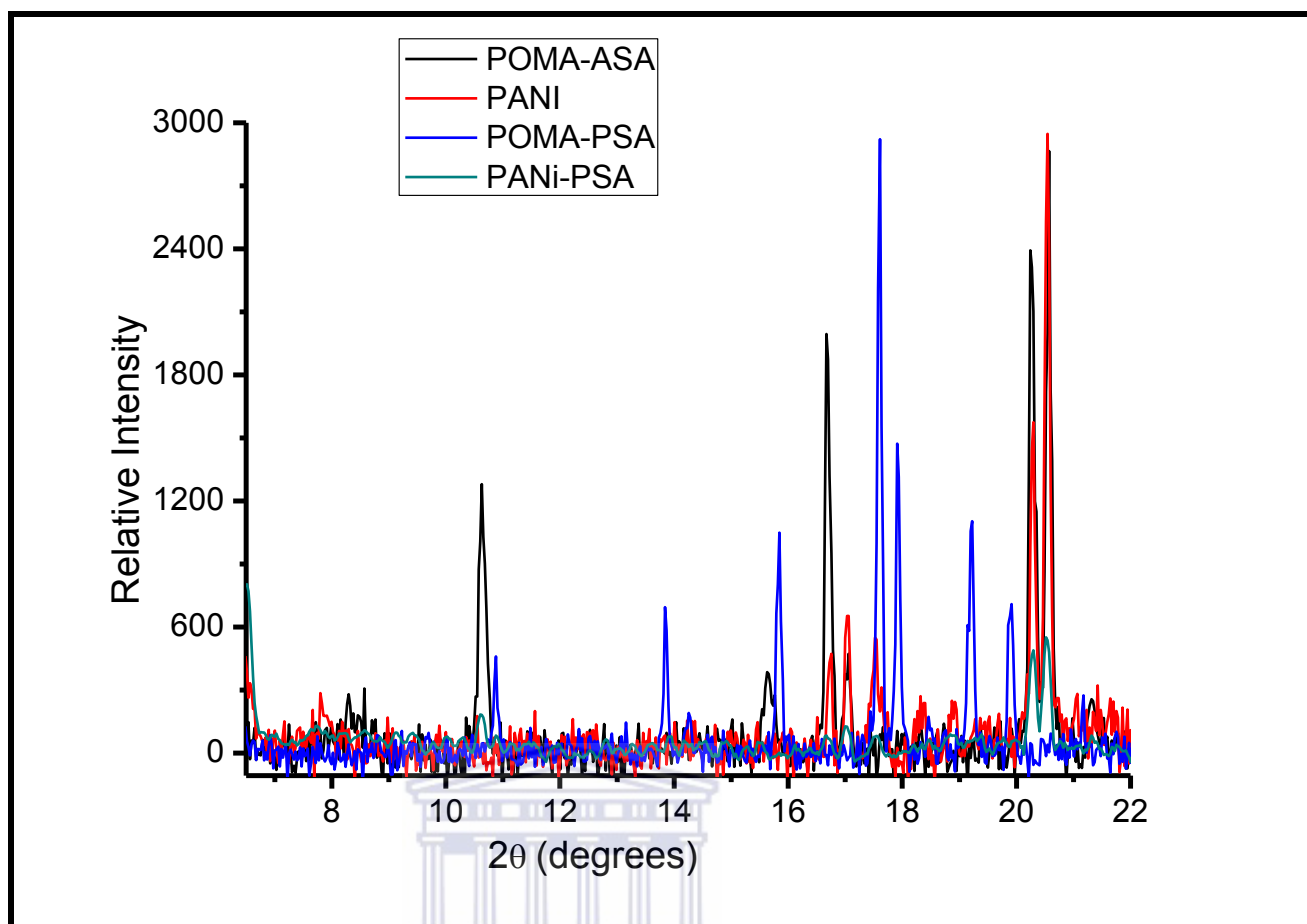


Figure 4.14: X-ray Diffraction pattern of the conjugated polymers

4.5 X-RAY DIFFRACTION PATTERN OF THE $ZnGa_2O_4$

The general XRD spectrum for the nanoparticles is characterised by a high level of crystallinity, **Figure 4.15**. The XRD data of the $ZnGa_2O_4$ revealed that there are combination characteristics displayed by the sample. There are characteristics that are as a result of the $ZnGa_2O_4$ and also the slightly amorphous characteristic that is due to the presence of GaO(OH) which is observed at a peak position where $2\theta = 33.4-34.2$ [119]. The presence of characteristics that are due to the GaO(OH) is because of the temperature at which synthesis was done which was lower than $200\text{ }^\circ\text{C}$.

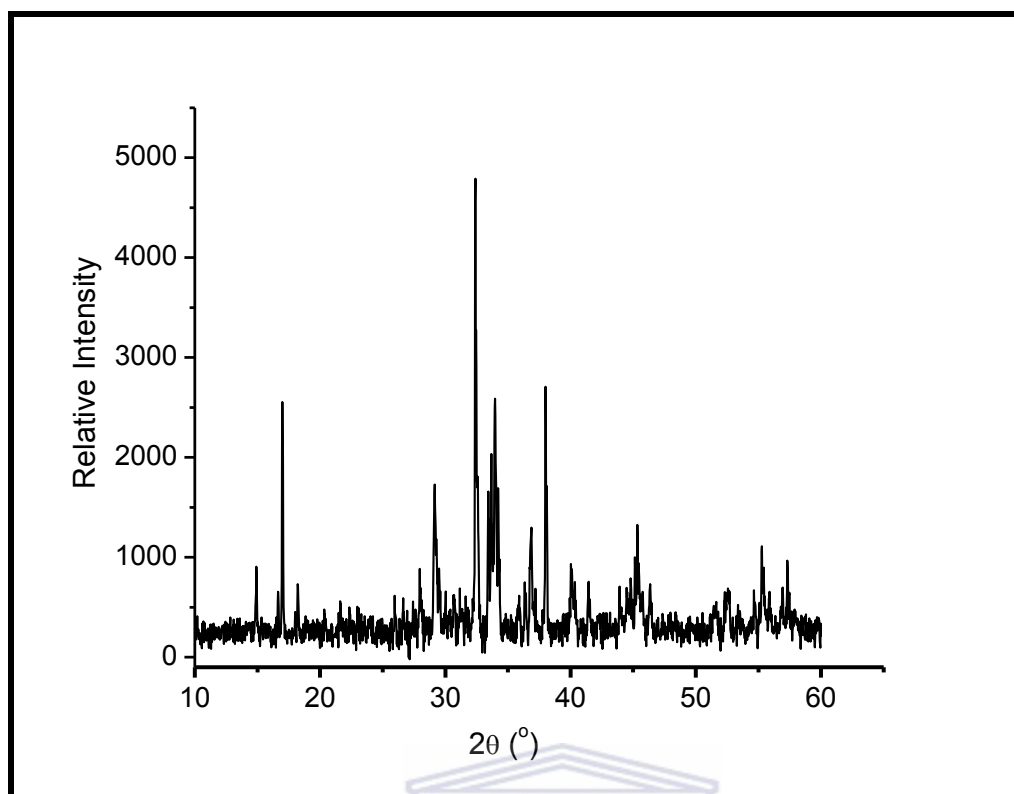


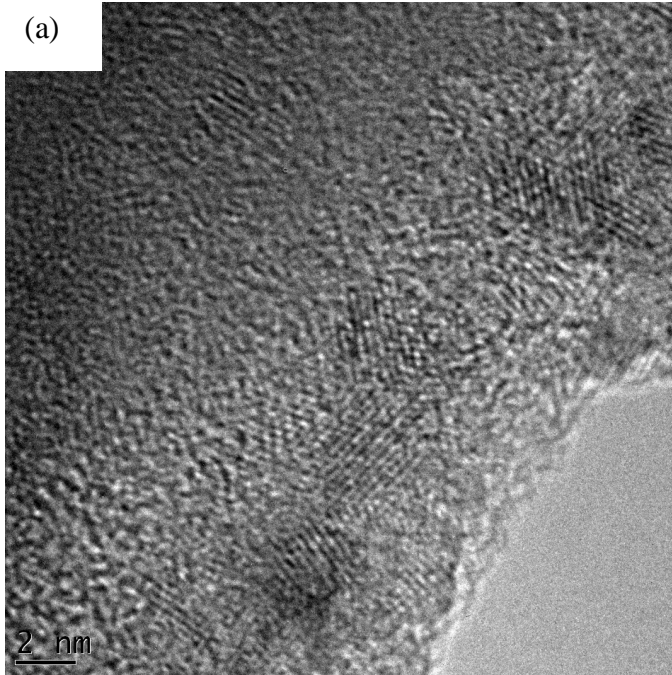
Figure 4.15: X-ray diffraction pattern of the ZnGa_2O_4 nanoparticles

4.6 MORPHOLOGICAL ANALYSIS FROM TEM

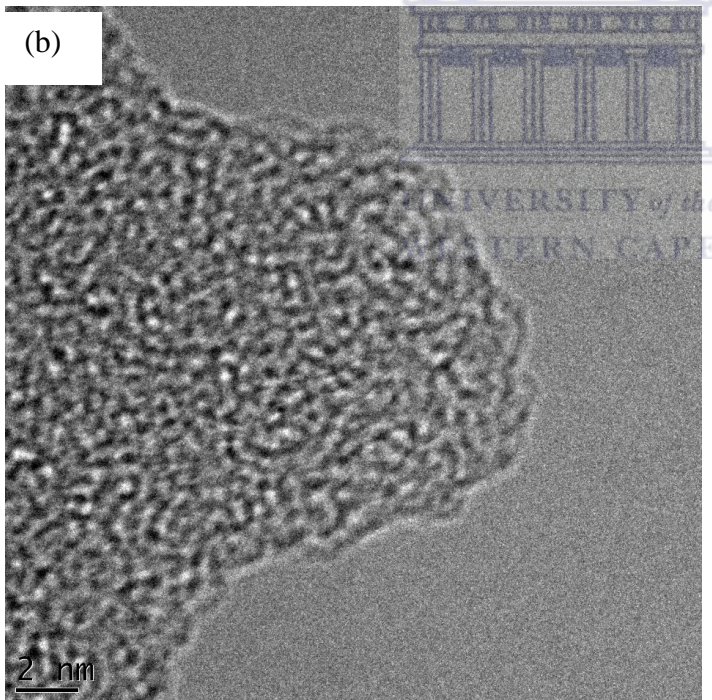
4.6.1 Conjugated Polymers

As seen in **Figure 4.16**, TEM allows for the monitoring of the way the chains of the polymers are folded. As previously stated in **Section 4.4**, folding of the polymeric chains determine the level of crystallinity of the compound. The images show a high degree of crystallinity for PANi and POMA-PSA, **Figure 4.14(a) and (c)**. The latter can be concluded because of the presence of well defined ridges within the images of the polymer chains. The PANi-PSA (**Figure 4.14(b)**) and POMA-ASA (**Figure 4.14(d)**) display the lowest level of crystallinity, with the POMA-ASA being the worst one. This agrees with the XRD data, the PANi was highly crystalline and POMA-ASA showed a more amorphous behaviour. This can be as a result of the nature of the doping agent that is anthracene sulfonic acid has a linear, rigid structure that is hindering a well ordered folding process of the polymer.

(a)



(b)



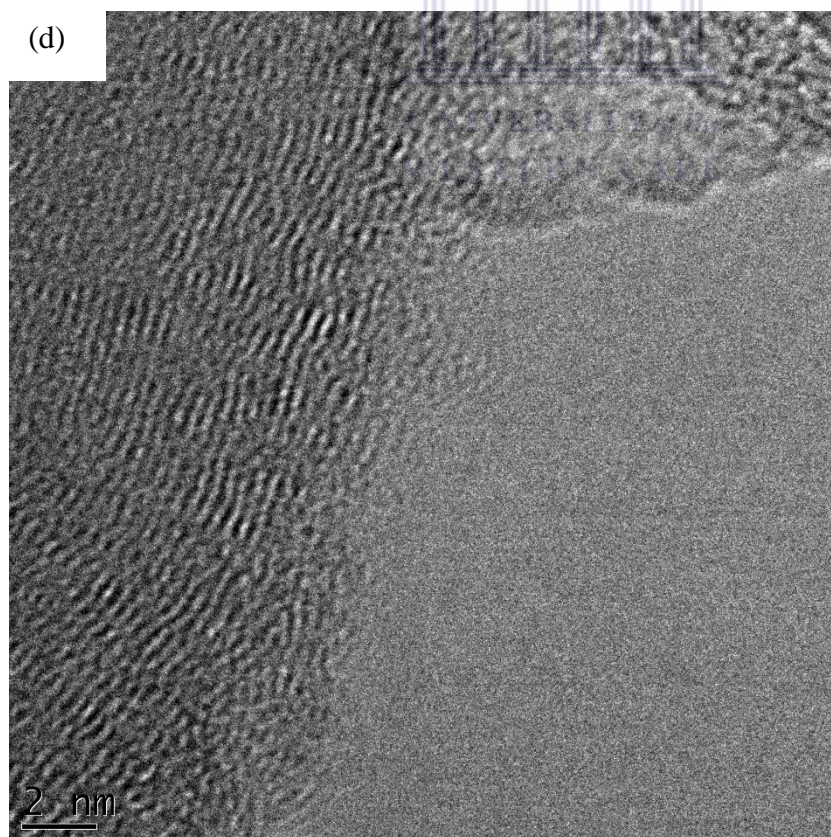
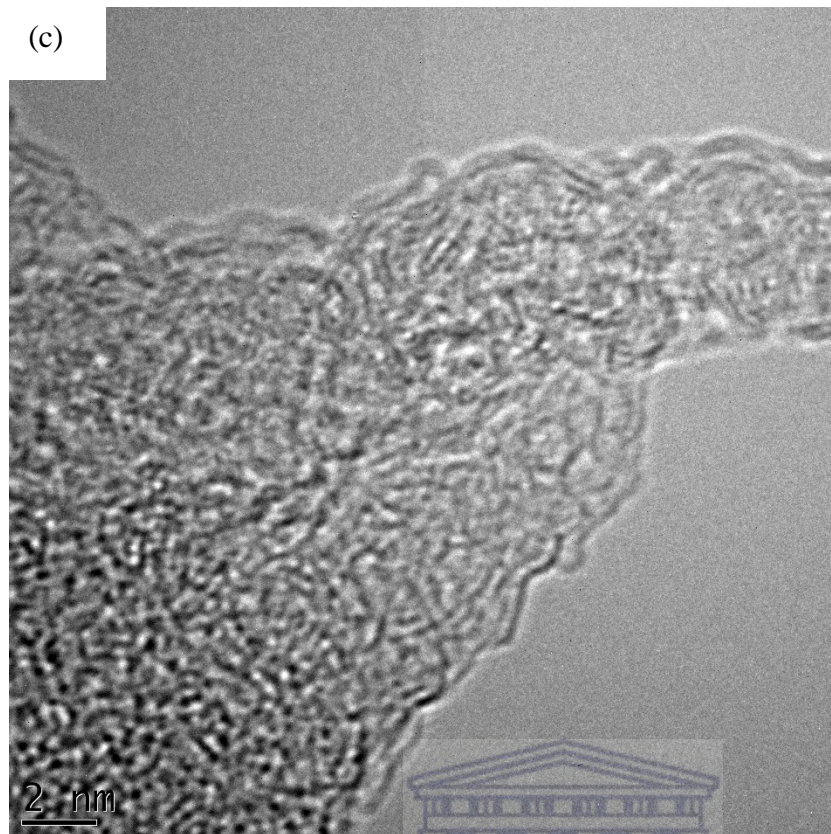


Figure 4.16: TEM images of (a) PANi (b) PANi-PSA, (c) POMA-ASA and (d) POMA-PSA

4.5.2 ZnGa₂O₄ nanoparticles

The TEM images of the nanoparticles are highly agglomerated nanorods, **Figure 4.17(a)**. The image of the agglomerated nanorods, in **Figure 4.17(b)**, at higher magnification shows the presence of ridges which is indicative of a crystalline compound.

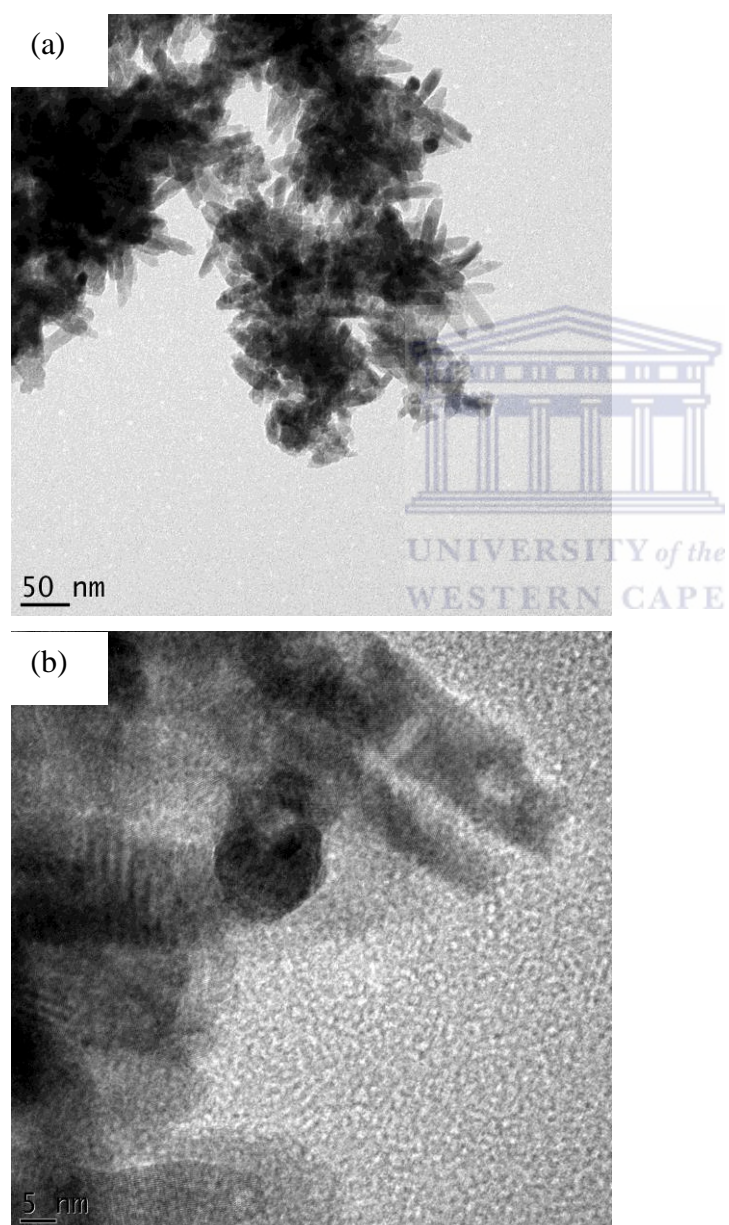
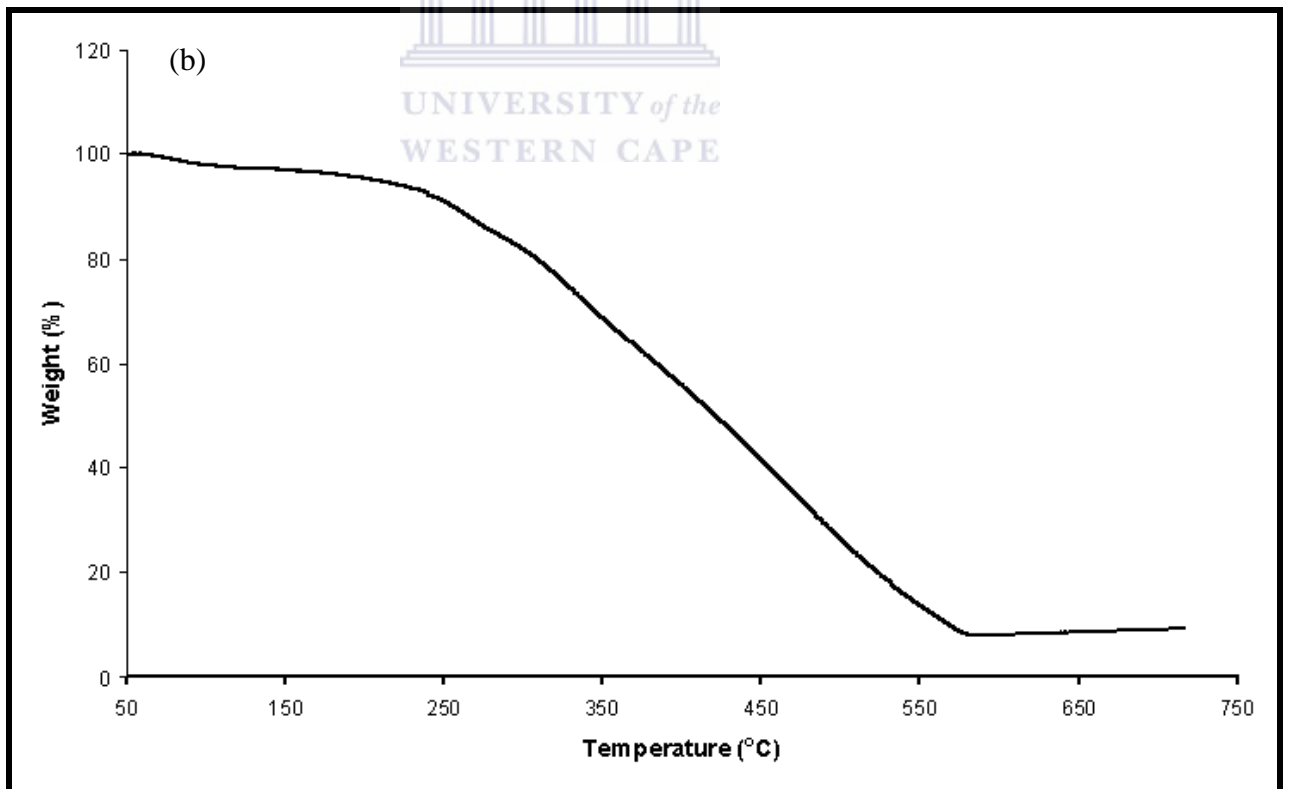
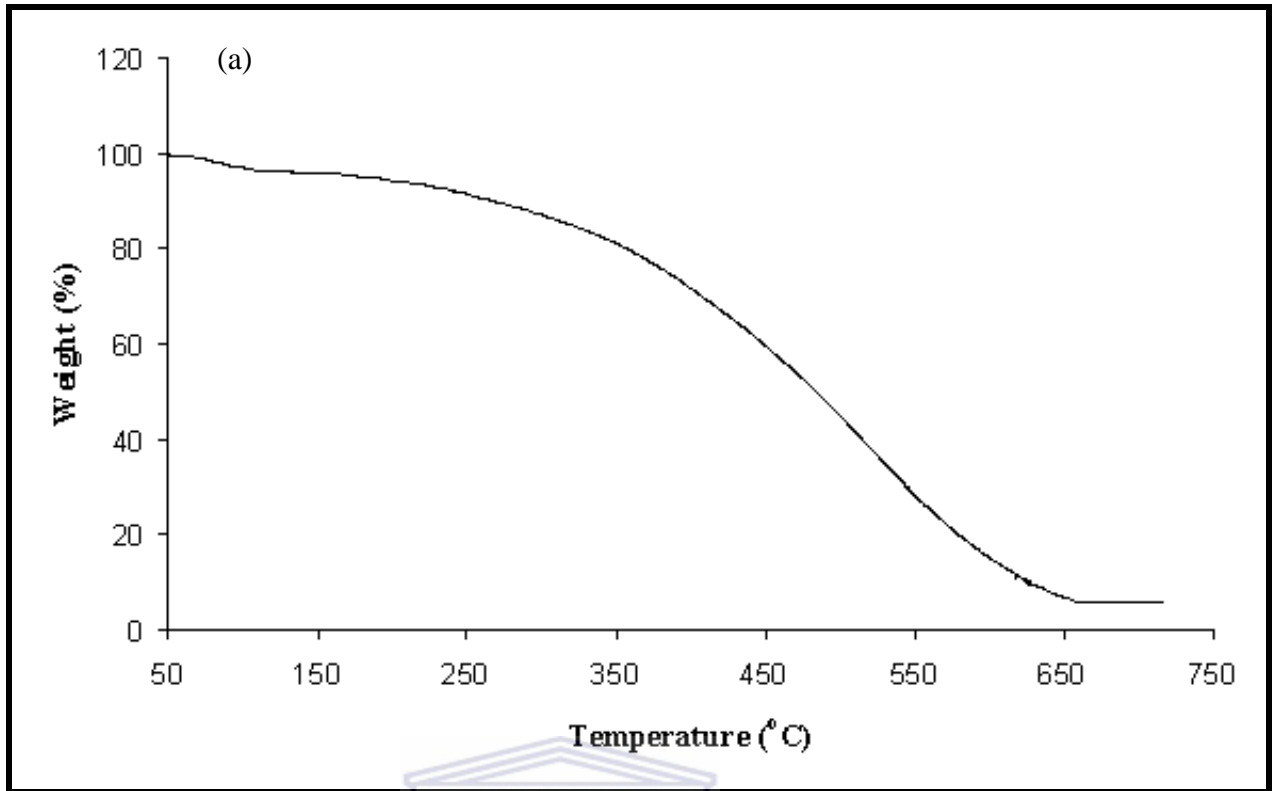


Figure 4.17: TEM images of ZnGa₂O₄ at a (a) 100 000 X magnification and (b) at 500 000X magnification

4.7 THERMAL GRAVIMETRIC ANALYSIS OF THE CONJUGATED POLYMERS

The thermal gravimetric analysis (TGA) of the polyaniline shows two transitions, **Figure 4.18(a)**. The one that is due to the loss of water and one due to the breakdown of polyaniline into its scission products such as aniline, ammonia [120]. The loss of water transpires at ~ 100 °C and is observed because of the hydroscopic nature of polyaniline. The polymeric chain of the polyaniline undergoes degradation at temperatures above 300 °C to form scission products depicted in **Figure 4.19**. These products undergo further degradation to form ammonia at temperatures above 450 °C. The PANi-PSA undergoes three transitions, **Figure 4.18(b)**. The transition due to the loss of water is observed together, at ~ 110 °C. This is followed by another transition at ~ 250 °C that is as a result of the loss of the dopant, which is in this case phenanthrene sulfonic acid. This is followed by the degradation of the chain length that occurs at temperatures above 300 °C.

The POMA-PSA and POMA-ASA also undergoes three transitions when analysed using TGA as seen in **Figure 4.18(c) and 4.18(d)**. The transitions that are observed are the loss of water at 100 °C and 110 °C for POMA-ASA and POMA-PSA, respectively. This is followed by the transition that is due to the loss of the dopants that is observed at 250 °C for the POMA-ASA and 290 °C for the POMA-PSA. The degradation of the polymeric chain for POMA-ASA and POMA-PSA occurs at temperatures of 300 °C and 350 °C, respectively. Overall it is seen that the polymers are stable at high temperatures. The subtle differences in the temperatures that undergo degradation between the polymers can be attributed to the use of different masses.



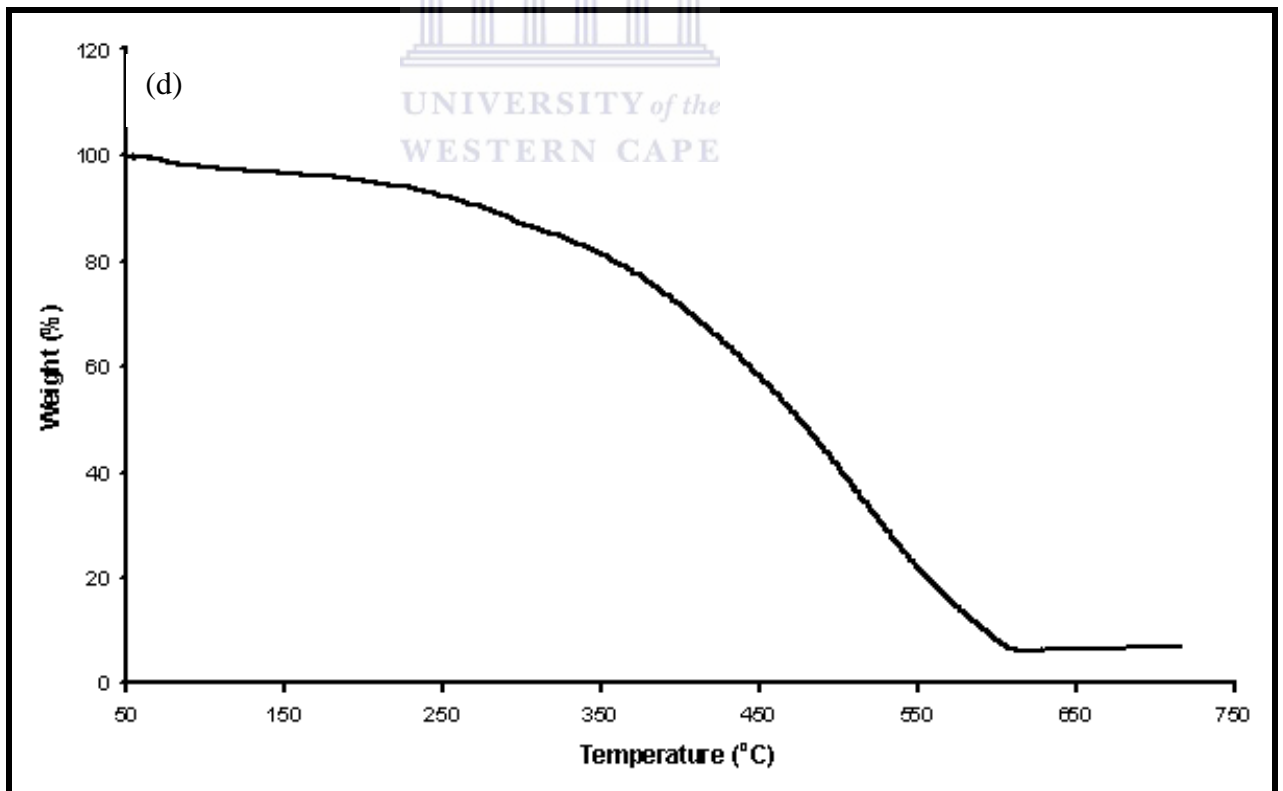
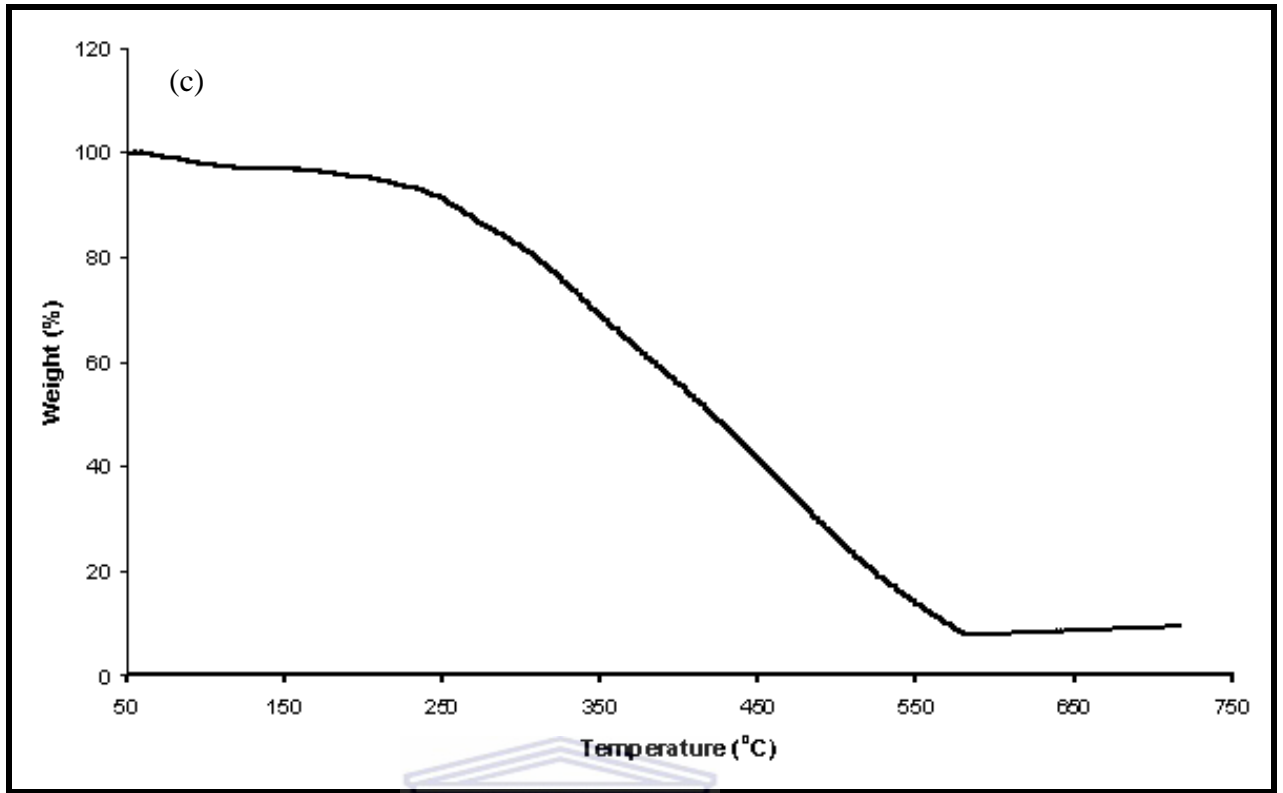


Figure 4.18: Thermal gravimetric curve of (a) PANi, b) PANi-PSA, c) POMA-ASA, d) POMA-PSA

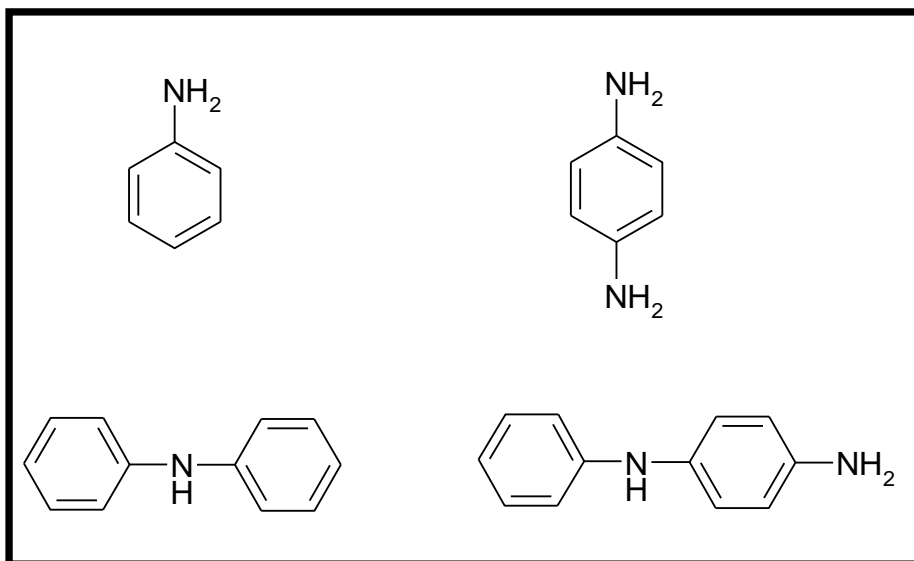
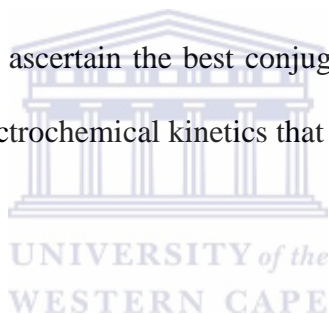


Figure 4.19: Possible degradation products from thermal gravimetric analysis of the conjugated polymers



CHAPTER 5 : ELECTROCHEMICAL CHARACTERISATION OF THE CONJUGATED POLYMERS

Analysis of the electrochemical kinetics is depicted in this chapter. There is use of two techniques for the analysis of the electrochemical parameters for the conjugated polymers. It is cyclic voltammetry and electrochemical impedance spectroscopy. The use of these techniques determines the ease at which charge transfer occurs for the different polymers. This is to ascertain the best conjugated polymer for photovoltaic application in terms of the electrochemical kinetics that is obtained.



5.1. CYCLIC VOLTAMMETRY OF THE CONJUGATED POLYMERS

The cyclic voltammetry of PANi paste was obtained using 1 M HCl is shown in **Figure 5.1**. There is only one reduction and oxidation peak that is observed for the PANi as shown in **Figure 5.1**. The oxidation peaks are occurring at +295 mV and +420 mV. The peak at +110 mV is due to the emeraldine form of polyaniline. The polyemeraldine is further oxidised to form polyemeraldine radical cation. The radical cation gets reduced at +254 mV to form a partly reduced polyleucoemeraldine. The latter undergoes further reduction at +107 mV to form fully reduced polyleucoemeraldine [47, 121]. The peak potentials and corresponding currents are also seen to vary as the scan rates value varies. This indicates that the polymer nanomaterial structures are conducting and that diffusion of electrons was taking place along the polymer chain [62].

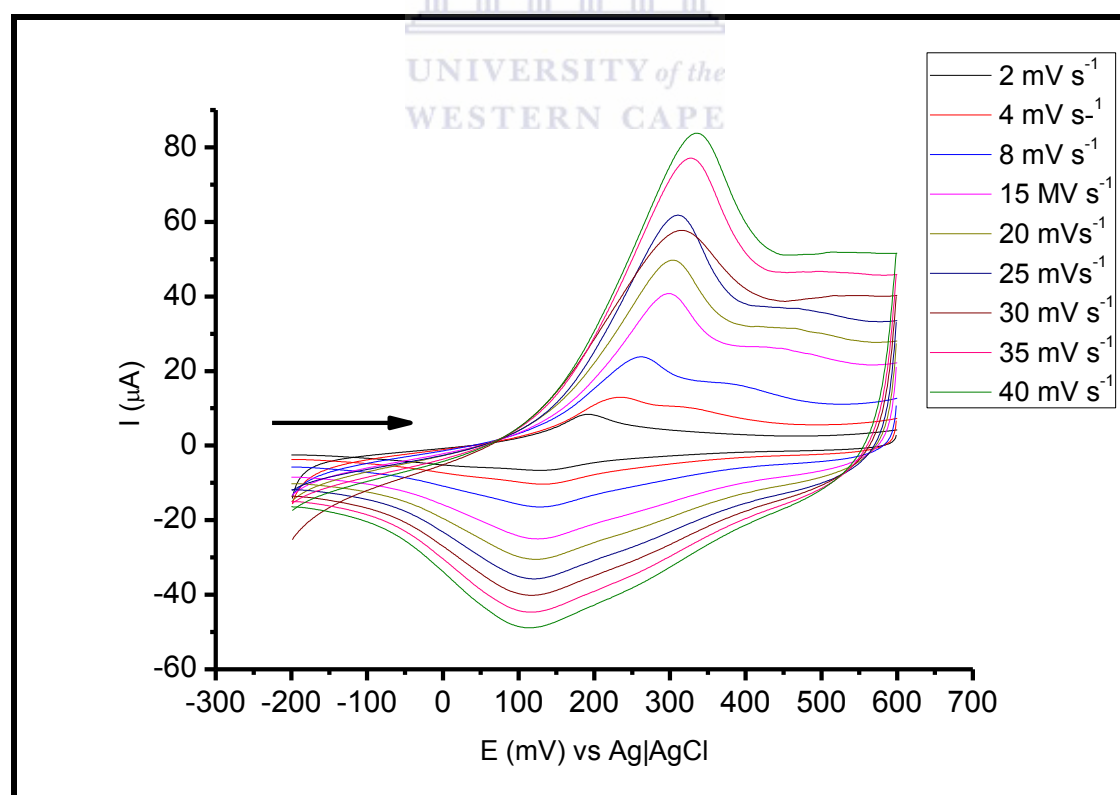


Figure 5.1: Scan rate dependence of the cyclic voltammetry of PANi paste in 1 M HCl

The cyclic voltammetry of PANi-PSA paste was obtained using 1 M HCl is shown in **Figure 5.2**. The oxidation peaks are occurring at +110 mV and +282 mV. The peak at +110 mV is due to the emeraldine form of polyaniline. The polyemeraldine is further oxidised to form polyemeraldine radical cation. The radical cation gets reduced at +210 mV to form a partly reduced polyleucoemeraldine. The latter undergoes further reduction at +100 mV to form fully reduced leucoemeraldine [47, 62, 121] . The peak potentials and corresponding currents are also seen to vary as the scan rates value varies. This indicated that the polymer nanomaterial structures are conducting and that diffusion of electrons was taking place along the polymer chain [62].

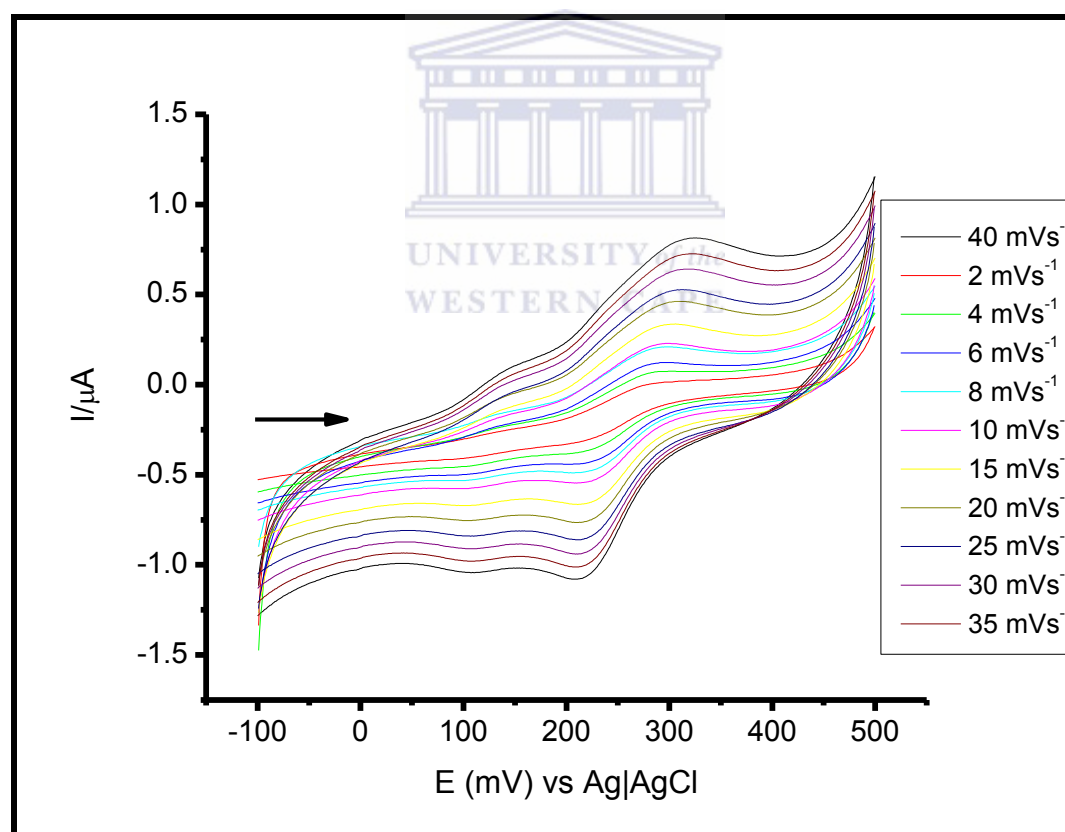


Figure 5.2: Scan rate dependence of the cyclic voltammetry of the PANi-PSA paste in 1 M HCl

There is only one reduction and oxidation peak that is observed for the POMA-PSA as shown in **Figure 5.3**. There is an oxidation peak occurring at +261 mV for the

formation of polyemeraldine radical cation. There reduction peak is occurring at +208 mV for the formation of the partly reduced polyleucoemeraldine. The peak potentials and corresponding currents are also seen to vary as the scan rates value varies. This indicates that the polymer nanomaterial structures are conducting and that diffusion of electrons was taking place along the polymer chain [62].

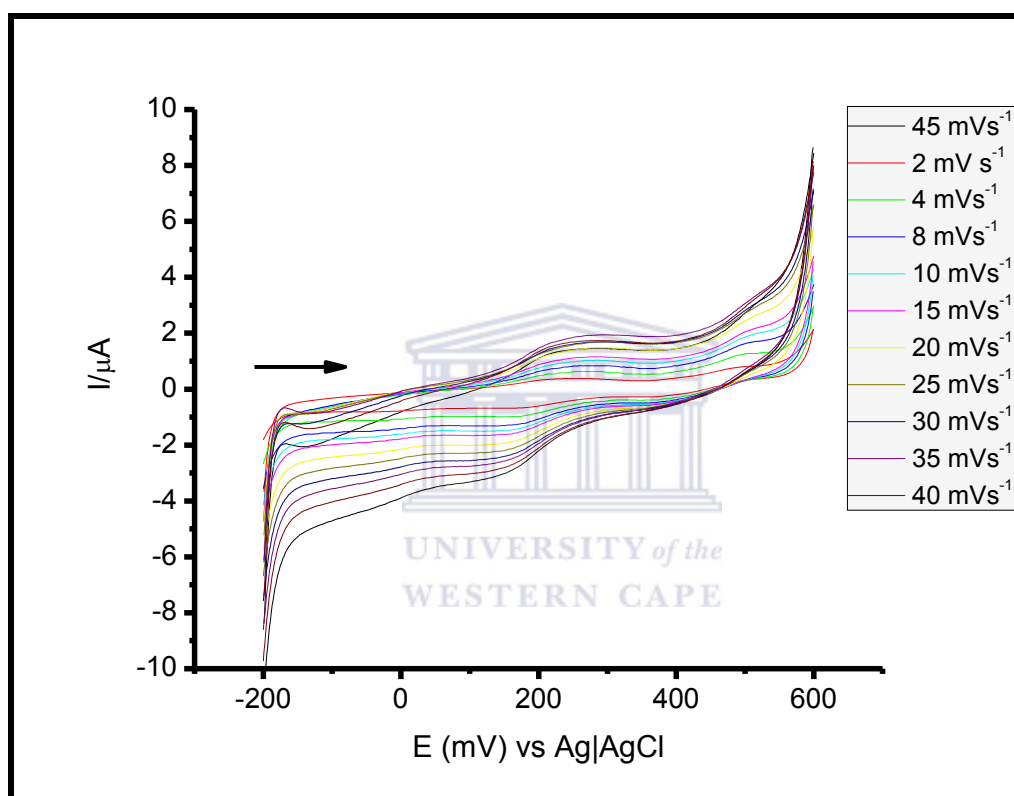


Figure 5.3: Scan rate dependence of the cyclic voltammetry of the POMA-PSA paste in 1 M HCl

The paste of POMA-ASA also has one oxidation and one reduction peak as shown in **Figure 5.4**. The oxidation peak at +317 mV is as a result of the polyemeraldine radical cation and the reduction peak at +248 mV is as a result of the formation of the partly reduced polyleucoemeraldine. The peak potentials and corresponding currents are also seen to vary as the scan rates value varies. This indicates that the polymer

nanomaterial structures are conducting and that diffusion of electrons was taking place along the polymer chain [62].

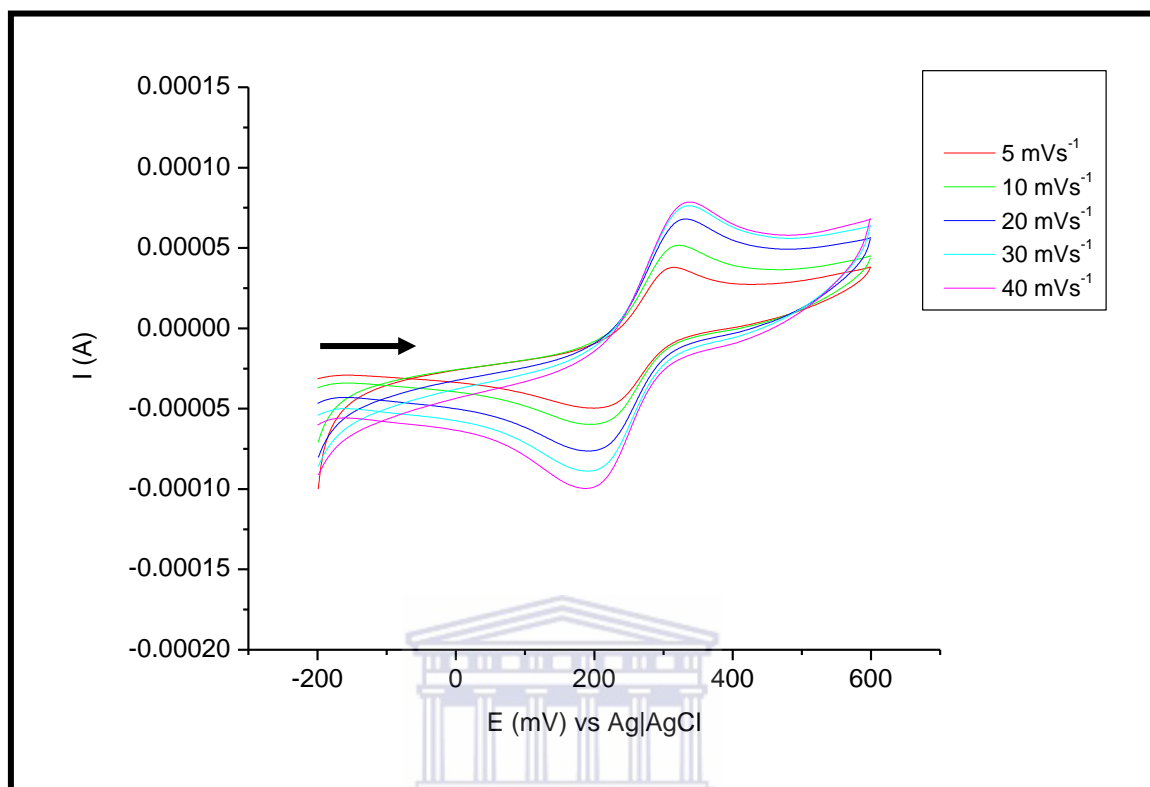


Figure 5.4: Scan rate dependence of the cyclic voltammetry of the PANi-PSA paste in 1 M HCl

The number of electrons transferred (n) was estimated from the CV and was calculated for each of the polymers, using the equation 5.1 below.

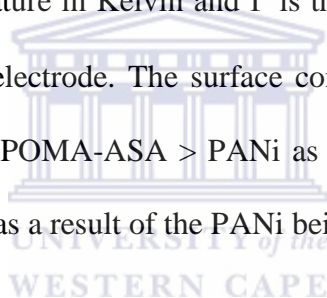
$$E - E_{1/2} = \frac{2.20RT}{nF} \quad 5.1$$

Where E is the maximum peak potential, $E_{1/2}$ is the half maximum peak potential, R is the gas constant ($8.314 \text{ J mol}^{-1} \text{ K}^{-1}$), T is the temperature of the system in Kelvin, F is the Faradays constant (96584 C mol^{-1}) and n is the number of electrons transferred. The number of electrons transferred was found to be approximately one for all of the polymers. The linear dependence of peak current on the scan rate for the various polymers showed that we have a thin film of conducting electroactive material

immobilised on the electrode, which undergo rapid electron transfer reactions [122]. Since the behaviour is the same as a surface confined species, it is possible to determine the surface concentration of the polymers on the platinum electrode. The surface concentration ($\Gamma = \text{mol cm}^{-2}$) of the adsorbed electroactive species is able to be calculated approximately from a plot of I_p versus v in accordance with the Brown Anson model,

$$I_p = \frac{n^2 F^2 \Gamma A v}{4RT} \quad 5.2$$

where I_p is the maximum current peak, n is the number of electrons transferred, F is the Faradays constant, A is the surface area of the electrode, v is the scan rate, R is the gas constant, T is the temperature in Kelvin and Γ is the surface concentration of the electroactive species on the electrode. The surface concentration is increasing from PANI-PSA > POMA-PSA > POMA-ASA > PANi as shown in Table 4. The higher surface coverage for PANi is as a result of the PANi being free from bulky dopants.



The quantitative analysis of the diffusion process was done by the determination of the diffusion coefficient from the Randle Sevčik equation for a reversible system:

$$I_p = 2.69 \times 10^5 n^{3/2} A D^{1/2} C v^{1/2} \quad 5.3$$

where I_p is the maximum current peak, n is the number of electrons exchanged during the redox process, A (cm^2) the active area of the working electrode, D the diffusion coefficient ($\text{cm}^2 \text{s}^{-1}$), C is the bulk concentration of the electroactive species (mol cm^{-3}) and v is the voltage scan rate (V s^{-1}). The values found showed that there is an increase in the diffusion coefficient from POMA-ASA > POMA-PSA > PANi-PSA > PANi, Table 4. The diffusion coefficient trend is following the trend that was

displayed by the band gaps. This implies that the diffusion coefficient is affected by the conductivity of the material.

Table 4: The diffusion coefficient and surface concentration of the polymers

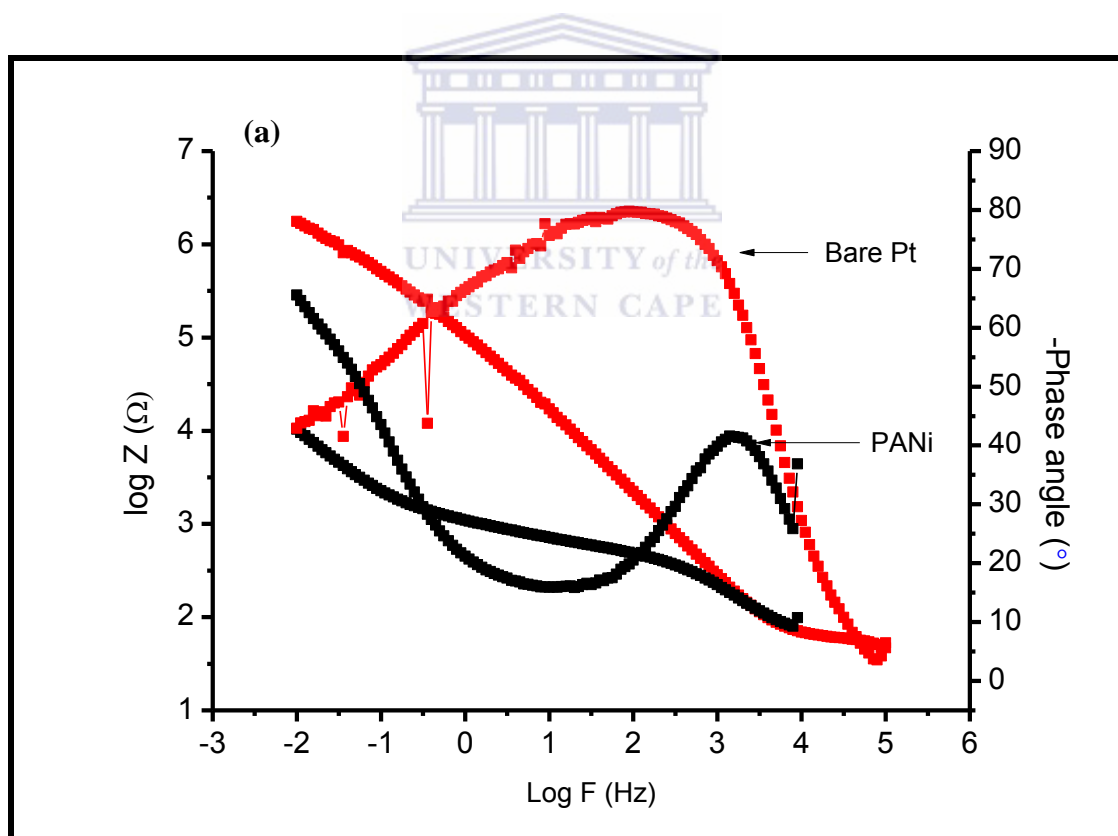
Surface	Γ ($\mu\text{mol cm}^{-2}$)	D ($\text{cm}^2 \text{s}^{-1}$)
PANi	18.5	3.97×10^{-19}
PANi-PSA	0.036	4.3×10^{-23}
POMA-PSA	0.061	1.13×10^{-21}
POMA-ASA	0.096	1.07×10^{-21}

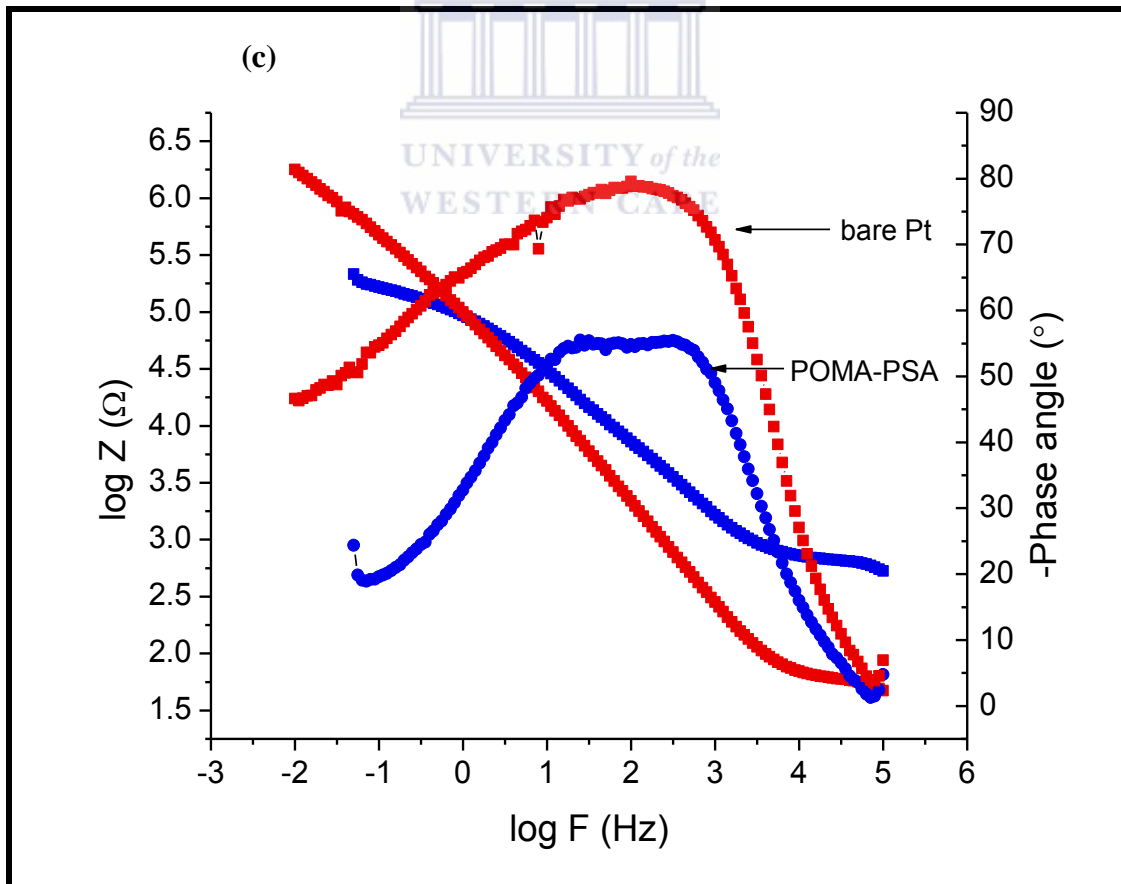
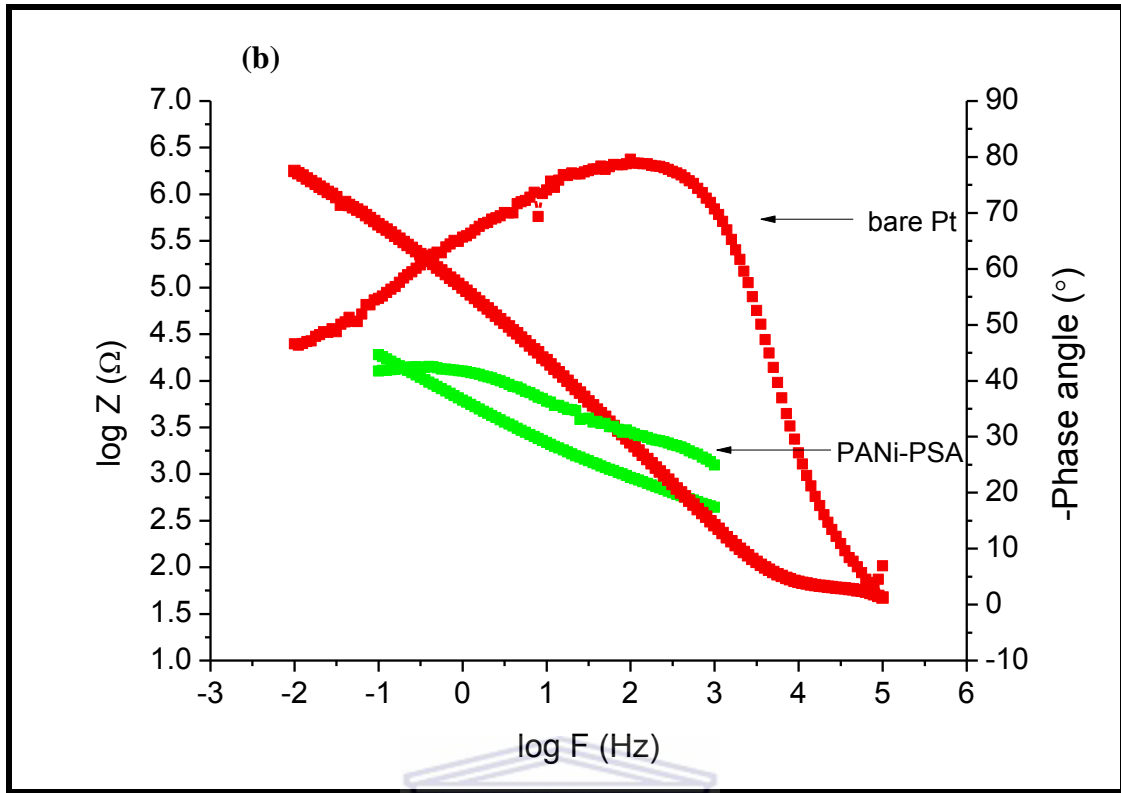
5.2 ELECTROCHEMICAL IMPEDANCE SPECTROSCOPY OF CONJUGATED POLYMERS

The electrochemical impedance analysis of the polymers was done using 1 M HCl as an electrolyte. Analysis of the EIS data can be done using Nyquist plots and Bode plots. The focus of this work is on analysis of the EIS data using Bode plots since with Bode plots frequency data is directly supplied.

The Bode plots are able to directly supply the phase angle data and the frequency. The value of the phase angle determines whether a compound is considered a conductor, semiconductor or an insulator. The increase in the capacitive effect is denoted by the increase in the value of the phase angle. The value of 90° denotes a pure capacitor. The phase angle maximum for bare platinum electrode is occurring at 76.5° and at a frequency of 436 Hz. The phase angle maximum for PANi is occurring at 42° and at a frequency of 1659 Hz. The phase angle maximum for the PANi-PSA is

occurring at 42° and at a frequency of 1.26 Hz. The phase angle maximum for the POMA-ASA is occurring at 39° and at a frequency of 245 Hz. The phase angle maximum for the POMA-PSA is occurring at 55° . The frequency at which the maxima of the phase angle is reached can be used to conclude the whether there is fast electron transfer or slow electron transfer. The data that was found can lead to the conclusion that there is relatively fast electron transfer that is occurring when PANi is used, since the capacitive effect maximum is only reached at relatively high frequencies in comparison with the other compounds. The sequence for the capacitive effect is decreasing in the following sequence bare platinum electrode > POMA-PSA > PANi-PSA = PANi > POMA-ASA.





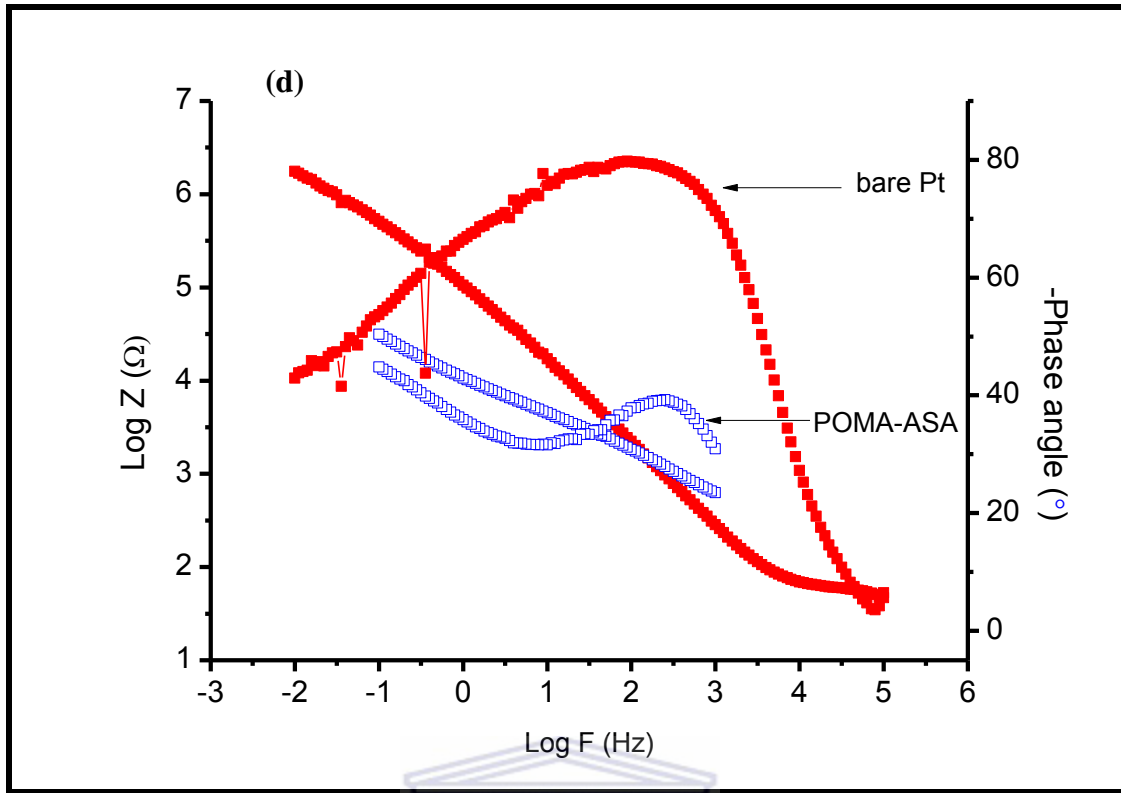


Figure 5.5: The Bode plots of a) PANi, b) PANi-PSA, c) POMA-PSA and d) POMA-ASA analysed using 1 M HCl

CHAPTER 6 : APPLICATION OF MATERIALS IN HYBRID PHOTOVOLTAIC CELLS

This chapter focuses on the study of the interaction of the polymers (donors) in the presence of PCBM (acceptor). The electronic spectra and photoluminescence are used as means to investigate the effect of the PCBM upon the spectra of the polymer donors. There is further investigation of the effect of the PCBM in the presence of the nanoparticle and polymers. The electronic and photoluminescence spectra are reported. The photovoltaic parameters are investigated for the different system (polymer/PCBM and polymer/nanoparticle/PCBM).

6.1 ELECTRONIC BEHAVIOUR OF THE CONJUGATED POLYMERS IN THE PRESENCE OF NANOPARTICLES AND PCBM IN SOLUTION

The importance of studying the electronic behaviour of the polymers (donors) in the presence of the PCBM (acceptor) is to determine whether the acceptor compound does not have adverse effect on the electronic behaviour of the compound. The adverse effects are the ones that lead to the degradation of the polymer.

6.1.1 Electronic Interaction between the Conjugated Polymers and PCBM

The electronic interaction of the conjugated polymers with the PCBM alone was studied in DMSO. The acceptor compound does not display electronic transitions within the scan range of 250 nm to 900 nm as observed in **Figure 6.1**. The ratio of the polymers (donors) to the PCBM (acceptor) that was used is 1:0.5 in DMSO. POMA-ASA is the one that is showing a level of instability in the presence of PCBM as an acceptor, using the previously stated ratio as shown in **Figure 6.1**. The instability is shown since the observed spectrum of the polymer alone in DMSO (Chapter 4) is not the same as the one observed in the presence of PCBM. The electronic absorption due to the transition from the π -bonding orbital to the π -antibonding orbital was still observed for the polymers at ~ 340 nm. The transition that is as a result of the charge transfer transitions between the quinoid moiety and the benzenoid moiety is occurring at ~ 600 nm for the polymers.

The presence of PCBM is supposed to induce the electron transfer from the polymer to the PCBM. As a result one would expect that there will be formation of polarons on the polymer backbone, this formation of polaron will induce the occurrence of electronic transitions that are observed at slightly lower energy levels. The transitions

were observed for the doped polymers alone in DMSO at ~425 nm. There is observation of an absorption peak at ~ 425 nm in the presence of PCBM, but it is not clearly defined. This indicates that there is charge transfer from the polymer to the PCBM. The poor definition may be as a result of aggregation in the presence of PCBM.

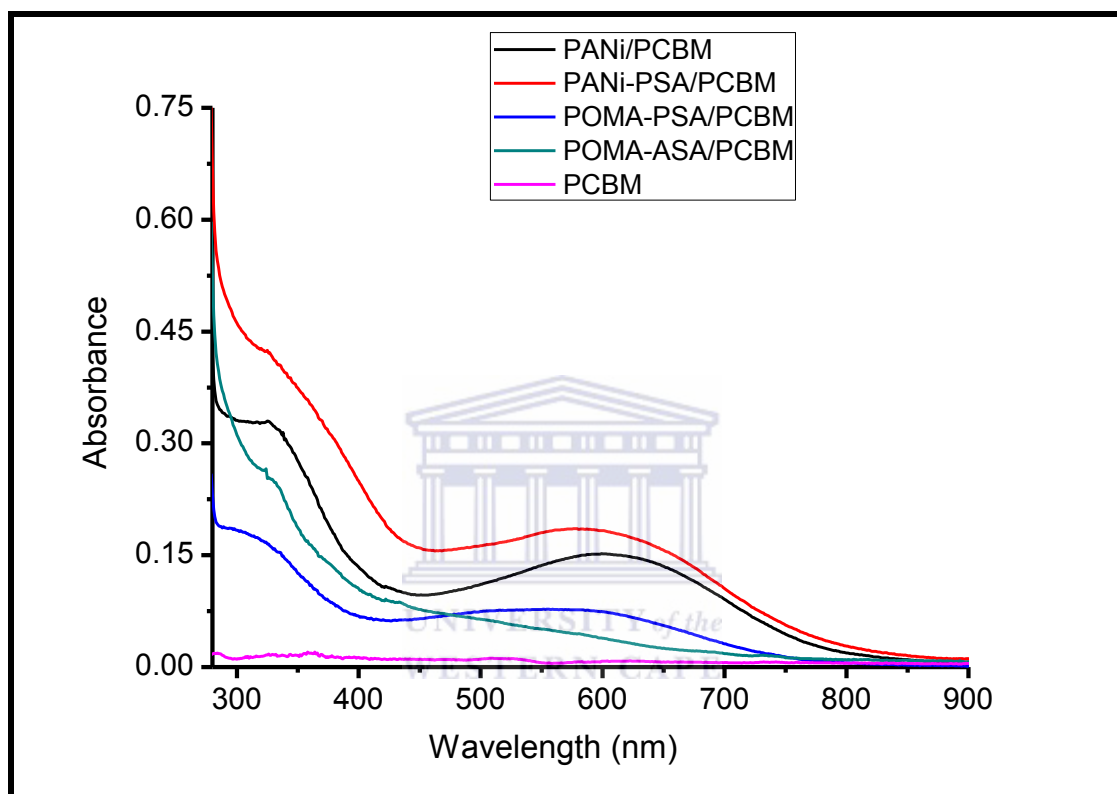


Figure 6.1: The electronic spectrum of the conjugated polymers in the presence of the PCBM (acceptor) in DMSO

6.1.2 Electronic Interaction between the Conjugated Polymers and Nanoparticles in the presence of PCBM

The wt ratio that was used is 1:1:0.5 in the interrogation of the interaction of the conjugated polymers in the presence of the nanoparticles and PCBM, **Figure 6.2**. There is observation of the characteristics due to the polymer and also the nanoparticles observed for PANi, PANi-PSA and POMA-PSA. The transitions due to the charge transfer from the quinoid moiety to the benzenoid moiety are observed at

~600 nm and there is prominence of the characteristic transitions due to the nanoparticles at the high energy wavelength. The POMA-ASA displays characteristics that show there is possible degradation of the polymer in the presence of the PCBM.

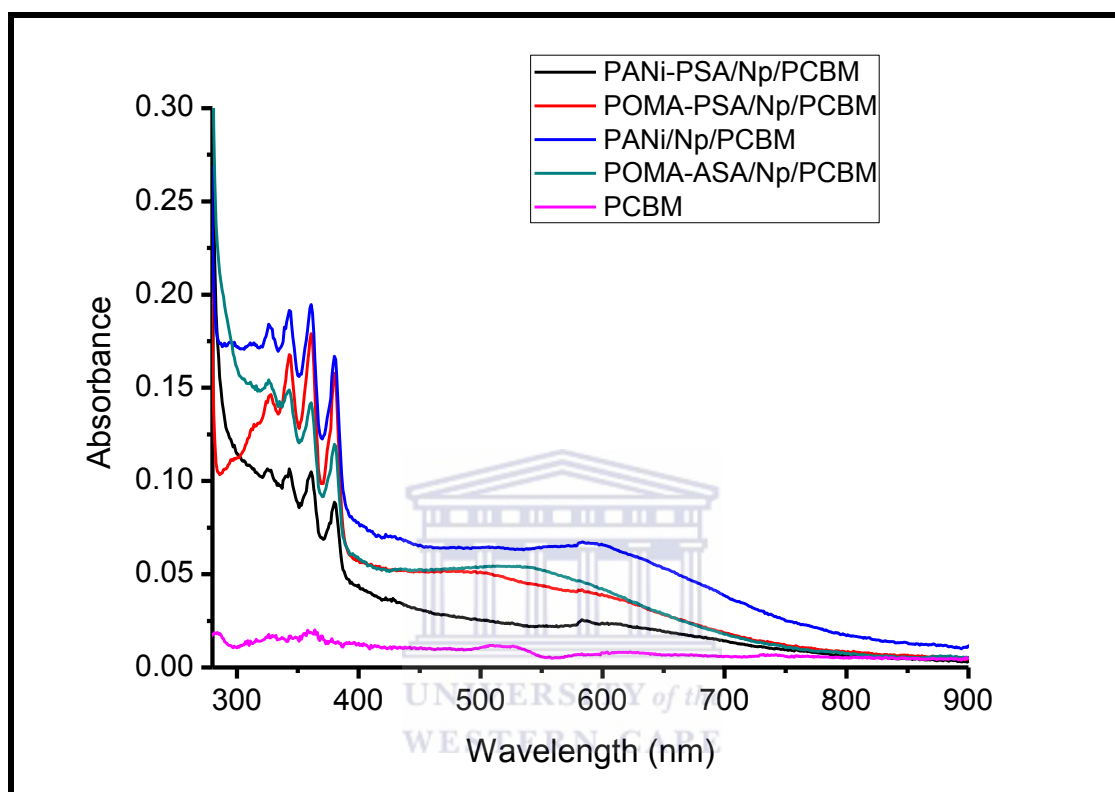


Figure 6.2: The electronic spectrum of the conjugated polymers in the presence of nanoparticles and PCBM (acceptor)

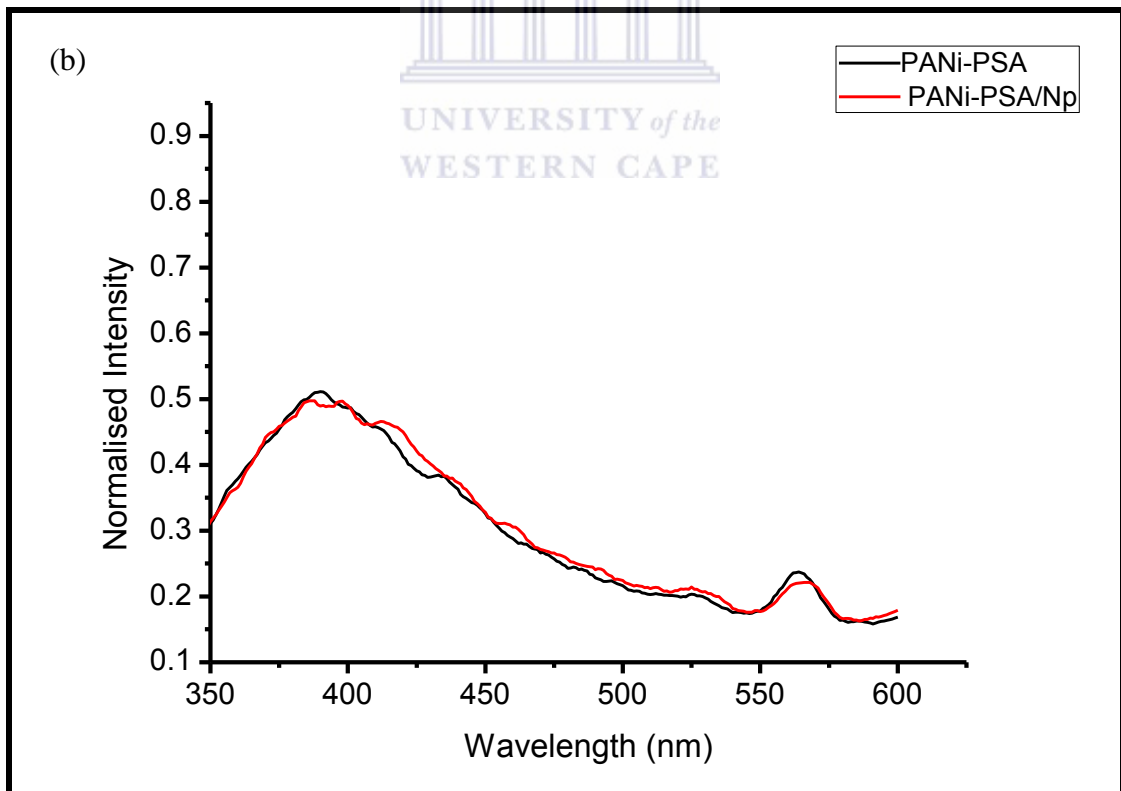
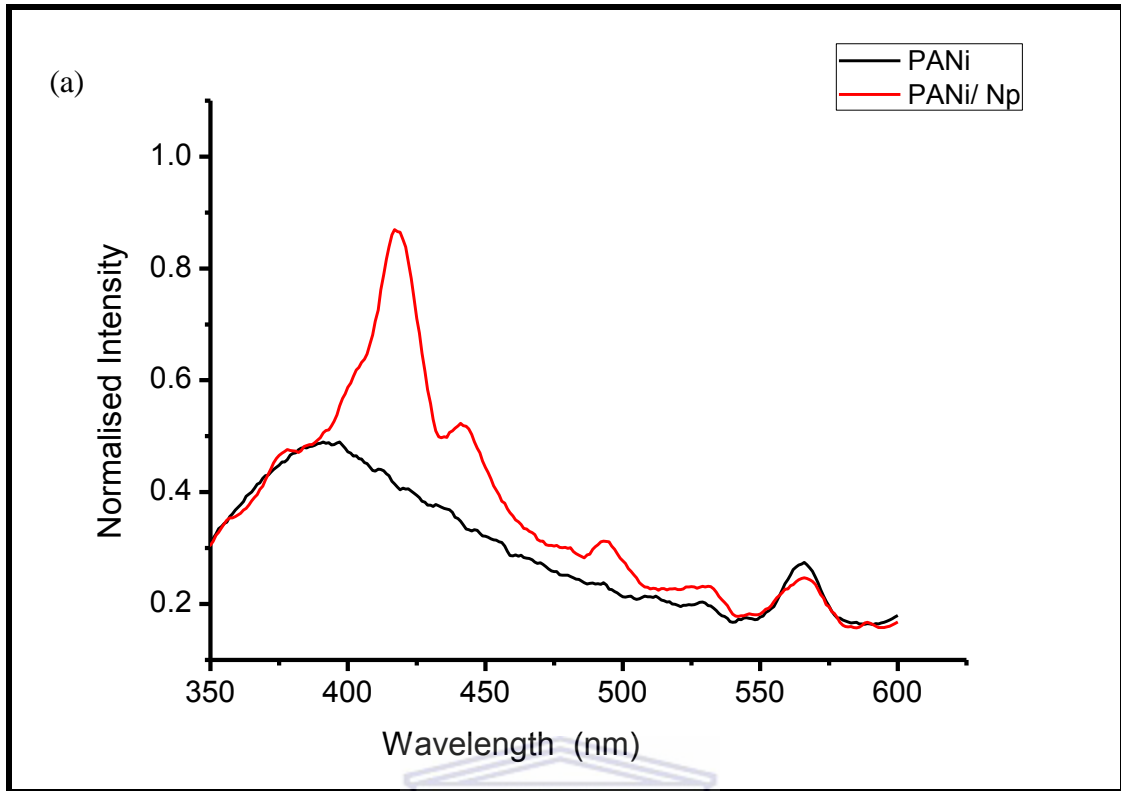
6.2 PHOTOLUMINESCENCE BEHAVIOUR OF THE COMPOUNDS ON ITO COATED GLASS

The photoluminescence behaviour of the conjugated polymers and nanoparticles was studied in solution in Chapter 4. It is important to look at the fluorescence behaviour of the compounds as a film since in photovoltaic cells the photoactive material forms a film on a chosen substrate. When the material are in its film, there is a high level of aggregation as a result there is a higher possibility of interaction between the polymer strands. The latter implies that there is a higher likelihood of experiencing

photoluminescence behaviour that is as a result of excimers in films. The study of the fluorescence behaviour of the polymers with the nanoparticles was done so as to verify whether there is quenching of the emission of the polymer which will be used as a donor in the photovoltaic cell by the nanoparticle which is a potential acceptor. It is important to develop potential acceptors since there is a smaller pool of acceptors that are used in photovoltaic cells.

6.1.1 Conjugated Polymers with Nanoparticles

The photoluminescence behaviour of the conjugated polymers alone and in the presence of the nanoparticles is depicted in **Figure 6.3**. The emission of the polymers alone on the ITO is such that there is observation of one wide peak that is due to the polymer emission at ~400 nm and the presence of an emission peak that is as a result of the ITO coated glass at ~600 nm. The observation of the latter emission is as a result of the thinness of the film that is formed on the substrate. The mixture of nanoparticles and polymers was done in a ratio of one is to one wt ratio. In the presence of the nanoparticles, there is observation of the emission due to both the polymer and nanoparticle without quenching of the emission. This characteristic makes the ZnGa_2O_4 nanoparticles not suitable as acceptors in photovoltaic cell technology.



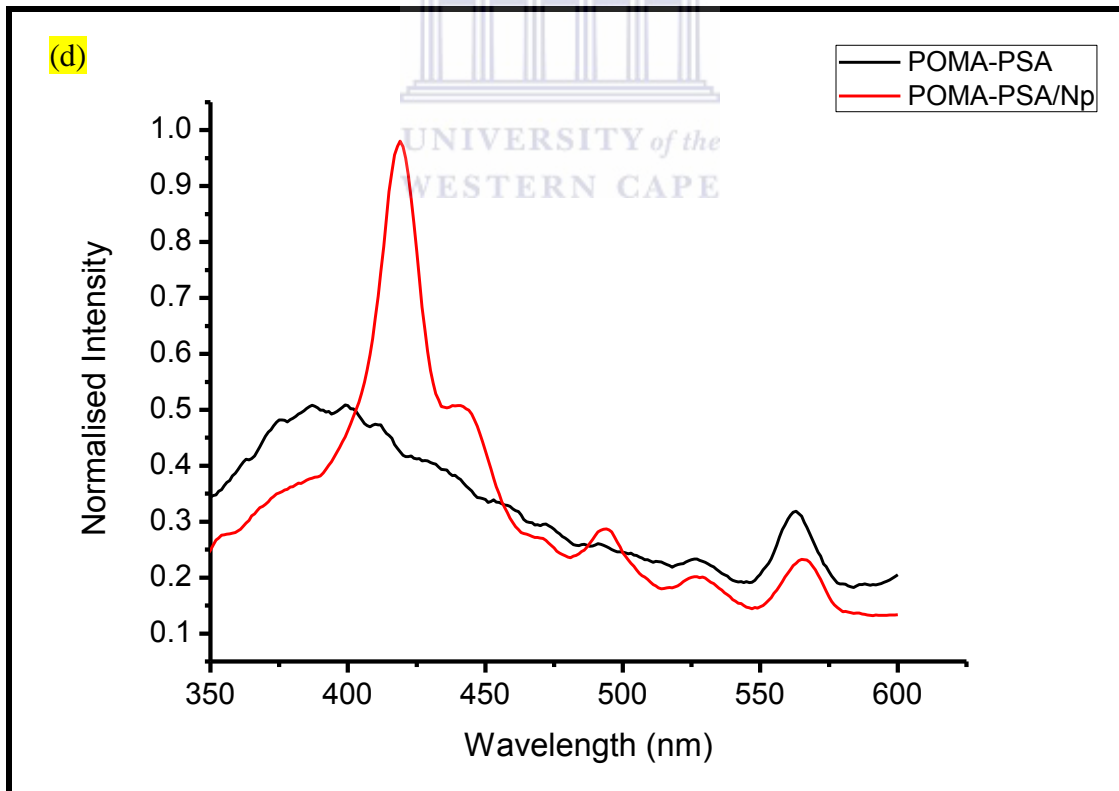
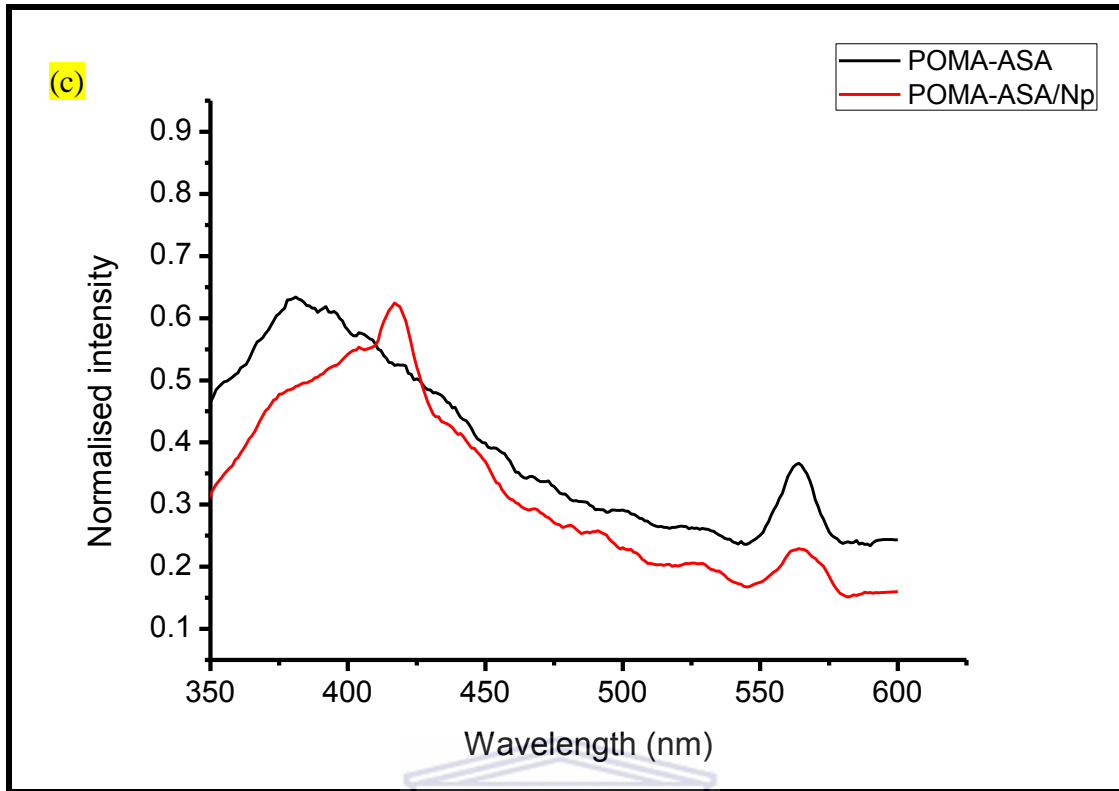


Figure 6.3: The photoluminescence behaviour of (a) PANi) PANi alone and PANi with nanoparticles ($ZnGa_2O_4$) (b) PANi-PSA alone and PANi-PSA with nanoparticles ($ZnGa_2O_4$) (c) POMA-ASA alone and POMA-ASA with nanoparticles ($ZnGa_2O_4$) (d) POMA-PSA alone and POMA-PSA with nanoparticles ($ZnGa_2O_4$) on ITO

6.1.2 Conjugated Polymers with PCBM on ITO

As previously stated the importance of looking at the interaction of the polymers (donors) and the PCM (acceptor), is to determine whether there is interaction of the donor and the acceptor at the excited level. This interaction is observed by the quenching of the fluorescence of the donor. The interaction was done using a 1:0.5 wt ratio. The mixture was spin coated on the ITO substrate before measurement. There is observation of the complete quenching of the fluorescence of the acceptor that is observed for all the polymers, **Figure 6.4**. This implies that there is charge dissociation that is occurring on the donor in the presence of PCBM as an acceptor [123]. This gives a potential system that can be used in photovoltaic cells.

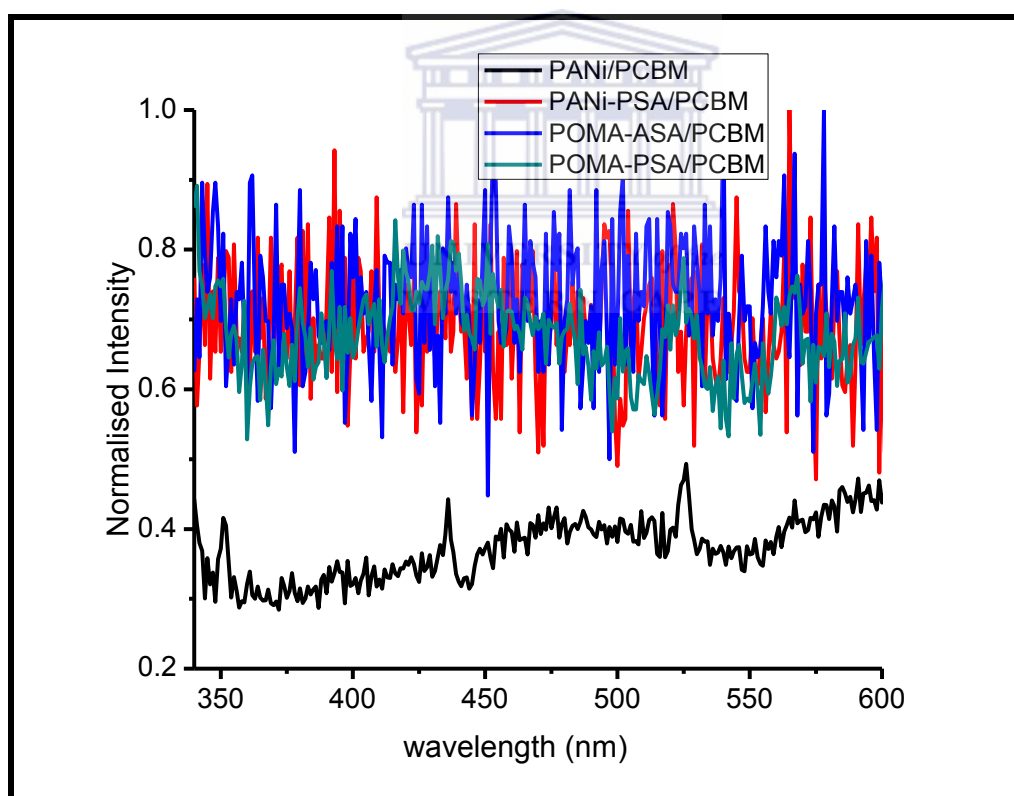


Figure 6.4: The photoluminescence behaviour of the polymers in the presence of PCBM

6.1.3 Conjugated Polymers with nanoparticles and PCBM on ITO

As observed in Section 6.1.1, the fluorescence of the polymer is not quenched by the nanoparticles, implying that the nanoparticles are incapable of being used as electron acceptors in this system. An experiment was done to observe whether the PCBM is able to act as an acceptor in the presence of the nanoparticles. The photoluminescence spectra that observed showed quenching of the emission due to the polymer and the nanoparticles, **Figure 6.5**. There is only observation of emission peaks due to the ITO substrate.

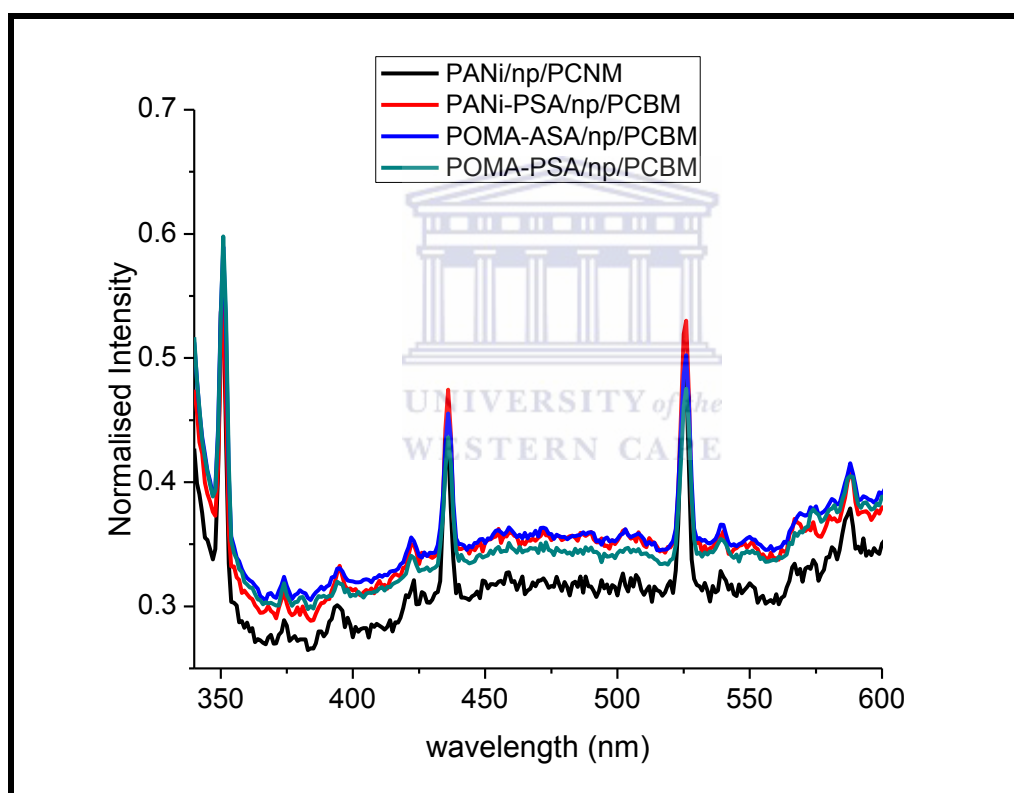


Figure 6.5: The photoluminescence response of the polymers in the presence of nanoparticles and PCBM

6.1.4 Photovoltaic behaviour of the Conjugated Polymers with PCBM as acceptor

As previously stated in Chapter 2, charge generation in organic solar cells involves the absorption of light by the donor, upon absorption an exciton is formed that is able

to dissociate into separate charge or recombine. The way in which to limit the degree of recombination is the use of an acceptor that has a lower HOMO level to the LUMO of the donor. This is the reason that PCBM is introduced as an acceptor in this case. The current-voltage (I-V) characteristics of the constructed photovoltaic cells were done and are denoted in **Figure 6.6**. The I-V curves are for the following devices ITO/PEDOT-PSS/PANi:PCBM/Ag, ITO/PEDOT-PSS/PANi-PSA:PCBM/Ag, ITO/PEDOT-PSS/POMA-PSA:PCBM/Ag and ITO/PEDOT-PSS/POMA-ASA:PCBM/Ag with a wt ratio of 1:1 between the donor (polymers) and acceptor (PCBM) under a simulated AM 1.5 illumination. The parameters that characterise a photovoltaic cell was calculated and is denoted in Table 6, overall the power conversion efficiency (η) values are much lower compared to the reported values of currently reported values for organic solar cells [25-26, 124], this can be accounted by the interconnected fibres that are formed and shown in SEM images. It has been reported [110] that the tubular form is more advantageous in the overall performance of the solar cell.

Photovoltaic cell that used PANi as a donor is the one that showed the best in terms of performance, with an efficiency of 4.62×10^{-6} %, V_{oc} of 4.8 mV, I_{sc} of 3.2 μ A and a FF of 0.296. This can be accounted under the basis that the PANi showed the highest level of crystallinity and conductivity compared to the other polymers. The former was demonstrated conclusively by XRD and TEM. There photovoltaic cell that used PANi-PSA as a donor showed a much lower level in the efficiency of the solar cell with an efficiency of 1.45×10^{-8} %. This is as a result of the lower conductivity and crystallinity. The POMA-PSA and POMA-ASA display much lower efficiencies in photovoltaic cells in comparison with the PANi and PANi-PSA. POMA-ASA has the

lowest values when looking at the photovoltaic parameters. This is following the trend in regards to crystallinity and conductivity, PANi > PANi-PSA > PANi-PSA > PANi-ASA. Another reason that can account for POMA-ASA's poor photovoltaic activity is that POMA-ASA seems to degrade in the presence of the PCBM; this is illustrated by the electronic spectrum of the POMA-ASA in the presence of the PCBM in Section 6.1.1.

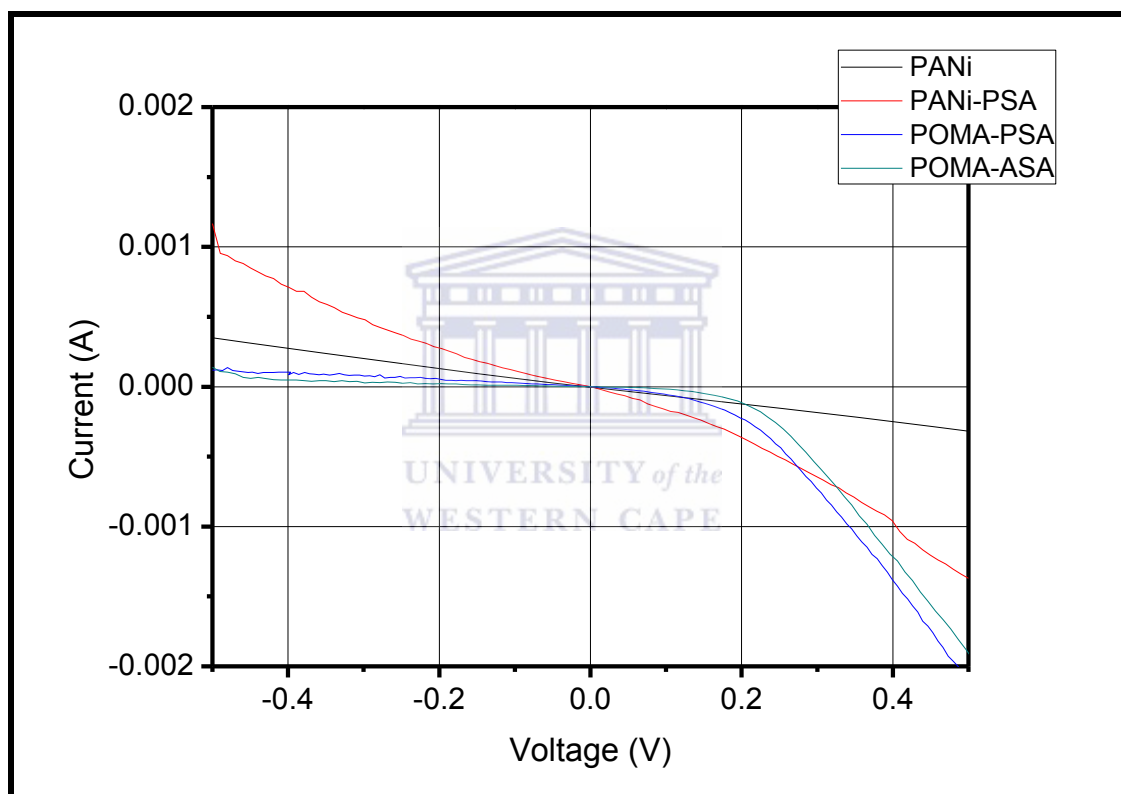


Figure 6.6: The I-V Curves of the photovoltaic cells under illumination

Table 5: The photovoltaic response of the polymers in the presence of PCBM as an acceptor under 1000 W cm⁻² Simulated Solar Irradiation

Polymer	V_{oc} (mV)	I_{sc} (μ A)	η (%)	FF
PANi	4.85	3.21	4.62×10^{-6}	0.296
PANi-PSA	1.45	0.239	8.13×10^{-8}	0.234
POMA-PSA	0.961	0.329	8.16×10^{-8}	0.257
POMA-ASA	0.234	0.233	1.085×10^{-8}	0.199

The photovoltaic parameters of the polymers with the ZnGa₂O₄ nanoparticles were investigated in the presence of PCBM as a donor. The current-voltage curves are illustrated in **Figure 6.7**. The overall response is very weak as can be seen by the fact that the intersection of the curve is very close to zero. This was confirmed by the values that were found for the photovoltaic parameters, the efficiency in power conversion is much lower in comparison with when the nanoparticles are not incorporated in the polymer. The data found is against the reported data that has been seen that there incorporation of nanoparticles such as zinc oxide leads to much higher efficiencies, Table 7. The negative effect may be as a result of the use of a gallium based nanoparticle which leads to the formation of nanoparticles that have a wide bandgap, hence a lower conductivity. The morphology of the nanoparticles that is displayed is spherical, which is not conducive in photovoltaic cells. Photovoltaic applications favour morphology that is tubular for the nanomaterials.

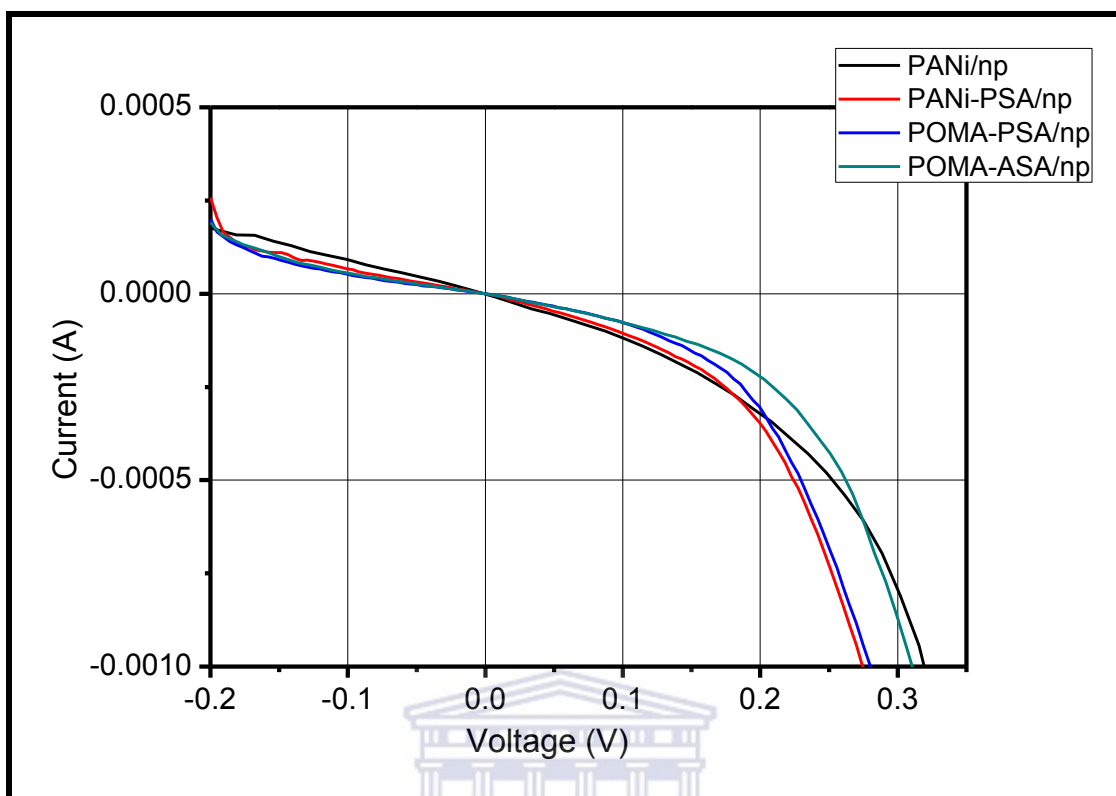


Figure 6.7: The I-V Curves of the photovoltaic cells under illumination

Table 6: The photovoltaic response of the polymers in the presence of PCBM as an acceptor under 1000 W cm^{-2} Simulated Solar Irradiation

Polymer	V_{oc} (mV)	I_{sc} (μA)	η (%)	FF
PANi-np	0.987	1.14	3.15×10^{-7}	0.28
PANi-PSA-np	0.654	0.515	1.13×10^{-7}	0.334
POMA-PSA-np	0.558	0.342	4.14×10^{-8}	0.217
POMA-ASA-np	0.0229	0.029	2.027×10^{-10}	0.306

CHAPTER 7 : CONCLUSIONS

Polymers that absorb in the visible region were synthesised. The polymeric materials were highly crystalline. Relationship between crystallinity and conductivity was displayed by the compounds. Conductivity and crystallinity increased in the following order, POMA-ASA < POMA-PSA < PANi-PSA < PANi. The PANi was the one that showed highest level of crystallinity and also a low energy band gap. The high level of crystallinity and band gap is as a result of the higher level of conjugation of the PANi in comparison with the other polymer derivatives. The dopants lower the level of conjugation and also the order in the folding process of the polymers. The emission of the polymers is quenched by the existence of excimers at the excited state of the polymers; this occurrence is propagated by the presence of the zinc gallate nanoparticles in solution. Reversible, single electron processes are observed for all the polymers. The diffusion coefficient is increasing with an increase in the surface concentration of the polymers on the electrode.

Generally the value of the efficiencies of the photovoltaic devices is low. This can be attributed to the morphology of the polymers that were synthesised. The morphology was not the desired nanorods that allow for higher produce higher efficiencies. The trend in the performance of the photovoltaic devices with the polymers alone with PCBM as an acceptor is the same as the one observed in the band gap, POMA-ASA < POMA-PSA < PANi-PSA < PANi. The observed trend was expected as it is anticipated that compounds that are highly conductive in organic solar cells, give the best response. The incorporation of the nanoparticles within the polymers lowered the

efficiency of the photovoltaic cell. Since the use of the bimetallic oxide increase the band gap, it seems to be advisable to make use of metal oxides that are composed of only one metal in order to lower the band gap, consequently increasing the conductivity of the compounds. Hence one recommendation for augmenting this work will be the use of metal oxides that are based on zinc and gallium, independently. The other recommendation is the investigation of the effect of different morphologies of the nanoparticles affect the overall performance of the zinc gallate as an electron acceptor.

The properties that are displayed by the polymers show that they can be useful in other areas besides photovoltaic application. The polymers display a highly fluorescent characteristic with good fluorescence quantum yield. This is an indication that they can be useful in the manufacturing of light emitting diodes. Since for light emitting diodes the requirement is that the compound must be a good fluorophore. An additional advantage is the ease of tailoring the polyaniline's conductivity by doping. This is a very attractive characteristic in the manufacture of electroluminescent devices for use in light emitting diodes. The luminescent properties of the polymers were not affected by the incorporation of the zinc gallate into the polymers when placed as a thin film on ITO glass. Instead there was a display of the luminescence behaviour of the polymer and the zinc gallate. Thus, it can be concluded that the polyaniline- zinc gallate composites can be used for electroluminescent devices. A synergistic effect may be demonstrated in the electroluminescence of the composite in comparison with the polymer alone.

The simplicity of tailoring the conductivity of the polyaniline derivatives by doping also makes it possible to use the polyaniline derivatives as electromagnetic radiation shields in the manufacturing of paints. This is due to the fact that the doping of the polymers can lead to polyaniline materials that have conductivity values that are close to those of the metals (aluminium and copper) that are used for electromagnetic shielding in the manufacturing of paints. The ease of processing of the polymeric materials is an additional factor that can lead to the polymers being able to find a niche in this area. There is also the thermal and environmental stability of the polymers that make them very attractive in this area.



CHAPTER 8 : REFERENCES

1. Razykov, T. M., C. S. Ferekides, D. Morel, E. Stefanakos, H. S. Ullal and H. M. Upadhyaya, *Solar photovoltaic electricity: Current status and future prospects*, Solar Energy, 2011.**85**:p. 1580-1608.
2. Kasap, S. O., *Optoelectronic and photonics: principles and practices*. 2001: Prentice Hall.340 pp.
3. Bernede, J. C., *Organic photovoltaic cells: history, principle and techniques*, Journal of the Chilean Chemical Society, 2008.**53**:p. 1549-1564.
4. Hamakawa, Y. In Proceedings of the First World Conference on Photovoltaic Energy Conversion. 1994. Hawaii,USA.
5. Peumans, P., A. Yakimov and S. R. Forrest, *Small molecular weight organic thin-film photodetectors and solar cells*, Journal of Applied Physics, 2003.**93**:p. 3693-3723.
6. Bhadra, S., D. Khastgir, N. K. Singha and J. H. Lee, *Progress in preparation, processing and applications of polyaniline*, Progress in Polymer Science, 2009.**34**:p. 783-810.
7. Metz, A., D. Adler, S. Bagus, H. Blanke, M. Bothar, E. Brouwer, S. Dauwe, K. Dressler, R. Droessler, T. Droste, M. Fiedler, Y. Gassenbauer, T. Grahl, N. Hermert, W. Kuzminski, A. Lachowicz, T. Lauinger, N. Lenck, M. Manole, M. Martini, R. Messmer, C. Meyer, J. Moschner, K. Ramspeck, P. Roth, R. Schoenfelder, B. Schum, J. Sticksel, K. Vaas, M. Volk and K. Wangemann, *Industrial high performance crystalline silicon solar cells and modules based on rear surface passivation technology*, Solar Energy Materials and Solar Cells, 2014.**120**:p. 417-425.

8. Mickey, C. D., *Solar Photovoltaic Cells*, Journal of Chemical Education, 1981.**58** (5):p. 418-423.
9. Yamaguchi, M., Y. Ohshita, K. Arafune, H. Sai and M. Tachibana, *Present status and future of crystalline silicon solar cells in Japan*, Solar Energy, 2006.**80**:p. 104-110.
10. Budiman, A. S., G. Illya, V. Handara, W. A. Caldwell, C. Bonelli, M. Kunz, N. Tamura and D. Verstraeten, *Enabling thin silicon technologies for next generation c-Si solar PV renewable energy systems using synchrotron X-ray microdiffraction as stress and crack mechanism probe*, Solar Energy Materials and Solar Cells, 2014.**130**:p. 303-308.
11. Bye, G. and B. Ceccaroli, *Solar grade silicon: Technology status and industrial trends*, Solar Energy Materials and Solar Cells, 2014.**130**:p. 634-646.
12. Chen, S., T. Jarmar, S. Soedergren, U. Malm, E. Wallin, O. Lundberg, S. Jander, R. Hunger and L. Stolt, *Light soaking induced doping increase and sodium redistribution in Cu(In,Ga)Se₂-based thin film solar cells*, Thin Solid Films, 2014,p. Ahead of Print.
13. Banerjee, C., T. Srikanth, U. Basavaraju, R. M. Tomy, M. G. Sreenivasan, K. Mohanchandran, S. Mukhopadhyay and A. K. Barua, *Development of n- μ c-SiO_x:H as cost effective back reflector and its application to thin film amorphous silicon solar cells*, Solar Energy, 2013.**97**:p. 591-595.
14. Johnson, F., S. H. Song, J. Abrahamson, R. Liptak, E. Aydil and S. A. Campbell, *Sputtered metal oxide broken gap junctions for tandem solar cells*, Solar Energy Materials and Solar Cells, 2014,p. Ahead of Print.
15. Kitai, A., *Principles of solar cells, LEDs and diodes: the role of the PN junction*. 2011: Wiley.334 pp.

16. Green, M. A., *Crystalline silicon photovoltaic cells*, *Advanced Materials*, 2001.**13**:p. 1019-1022.
17. Stuckelberger, M., Y. Riesen, M. Despeisse, J. W. Schuttauf, F. J. Haug and C. Ballif, *Light-induced Voc increase and decrease in high-efficiency amorphous silicon solar cells*, *Journal of Applied Physics*, 2014.**116**:p. 094503/094501-094503/094512.
18. Lim, J. W., M. Shin, D. J. Lee, S. H. Lee and S. J. Yun, *Highly transparent amorphous silicon solar cells fabricated using thin absorber and high-bandgap-energy n/i-interface layers*, *Solar Energy Materials and Solar Cells*, 2014.**128**:p. 301-306.
19. Xue, C. and X. Sun, *Design for amorphous silicon solar cells*, *Advances in Materials Research*, 2013.**750-752**:p. 961-964, 965 pp.
20. Goetzberger, A., C. Hebling and H.-W. Schock, *Photovoltaic materials, history, status and outlook*, *Materials Science and Engineering Reports*, 2003.**R40**:p. 1-46.
21. Li, L., N. Coates and D. Moses, *Solution-processed inorganic solar cell based on in situ synthesis and film deposition of CuInS₂ nanocrystals*, *Journal of the American Chemical Society*, 2010.**132**:p. 22-23.
22. Levy-Clement, C., R. Tena-Zaera, M. A. Ryan, A. Katty and G. Hodes, *CdSe-sensitized p-CuSCN/Nanowire n-ZnO heterojunctions*, *Advanced Materials*, 2005.**17**:p. 1512-1515.
23. Chang, F. F., H. H. Lin, H. C. Lin, C. H. Hsieh and T. Z. Li. *Photovoltaic cell structure*. 2010. US20100243044A1.
24. Gomez, R. and J. L. Segura. *Materials for organic solar cells*. 2008. American Scientific Publishers.
25. Zhang, C., *Study of organic solar cells conversion efficiency*, *Advances in Materials Research*, 2014.**950**:p. 150-154, 156.

26. Satoru, I., *Energy conversion efficiency in exciton process for single and bulk heterojunction organic solar cells*, Japanese Journal of Applied Physics, 2008.**47** (12R):p. 8859.
27. Guenes, S., H. Neugebauer and N. S. Sariciftci, *Conjugated polymer-based organic solar cells*, Chemical Reviews, 2007.**107**:p. 1324-1338.
28. Hoppe, H. and N. S. Sariciftci, *Organic solar cells: an overview*, Journal of Materials Research, 2004.**19** (07):p. 1924-1945.
29. Leventis, H. C., S. P. King, A. Sudlow, M. S. Hill, K. C. Molloy and S. A. Haque, *Nanostructured hybrid polymer-inorganic solar cell active layers formed by controllable in situ growth of semiconducting sulfide networks*, Nano Letters, 2010.**10**:p. 1253-1258.
30. Singh, V. K., R. K. Kanaparthi and L. Giribabu, *Emerging molecular design strategies of unsymmetrical phthalocyanines for dye-sensitized solar cell applications*, RSC Advances, 2014.**4**:p. 6970-6984.
31. Kietzke, T., *Recent advances in organic solar cells*, Advances in OptoElectronics, 2007.p. 40285/40281-40285/40215.
32. Yan, J. and B. R. Saunders, *Third-generation solar cells: a review and comparison of polymer:fullerene, hybrid polymer and perovskite solar cells*, RSC Advances, 2014.**4**:p. 43286-43314.
33. Jose, R., V. Thavasi and S. Ramakrishna, *Metal oxides for dye-sensitized solar cells*, Journal of the American Ceramic Society, 2009.**92**:p. 289-301.
34. Beek, W. J. E., M. M. Wienk and R. A. J. Janssen. *Metal oxide-polymer bulk heterojunction solar cells*. 2008. Wiley-VCH Verlag GmbH & Co. KGaA.
35. Wang, W. and E. A. Schiff, *Polyaniline on crystalline silicon heterojunction solar cells*, Applied Physics Letters, 2007.**91**:p. 133504/133501-133504/133503.

36. Sun, H., Y. Luo, Y. Zhang, D. Li, Z. Yu, K. Li and Q. Meng, *In situ preparation of a flexible polyaniline/carbon composite counter electrode and its application in dye-sensitized solar cells*, Journal of Physical Chemistry C, 2010.**114**:p. 11673-11679.
37. Singh, S., R. S. Deol, M. L. Singla and D. V. S. Jain, *Light harvesting efficiency of hybrid nano-composite for photovoltaic application*, Solar Energy Materials and Solar Cells, 2014.**128**:p. 231-239.
38. Bolisetty, S., J. Adamcik, J. Heier and R. Mezzenga, *Amyloid directed synthesis of titanium dioxide nanowires and their applications in hybrid photovoltaic devices*, Advanced Functional Materials, 2012.**22**:p. 3424-3428.
39. Oku, T., A. Takeda, A. Nagata, K. Fujimoto, T. Akiyama and A. Suzuki, *Microstructures and photovoltaic properties of fullerene-based organic-inorganic hybrid solar cells*, Journal of Physics: Conference Series, 2012.**352**:p. 012024/012021-012024/012029.
40. He, Y. and Y. Li, *Fullerene derivative acceptors for high performance polymer solar cells*, Physical Chemistry Chemical Physics, 2011.**13**:p. 1970-1983.
41. Horowitz, G., F. Deloffre, F. Garnier, R. Hajlaoui, M. Hmyene and A. Yassar, *All-organic field-effect transistors made of π -conjugated oligomers and polymeric insulators*, Synthetic Metals, 1993.**54** (1-3):p. 435-445.
42. Dimitrakopoulos, C. D., B. K. Furman, T. Graham, S. Hegde and S. Purushothaman, *Field-effect transistors comprising molecular beam deposited α,ω -dihexyl-hexathienylene and polymeric insulator*, Synthetic Metals, 1998.**92** (1):p. 47-52.
43. Ren, S., N. Zhao, S. C. Crawford, M. Tambe, V. Bulovic and S. Gradecak, *Heterojunction photovoltaics using GaAs nanowires and conjugated polymers*, Nano Lett, 2011.**11**:p. 408-413.

44. Wang, X., K. Maeda, X. Chen, K. Takanabe, K. Domen, Y. Hou, X. Fu and M. Antonietti, *Polymer semiconductors for artificial photosynthesis: hydrogen evolution by mesoporous graphitic carbon nitride with visible light*, Journal of the American Chemical Society, 2009.**131** (5):p. 1680-1681.
45. Morteani, A. C., P. Sreearunothai, L. M. Herz, R. H. Friend and C. Silva, *Exciton regeneration at polymeric semiconductor heterojunctions*, Physical Review Letters, 2004.**92** (24):p. 247402.
46. Choi, M.-C., Y. Kim and C.-S. Ha, *Polymers for flexible displays: From material selection to device applications*, Progress in Polymer Science, 2008.**33**:p. 581-630.
47. Dhand, C., M. Das, M. Datta and B. D. Malhotra, *Recent advances in polyaniline based biosensors*, Biosensors and Bioelectronics, 2011.**26**:p. 2811-2821.
48. Hu, Z. A., L. J. Ren, X. J. Feng, Y. P. Wang, Y. Y. Yang, J. Shi, L. P. Mo and Z. Q. Lei, *Platinum-modified polyaniline/polysulfone composite film electrodes and their electrocatalytic activity for methanol oxidation*, Electrochemistry Communications, 2006.**9**:p. 97-102.
49. Holze, R., *G. Inzelt: Conducting polymers*, Journal of Applied Electrochemistry, 2009.**39** (6):p. 953-954.
50. van der Zanden, B., A. Goossens and J. Schoonman, *Photodoping of PPV/TiO₂ solar cells*, Synthetic Metals, 2001.**121**:p. 1601-1602.
51. Vats, T., S. N. Sharma, M. Kumar, M. Kar, K. Jain, V. N. Singh, B. R. Mehta and A. K. Narula, *Comparison of photostability, optical and structural properties of TiO₂/conjugated polymer hybrid composites prepared via different methods*, Thin Solid Films, 2011.**519**:p. 1100-1105.
52. Nan, Y.-X., F. Chen, L.-G. Yang, X.-X. Jiang, L.-J. Zuo, J.-L. Zhang, Q.-X. Yan, M.-M. Shi and H.-Z. Chen, *Photoluminescence enhancement and atmosphere-*

dependent photovoltaic performance in CdS nanorod arrays/MEH-PPV hybrid, Solar Energy Materials and Solar Cells, 2011.**95**:p. 3233-3240.

53. Bi, D., F. Wu, W. Yue, Q. Qu, Q. Cui, Z. Qiu, C. Liu, W. Shen and M. Wang, *Improved performance of MEH-PPV/ZnO solar cells by addition of lithium salt*, Solar Energy, 2011.**85**:p. 2819-2825.

54. Yang, X. and A. Uddin, *Effect of thermal annealing on P3HT:PCBM bulk-heterojunction organic solar cells: A critical review*, Renewable Sustainable Energy Rev., 2014.**30**:p. 324-336.

55. Mingeback, M., S. Walter, V. Dyakonov and C. Deibel, *Direct and charge transfer state mediated photogeneration in polymer-fullerene bulk heterojunction solar cells*, Applied Physics Letters, 2012.**100**:p. 193302/193301-193302/193304.

56. Khlyabich, P. P., B. Burkhart, A. E. Rudenko and B. C. Thompson, *Optimization and simplification of polymer-fullerene solar cells through polymer and active layer design*, Polymer, 2013.**54**:p. 5267-5298.

57. Tan, F., S. Qu, J. Wu, Z. Wang, L. Jin, Y. Bi, J. Cao, K. Liu, J. Zhang and Z. Wang, *Electrodeposited polyaniline films decorated with nano-islands: Characterization and application as anode buffer layers in solar cells*, Solar Energy Materials and Solar Cells, 2011.**95**:p. 440-445.

58. Lee, K., S. Cho, S. H. Park, A. J. Heeger, C.-W. Lee and S.-H. Lee, *Metallic transport in polyaniline*, Nature, 2006.**441**:p. 65-68.

59. Li, D., J. Huang and R. B. Kaner, *Polyaniline nanofibers: a unique polymer nanostructure for versatile applications*, Accounts of Chemical Research, 2009.**42**:p. 135-145.

60. Upadhyay, P. K. and A. Ahmad, *Chemical synthesis, spectral characterization and stability of some electrically conducting polymers*, Chinese Journal of Polymer Science, 2010.**28**:p. 191-197.
61. Mavundla, S. E., G. F. Malgas, P. Baker and E. I. Iwuoha, *Synthesis and characterization of novel nanophase hexagonal poly(2,5-dimethoxyaniline)*, Electroanalysis, 2008.**20**:p. 2347-2353.
62. Mathebe, N. G. R., A. Morrin and E. I. Iwuoha, *Electrochemistry and scanning electron microscopy of polyaniline/peroxidase-based biosensor*, Talanta, 2004.**64**:p. 115-120.
63. Iwuoha, E. I., D. S. De Villaverde, N. P. Garcia, M. R. Smyth and J. M. Pingarron, *Reactivities of organic phase biosensors. 2. The amperometric behavior of horseradish peroxidase immobilized on a platinum electrode modified with an electrosynthetic polyaniline film*, Biosensors and Bioelectronics, 1997.**12**:p. 749-761.
64. Dadashi-Silab, S., H. Bildirir, R. Dawson, A. Thomas and Y. Yagci, *Microporous thioxanthone polymers as heterogeneous photoinitiators for visible light induced free radical and cationic polymerizations*, Macromolecules, 2014.**47**:p. 4607-4614.
65. Morris, J. C., S. Telitel, K. Fairfull-Smith, S. Bottle, J. Lalevee, J.-I. Clement, Y. Guillaneuf and D. Gimes, *Novel polymer synthesis methodologies using combinations of thermally- and photochemically-induced nitroxide mediated polymerization*, Polymer Chemistry, 2014.p. Ahead of Print.
66. Spring, A. M., C.-Y. Yu, M. Horie and M. L. Turner, *MEH-PPV by microwave assisted ring-opening metathesis polymerisation*, Chemical Communications, 2009.p. 2676-2678.

67. Lidster, B. J., J. M. Behrendt and M. L. Turner, *Monotelechelic poly(p-phenylenevinylene)s by ring opening metathesis polymerisation*, Chemical Communications, 2014.**50**:p. 11867-11870.
68. Koparkar, K. A., *Plasma polymerized thin film sensor: synthesis and application*, Sensors and Transducers Journal, 2012.**143**:p. 10-31.
69. Zhao, X.-Y., M.-z. Wang, Z. Wang and B.-z. Zhang, *Structural and dielectric properties of conjugated polynitrile thin films deposited by plasma polymerization*, Thin Solid Films, 2008.**516**:p. 8272-8277.
70. Liu, W., R. Tkachov, H. Komber, V. Senkovskyy, M. Schubert, Z. Wei, A. Facchetti, D. Neher and A. Kiriya, *Chain-growth polycondensation of perylene diimide-based copolymers: a new route to regio-regular perylene diimide-based acceptors for all-polymer solar cells and n-type transistors*, Polymer Chemistry, 2014.**5**:p. 3404-3411.
71. Verswyvel, M., P. Verstappen, L. De Cremer, T. Verbiest and G. Koeckelberghs, *The quest for a universal controlled chain-growth polymerization protocol: toward a variety of all-conjugated block-copolymers*, Polym. Prepr., 2011.**52**:p. 989-990.
72. Aydogan, B., A. S. Gundogan, T. Ozturk and Y. Yagci, *Polythiophene derivatives by step-growth polymerization via photoinduced electron transfer reactions*, Chemical Communications, 2009.p. 6300-6302.
73. Ruckenstein, E., *Concentrated emulsion polymerization*, *Polymer Synthesis/Polymer Catalysis*, 1997, Springer Berlin Heidelberg. p. 1-58.
74. Lee, K.-R., Y.-J. Yu, S.-H. Joo, C.-Y. Lee, D. H. Choi, J. S. Joo, Y.-S. Park and J.-I. Jin, *Poly(2,5-thienylene vinylene) in nano shapes by CVD polymerization*, Macromolecular Rapid Communications, 2007.**28**:p. 1057-1061.

75. Inayama, S., Y. Tatewaki and S. Okada, *Solid-state polymerization of conjugated hexayne derivatives with different end groups*, Polym J, 2010.**42** (3):p. 201-207.
76. Gomes, E. C. and M. A. S. Oliveira, *Chemical polymerization of aniline in hydrochloric acid (HCl) and formic acid (HCOOH) media. Differences between the two synthesized polyanilines*, American Journal of Polymer Science, 2012.**2**:p. 5-13, 19 pp.
77. Zhu, S., X. Chen, Y. Gou, Z. Zhou, M. Jiang, J. Lu and D. Hui, *Synthesis and mechanism of polyaniline nanotubes with rectangular cross section via in situ polymerization*, Polymers for Advanced Technologies, 2012.**23**:p. 796-802.
78. Eisa, W. H., M. F. Zayed, Y. K. Abdel-Moneam and A. M. Abou Zeid, *Water-soluble gold/polyaniline core/shell nanocomposite: Synthesis and characterization*, Synthetic Metals, 2014.**195**:p. 23-28.
79. Cao, Y., J. Qiu and P. Smith, *Effect of solvents and co-solvents on the processibility of polyaniline: I. Solubility and conductivity studies*, Synthetic Metals, 1995.**69**:p. 187-190.
80. Facchetti, A., *π -Conjugated polymers for organic electronics and photovoltaic cell applications*, Chemistry of Materials, 2011.**23**:p. 733-758.
81. Salaneck, W. R., R. H. Friend and J. L. Bredas, *Electronic structure of conjugated polymers: consequences of electron-lattice coupling*, Physics Reports, 1999.**319**:p. 231-251.
82. Patil, A. O., A. J. Heeger and F. Wudl, *Optical properties of conducting polymers*, Chemical Reviews, 1988.**88**:p. 183-200.
83. Huang, J. and M. Wan, *Polyaniline doped with different sulfonic acids by in situ doping polymerization*, Journal of Polymer Science Part A: Polymer Chemistry, 1999.**37** (9):p. 1277-1284.

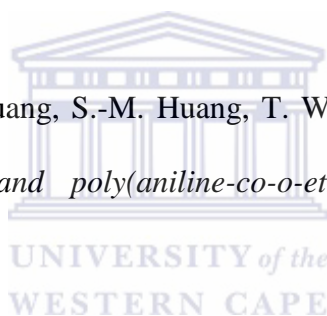
84. Han, Y.-G., T. Kusunose and T. Sekino, *One-step reverse micelle polymerization of organic dispersible polyaniline nanoparticles*, *Synthetic Metals*, 2009.**159**:p. 123-131.
85. Dai, L., *Conjugated and fullerene-containing polymers for electronic and photonic applications: advanced syntheses and microlithographic fabrications*, *Journal of Macromolecular Science - Reviews in Macromolecular Chemistry and Physics*, 1999.**C39**:p. 273-387.
86. Ozdemir, C., H. K. Can, N. Colak and A. Guner, *Synthesis, characterization, and comparison of self-doped, doped, and undoped forms of polyaniline, poly(o-anisidine), and poly[aniline-co-(o-anisidine)]*, *Journal of Applied Polymer Science*, 2006.**99**:p. 2182-2192.
87. Petrova, J. N., J. R. Romanova, G. K. Madjarova, A. N. Ivanova and A. V. Tadjer, *Fully doped oligomers of emeraldine salt: polaronic versus bipolaronic configuration*, *Journal of Physical Chemistry B*, 2011.**115**:p. 3765-3776.
88. Lakowicz, J., R.ed. *Topics in fluorescence spectroscopy: principles*. Vol 2. 2002, Kluwer Academic Publishers. New York. 1-429.
89. Badaeva, E., M. R. Harpham, R. Guda, O. Suzer, C.-Q. Ma, P. Bauerle, T. Goodson and S. Tretiak, *Excited-state structure of oligothiophene dendrimers: computational and experimental study*, *Journal of Physical Chemistry B*, 2010.**114**:p. 15808-15817.
90. Jenekhe, S. A. and J. A. Osaheni, *Excimers and exciplexes of conjugated polymers*, 1994, Rochester Univ. p. 32.
91. Barbour, L. W., M. Hegadorn and J. B. Asbury, *Watching electrons move in real time: ultrafast infrared spectroscopy of a polymer blend photovoltaic material*, *Journal of the American Chemical Society*, 2007.**129**:p. 15884-15894.

92. Adebolu, O., C. E. Bonner, Jr., C. Zhang and S. Sun, *Emission dynamics of donor and acceptor substituted PPV for photovoltaic applications*, Polymeric Preprints (American Chemical Society, Division of Polymer Chemistry), 2006.**47**:p. 132.
93. Dai, L., J. Lu, B. Matthews and A. W. H. Mau, *Doping of conducting polymers by sulfonated fullerene derivatives and dendrimers*, Journal of Physical Chemistry B, 1998.**102**:p. 4049-4053.
94. Zhou, C., J. Kong and H. Dai, *Intrinsic Electrical Properties of Individual Single-Walled Carbon Nanotubes with Small Band Gaps*, Physical Review Letters, 2000.**84**:p. 5604-5607.
95. Ohsawa, Y. and T. Saji, *Electrochemical detection of C606- at low temperature*, Journal of the Chemical Society, Chemical Communications, 1992.p. 781-782.
96. Bi, D., F. Wu, W. Yue, Y. Guo, W. Shen, R. Peng, H. Wu, X. Wang and M. Wang, *Device performance correlated with structural properties of vertically aligned nanorod arrays in polymer/ZnO solar cells*, Journal of Physical Chemistry C, 2010.**114**:p. 13846-13852.
97. James, L. W., H. A. VanderPlas and R. L. Moon, *High performance gallium arsenide photovoltaic cells for concentrator applications*, 1977, Varian Assoc. p. 87
98. Blokhin, S. A., A. V. Sakharov, A. M. Nadtochy, A. S. Pauysov, M. V. Maximov, N. N. Ledentsov, A. R. Kovsh, S. S. Mikhrin, V. M. Lantratov, S. A. Mintairov, N. A. Kaluzhniy and M. Z. Shvarts, *AlGaAs/GaAs photovoltaic cells with an array of InGaAs QDs*, Semiconductors, 2009.**43**:p. 514-518.
99. Lee, S. B., J. H. Beak, B. h. Kang, K.-Y. Dong, Y.-Y. Yu, Y. Doo Lee and B.-K. Ju, *The annealing effects of tungsten oxide interlayer based on organic photovoltaic cells*, Solar Energy Materials and Solar Cells, 2013.**117**:p. 203-208.

100. Holt, J. M., A. J. Ferguson, N. Kopidakis, B. A. Larsen, J. Bult, G. Rumbles and J. L. Blackburn, *Prolonging charge separation in P3HT-SWNT composites using highly enriched semiconducting nanotubes*, Nano Letters, 2010.**10**:p. 4627-4633.
101. Flavin, K., K. Lawrence, J. Bartelmess, M. Tasior, C. Navio, C. Bittencourt, D. F. O'Shea, D. M. Guldi and S. Giordani, *Synthesis and characterization of boron azadipyrromethene single-wall carbon nanotube electron donor-acceptor conjugates*, ACS Nano, 2011.**5**:p. 1198-1206.
102. Fukai, Y., Y. Kondo, S. Mori and E. Suzuki, *Highly Efficient Dye-Sensitized SnO₂ Solar Cells having Sufficient Electron Diffusion Length*, Electrochemistry Communications, 2007.**9**:p. 1439-1443.
103. Ghosh, A. K. and T. Feng, *Rectification, space-charge-limited current, photovoltaic, and photoconductive properties of aluminum/tetracene/gold sandwich cell*, Journal of Applied Physics, 1973.**44**:p. 2781-2788.
104. Sariciftci, N. S., D. Braun, C. Zhang, V. I. Srdanov, A. J. Heeger, G. Stucky and F. Wudl, *Semiconducting polymer-buckminsterfullerene heterojunctions: diodes, photodiodes, and photovoltaic cells*, Applied Physics Letters, 1993.**62**:p. 585-587.
105. Halls, J. J. M., C. A. Walsh, N. C. Greenham, E. A. Marseglia, R. H. Friend, S. C. Moratti and A. B. Holmes, *Efficient photodiodes from interpenetrating polymer networks*, Nature, 1995.**376**:p. 498-500.
106. Yu, G., J. Gao, J. C. Hummelen, F. Wudl and A. J. Heeger, *Polymer photovoltaic cells: enhanced efficiencies via a network of internal donor-acceptor heterojunctions*, Science, 1995.**270**:p. 1789-1791.
107. Saunders, B. R. and M. L. Turner, *Nanoparticle-polymer photovoltaic cells*, Advances in Colloid and Interface Science, 2008.**138**:p. 1-23.

108. Gu, D., H. Baumgart and G. Namkoong, *Novel hybrid organic/inorganic photovoltaic device configuration utilizing ALD technology and template based nanoelectrode arrays*, ECS Transactions, 2011.**41**:p. 279-284.
109. Kalita, G., M. Masahiro, W. Koichi and M. Umeno, *Nanostructured morphology of P3HT:PCBM bulk heterojunction solar cells*, Solid State Electronics, 2010.**54**:p. 447-451.
110. Kularatne, R. S., H. D. Magurudeniya, P. Sista, M. C. Biewer and M. C. Stefan, *Donor-acceptor semiconducting polymers for organic solar cells*, Journal of Polymer Science Part A: Polymer Chemistry, 2013.**51** (4):p. 743-768.
111. Tsakalakos, L., ed. *Nanotechnology for photovoltaics*. Vol 2010, CRC Press: Taylor and Francis Group. 1-429.
112. Furukawa, Y., F. Ueda, Y. Hyodo, I. Harada, T. Nakajima and T. Kawagoe, *Vibrational spectra and structure of polyaniline*, Macromolecules, 1988.**21** (5):p. 1297-1305.
113. Ibrahim, K. A., *Synthesis and characterization of polyaniline and poly(aniline-co-o-nitroaniline) using vibrational spectroscopy*, Arabian Journal of Chemistry, 2013,p. Ahead of Print.
114. Xia, Y., A. G. MacDiarmid and A. J. Epstein, *Camphorsulfonic acid fully doped polyaniline emeraldine salt: in situ observation of electronic and conformational changes induced by organic vapors by an ultraviolet/visible/near-infrared spectroscopic method*, Macromolecules, 1994.**27**:p. 7212-7214.
115. Kim, Y.-G., B. C. Thompson, N. Ananthakrishnan, G. Padmanaban, S. Ramakrishnan and J. R. Reynolds, *Variable band gap conjugated polymers for optoelectronic and redox applications*, Journal of Materials Research, 2005.**20**:p. 3188-3198.

116. Kho, J.-G., H.-D. Park and D.-P. Kim, *Photoluminescence of the Mn-doped ZnGa₂O₄ phosphors prepared by coprecipitation of metal salts*, Bulletin of the Korean Chemical Society, 1999.**20**:p. 1035-1039.
117. Dimple P. Dutta, R. G., A. K. Tyagi, *Luminescent properties of doped zinc aluminate and zinc gallate white light emitting nanophosphors prepared via sonochemical method*, Journal of Physical Chemistry C, 2009.**113**:p. 16954-16061.
118. Murthy, N. S., *Recent developments in polymer characterisation using X-ray diffraction*, The Rigaku Journal, 2004.**21** (1):p. 15-24.
119. Hirano, M., M. Imai and M. Inagaki, *Preparation of ZnGa₂O₄ spinel fine particles by the hydrothermal method*, Journal of the American Ceramic Society, 2000.**83**:p. 977-979.
120. Conklin, J. A., S.-C. Huang, S.-M. Huang, T. Wen and R. B. Kaner, *Thermal properties of polyaniline and poly(aniline-co-o-ethylaniline)*, Macromolecules, 1995.**28**:p. 6522-6527.
121. Iwuoha, E. I., D. Saenz de Villaverde, N. P. Garcia, M. R. Smyth and J. M. Pingarron, *Reactivities of organic phase biosensors. 2. The amperometric behaviour of horseradish peroxidase immobilised on a platinum electrode modified with an electrosynthetic polyaniline film*, Biosensors and Bioelectronics, 1997.**12** (8):p. 749-761.
122. Bard, A. J. and L. R. Faulkner, *Electrochemical Methods: Fundamentals and Applications*. 1980: Wiley.718
123. Motaung, D. E., G. F. Malgas and C. J. Arendse, *Comparative study: The effects of solvent on the morphology, optical and structural features of regioregular poly(3-hexylthiophene):fullerene thin films*, Synthetic Metals, 2010.**160** (9–10):p. 876-882.



124. Zhan, X. and D. Zhu, *Conjugated polymers for high-efficiency organic photovoltaics*, *Polymer Chemistry*, 2010.1:p. 409-419.

